

Assimilative Causal Inference

Marios Andreou and Nan Chen*

Department of Mathematics, University of Wisconsin–Madison, 480 Lincoln Drive, Madison, WI
53706-1325, USA

Erik Bollt†

Department of Electrical and Computer Engineering, Clarkson University, 8 Clarkson Ave, Potsdam,
13699-5815, NY, USA

A short video about “Assimilative Causal Inference” using animations in [Manim](#):

<https://youtu.be/lrcPweSC7mQ>

Contents

1	Introduction	2
2	The Assimilative Causal inference (ACI) Framework	4
2.1	Setup and Notation	4
2.2	Causal Discovery from a Bayesian Inverse Problem Viewpoint	4
2.3	ACI	5
3	Dynamic Discovery of the Causal Influence Range (CIR)	6
3.1	Online Smoothing for Dynamic Influence Tracking	6
3.2	Objective CIR	7
4	Conditional ACI in the Presence of Additional Non-Target Variables	7
5	Applications to Nonlinear Systems with Intermittency and Extreme Events	9
5.1	A Nonlinear Dyad Model with Extreme Events	9
5.2	A Stochastic Model Capturing the El Niño-Southern Oscillation (ENSO) Diversity	10
6	Conclusion and Discussions	11
	Supplementary Information	18
SI.A	Mathematical Foundations and Theoretical Analysis of Assimilative Causal Inference	18
A.1	Mathematical Framework and Notational Conventions	18
A.2	Bayesian Data Assimilation with Continuous-Time Observations	18
A.2.1	Underlying Dynamics	18
A.2.2	Bayesian Data Assimilation	19
A.2.3	Filter and Smoother	19
A.3	Explicit Expression of the ACI Framework for Gaussian Distributions	19
A.4	Conditional ACI in the Presence of Additional Non-Target Variables	20
A.4.1	Analyzing how \mathbf{x}_B Affects the State Estimation of $\mathbf{y}(t)$	21
A.4.2	Managing the Influence of \mathbf{x}_B on $\mathbf{y}(t)$ ’s Estimation	21

*Corresponding author (chennan@math.wisc.edu)

†In memory of our co-author Erik, who unexpectedly passed away on December 7, 2025

A.4.3	Arguments in Favor of the Conditional ACI Framework	22
A.4.4	Further Justification: Why Infinite Uncertainty Outperforms Marginalization . . .	23
A.5	Dynamic Discovery of the Causal Influence Range (CIR)	24
A.5.1	Quantifying the CIR	24
A.5.2	Subjective and Objective Perspectives of the CIR	25
A.5.3	Efficient Computation of the Objective CIR	26
SI.B	Analytically Tractable Nonlinear Systems for ACI Analysis	27
B.1	Conditional Gaussian Nonlinear Systems (CGNS)	27
B.1.1	The Modeling Framework	27
B.1.2	Filtering and Smoothing Distributions for CGNSs	28
B.2	Online Smoother for CGNSs	29
B.3	Calculation of the Subjective and Objective CIRs for CGNSs	30
SI.C	ACI-Based Principles of Nil Causality	32
C.1	Principle of Nil Assimilative Causality for CGNSs	32
C.2	Principle of Nil Conditional Assimilative Causality for CGNSs	33
SI.D	Numerical Studies: ACI Performance in Nonlinear Systems with Intermittency, Regime Switching and Extreme Events	36
D.1	A Nonlinear Dyad Model with Intermittent Extreme Events	37
D.2	A Noisy Predator–Prey Model	38
D.3	A Stochastic Model Capturing the El Niño–Southern Oscillation (ENSO) Diversity	41
D.3.1	Model Details	41
D.3.2	Additional Results Using Model-Generated Data	42
D.3.3	ACI on Real-World ENSO Data	42

Abstract

Causal inference is fundamental across scientific disciplines, yet existing methods struggle to capture instantaneous, time-evolving causal relationships in complex, high-dimensional systems. In this paper, assimilative causal inference (ACI) is developed, which is a methodological framework that leverages Bayesian data assimilation to trace causes backward from observed effects. ACI solves the inverse problem rather than quantifying forward influence. It uniquely identifies dynamic causal interactions without requiring observations of candidate causes, accommodates short datasets, and, in principle, can be implemented in high-dimensional settings by employing efficient data assimilation algorithms. Crucially, it provides online tracking of causal roles that may reverse intermittently and facilitates a mathematically rigorous criterion for the causal influence range, revealing how far effects propagate. The effectiveness of ACI is demonstrated by complex dynamical systems showcasing intermittency and extreme events. ACI opens valuable pathways for studying complex systems, where transient causal structures are critical.

1 Introduction

Causal inference determines cause-and-effect relationships between variables [33, 32, 42]. It has found wide applications across different disciplines such as atmospheric and ocean science, economics, and neuroscience [4, 39, 34]. In addition to discovering the interactions between variables, causal inference plays a significant role in model identification, policy evaluation, and decision-making [36, 7, 43, 55, 40].

Methods for causal inference can be classified into different categories depending on the available resources for use. On the one hand, a natural way to identify the overall causal structures is to exploit multivariate time series, where temporal dependencies are often utilized to infer causal relationships. Methods falling into this category include Granger causality [21], transfer entropy [47, 5], mutual

information [13, 19], convergent cross mapping [49, 31], causation entropy [51, 50], and mixture causal discovery [52]. On the other hand, models built upon physics can assist in understanding causal dependence between different variables. Information transfer based on the ensemble forecast of the underlying model has been exploited to indicate certain causal relationships for a short term [27]. In addition, linear response theory, which infers causal links by analyzing system responses to small perturbations at the equilibrium, has been utilized to reveal the attributions of variations in climate systems [28, 17, 23]. Other recently developed methods include using Koopman operators for causal discovery [44], causal graphs [25], dynamic neural relational inference [20], and approaches based on machine learning [6, 35, 48].

Nature can be regarded as a complex dynamical system where only a single random realization from this system is available. Due to the underlying strong nonlinearity and multiscale features, such a realization is usually intermittent and stochastic. Detecting instantaneous causal relationships as a function of time is crucial for understanding the dynamic interplay among variables, where the roles of causes and effects can shift repeatedly over time and at irregular intervals. In environmental science, extreme events, such as the triggering mechanisms of hurricanes and the abrupt transitions in weather patterns, have significant scientific and social impacts. Understanding the precursor of each extreme event and its subsequent implications requires online tracking of the causal relationship between them. Likewise, instantaneous causal analysis is of broad interest in neuroscience to discover temporary role reversals between brain regions during decision-making or cognitive tasks. However, most purely data-driven causal inference methods exploit data points over a long time series to reveal the average causal directions. In contrast, purely model-based methods, such as computing the information transfer in [27], utilize ensemble forecasts to infer the causal relationship when the system begins from a given initial condition and evolves toward statistical equilibrium. Yet, these methods are typically only able to provide time-dependent results for a very short time and become computationally challenging as the dimension of the system increases. Additionally, these model-based methods often struggle to optimally handle cases with a single observed realization.

Given the importance of discovering instantaneous causal relationships, this paper introduces a methodological framework called assimilative causal inference (ACI) to compute time-dependent causal interactions in complex systems. As in many practical applications, only a single realization of a subset of the state variables is available as observations. Meanwhile, an associated model, often turbulent and stochastic, is accessible as a supplement. Fundamentally different from traditional causal inference methods, which treat causality as a forward problem (analyzing how causes propagate into effects), ACI addresses it as an inverse problem. Using Bayesian data assimilation, ACI traces causes backward from observed effects by quantifying whether incorporating information about the effects reduces uncertainty in reconstructing potential causes.

ACI has several desirable advantages. First, it captures the evolving interplay among state variables, as their causal and effect roles can be reversed across time. Thus, ACI provides direct insights beyond time-averaged causal links, making it particularly valuable for studying turbulent systems with intermittency and regime switching. Second, ACI identifies the causal inference range (CIR), revealing how far causal effects propagate at each time instant. The framework includes a mathematically justified criterion to determine the CIR without empirical thresholds. While the importance of the CIR has been highlighted in complex networks [41, 56], ACI offers a unique and general method for its computation in turbulent systems with varying autocorrelation decay rates. Third, ACI scales efficiently to high-dimensional problems by leveraging computational methods developed in Bayesian data assimilation. This is fundamentally different from information-transfer methods limited to low dimensions [27]. In addition, ACI can accommodate short time series and incomplete datasets, which often appear in geophysics and climate science. Notably, ACI does not require observations of candidate causes, which is a key advantage since potential drivers are usually unknown or unmeasured. Instead, uncertainty reduction in potential causal variables can be determined solely from the

observed effects and governing dynamical model via Bayesian assimilation. As a final remark, while data assimilation has been used to assist in detecting the attribution of weather and climate-related events [22, 9], these studies primarily focus on estimating the state in response to specific external perturbations, rather than online causal inference or CIR estimation. ACI also fundamentally differs from these methods in its integration of data assimilation into causal inference.

The remainder of this paper is organized as follows. Section 2 presents the operational details of the ACI framework, followed by the discussion of CIR in Section 3. Section 4 extends the ACI framework to account for the presence of non-target variables. Numerical results from applying ACI on various nonlinear complex dynamical systems with intermittency and extreme events are presented in Section 5. Concluding remarks are contained in Section 6. Additional mathematical derivations and supplementary test results are available in the Supplementary Information.

2 The Assimilative Causal inference (ACI) Framework

In this section, we provide a high-level overview of the methodology underlying the ACI framework, including its formulation of causal inference as a Bayesian inverse problem. Rigorous mathematical justifications are provided in the Supplementary Information.

2.1 Setup and Notation

Consider a time interval $[0, T]$ and a specific time instant t , where $0 \leq t \leq T$. Let $\{\mathbf{x}(t)\}_{0 \leq t \leq T}$ and $\{\mathbf{y}(t)\}_{0 \leq t \leq T}$ be two multivariate stochastic processes defined over this interval. Denote by $\mathbf{x}(t)$ and $\mathbf{y}(t)$ the corresponding multivariate random variables at time t . Their evolution in time is defined by the following stochastic dynamical system:

$$\begin{aligned} \frac{d\mathbf{x}}{dt} &= \mathbf{f}^{\mathbf{x}}(t, \mathbf{x}, \mathbf{y}) + \Sigma_1^{\mathbf{x}}(t, \mathbf{x})\dot{\mathbf{W}}_1 + \Sigma_2^{\mathbf{x}}(t, \mathbf{x})\dot{\mathbf{W}}_2, \\ \frac{d\mathbf{y}}{dt} &= \mathbf{f}^{\mathbf{y}}(t, \mathbf{x}, \mathbf{y}) + \Sigma_1^{\mathbf{y}}(t, \mathbf{x}, \mathbf{y})\dot{\mathbf{W}}_1 + \Sigma_2^{\mathbf{y}}(t, \mathbf{x}, \mathbf{y})\dot{\mathbf{W}}_2, \end{aligned} \quad (2.1)$$

where $\dot{\mathbf{W}}_1$ and $\dot{\mathbf{W}}_2$ are independent mean-zero Gaussian random vectors with uncorrelated components that possess unit variance. Mathematical details regarding the structure of (2.1) are given in the Supplementary Information. For notational simplicity, the dependence on t is sometimes omitted when referring to these state variables and no distinction between random variables and their realizations is made. Let $\mathbf{x}(s \leq t)$ represent one realization of the stochastic process $\{\mathbf{x}(t)\}_{0 \leq t \leq T}$ as a time series over the interval $[0, t]$. Similarly, $\mathbf{x}(s \leq T)$ denotes a realization of $\{\mathbf{x}(t)\}_{0 \leq t \leq T}$ as a time series over the entire interval $[0, T]$. For simplicity, the time series are assumed to be continuously observed. An analogous framework can be developed for discrete-in-time observations. Throughout this paper, the time series is assumed to be free of observational noise.

According to Granger’s predictive causality or its nonlinear extension, transfer entropy, \mathbf{y} is the cause of \mathbf{x} at time t if the knowledge of $\mathbf{y}(s \leq t)$ improves the prediction or reduces the uncertainty of $\mathbf{x}(t)$ [21, 47, 5]. Using information theory, this can be expressed as:

$$\mathcal{S}(p(\mathbf{x}(t)|\mathbf{y}(s \leq t))) < \mathcal{S}(p(\mathbf{x}(t))), \quad (2.2)$$

where $\mathcal{S}(\cdot)$ is Shannon’s entropy and the history of the target variable in the conditioning, i.e., $\mathbf{x}(s < t)$, is omitted in (2.2) for notational simplicity.

2.2 Causal Discovery from a Bayesian Inverse Problem Viewpoint

The above argument can be interpreted in a reverse way, from the perspective of statistical inference through an inverse problem in uncertainty quantification. If \mathbf{x} is the subsequent effect of $\mathbf{y}(t)$, then

knowing future information about \mathbf{x} reduces the uncertainty in inferring the current state of \mathbf{y} :

$$\mathcal{S}(p(\mathbf{y}(t)|\mathbf{x}(s > t))) < \mathcal{S}(p(\mathbf{y}(t))). \quad (2.3)$$

Further including the past information of \mathbf{x} on both side yields

$$\mathcal{S}(p(\mathbf{y}(t)|\mathbf{x}(s \leq T))) < \mathcal{S}(p(\mathbf{y}(t)|\mathbf{x}(s \leq t))), \quad (2.4)$$

which does not change the causal relationship in (2.3).

A notable feature of (2.4) is that it establishes a connection between causal discovery and Bayesian data assimilation. Suppose the underlying turbulent and potentially stochastic model governing \mathbf{x} and \mathbf{y} is known and given by (2.1). Running the model forward provides a statistical estimation of the state of $\mathbf{y}(t)$ (known as ‘forecast’). However, this state estimation differs when also incorporating the knowledge of the time series $\mathbf{x}(s \leq t)$ or $\mathbf{x}(s \leq T)$ (known as ‘analysis’), as the specific observation provides additional information to reduce the uncertainty when inferring the state of $\mathbf{y}(t)$. This two-step (forecast-analysis) process is known as Bayesian data assimilation [26, 37], where the distribution derived solely from the model statistics is referred to as the prior, while the observed time series is used to compute the likelihood, accounting for the uncertainty in the observational process. The two conditional distributions in (2.4) result from combining the model-based information with the observation-induced likelihood and are referred to as the posteriors. Specifically, the distribution on the left-hand side of (2.4) corresponds to smoothing, while the one on the right-hand side corresponds to filtering [16, 46].

2.3 ACI

Denote by p_t^s and p_t^f the smoother and filter posterior distributions at time t (i.e., the two distributions on the left- and right-hand sides of (2.4)), respectively. If the uncertainty reduction in p_t^s is more significant than that in p_t^f , then it is due to the incorporation of the future information of \mathbf{x} , which indicates toward the contribution from $\mathbf{y}(t)$ to the future states of \mathbf{x} .

Although the entropy difference has been widely used in many other causal inference methods, the relative entropy is employed hereafter to quantify the uncertainty reduction in p_t^s related to p_t^f . In addition to the covariance (and other higher-order moments), which measure the variability of the random variable, the relative entropy also accounts for the difference in the mean state of the two distributions. This difference is crucial for reflecting the additional information gained by incorporating future observations. Furthermore, it is coordinate-free, i.e., it is invariant under general nonlinear changes of the state variables. Notably, relative entropy has been widely used to assess uncertainty reduction in the context of data assimilation [54, 29, 18, 10].

As such, if the relative entropy between the smoother and filter distributions is nonzero, i.e.,

$$\mathcal{P}(p_t^s, p_t^f) = \int p_t^s \ln(p_t^s/p_t^f) > 0, \quad (2.5)$$

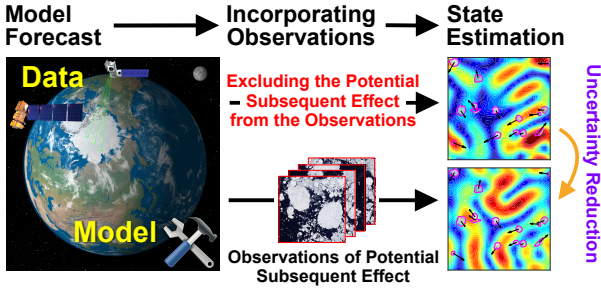
then \mathbf{y} is identified as the cause of \mathbf{x} at time t . By computing (2.5) at different t , a time-dependent causal link is established.

Under (2.5), ACI provides a unique formulation for identifying causal relationships. In traditional approaches, causal links are inferred by running (2.1) forward to quantify the informational response on the target variables’ entropy when conditioned on the history of the candidate causes. ACI instead solves an inverse problem, thus tracing causes back from the data of the observed subsequent effects. By interpolating causality from effects to causes instead of extrapolating the latter forward-in-time, ACI offers an inherently more robust framework compared to classical predictive causality. Interpolation is typically more stable because it operates within the range of observed information,

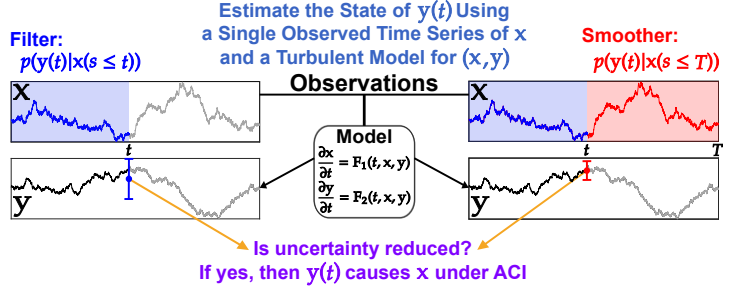
Assimilative Causal Inference (ACI)

Inverse Problem: Tracing Causes Backward from Observed Effects

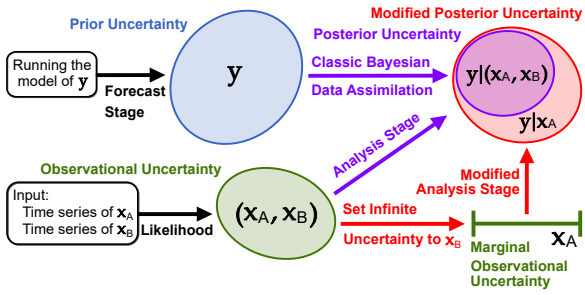
(a) High-Level Overview of Framework



(b) Schematic Illustration of ACI Essential Details



(c) Conditional ACI in the Presence of Non-Target Variables



(d) Objective Causal Influence Range (CIR)

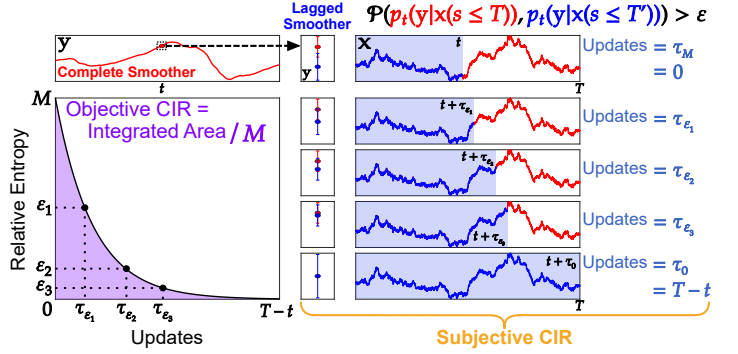


Figure 1: The ACI framework. Panel (a): A high-level overview of the proposed method. Panel (b): Schematic illustration of ACI from a more technical viewpoint. Panel (c): ACI in the presence of non-target variables. Panel (d): Objective CIR, as an average of the associated subjective CIRs.

whereas extrapolation requires projecting beyond available data and is therefore far more sensitive to model error and uncertainty.

Panel (a) of Figure 1 provides a high-level overview of the ACI framework, while Panel (b) presents a schematic illustration of ACI using the filter and smoother estimates. The Supplementary Information contains more technical details.

3 Dynamic Discovery of the Causal Influence Range (CIR)

While the uncertainty reduction in the smoother solution related to the filter solution in (2.5) indicates an instantaneous causal link from \mathbf{y} to \mathbf{x} at time t , it does not reveal the temporal extent of this causal influence, namely, how many future units of \mathbf{x} are affected by $\mathbf{y}(t)$. Since the memory of turbulent systems decays over time, $\mathbf{y}(t)$ is expected to effectively influence the future states \mathbf{x} only within a limited time period, where this causal influence range can vary significantly as a function of t . This raises two key questions: How can we determine the CIR and, more importantly, how can we do so objectively, i.e., without relying on empirical cutoff thresholds? This section outlines the core ideas for addressing these questions. Rigorous mathematical analysis and detailed algorithms are provided in the Supplementary Information.

3.1 Online Smoothing for Dynamic Influence Tracking

Recall from (2.5) that the relative entropy $\mathcal{P}(p_t^s, p_t^f)$ between the filter and smoother estimates quantifies the causal influence from $\mathbf{y}(t)$ to \mathbf{x} . Here, $p_t^s = p(\mathbf{y}(t)|\mathbf{x}(s \leq T))$ incorporates the complete future information of \mathbf{x} . Due to the finite effective influence length, the complete smoother solution p_t^s achieves a substantial uncertainty reduction compared to the lagged posterior distributions

$p(\mathbf{y}(t)|\mathbf{x}(s \leq T'))$), which only utilize future information up to $t \leq T' \leq T$, for a short time period after t . The divergence between these distributions vanishes as $T' \rightarrow T$. We therefore define the causal influence radius or CIR through the relative entropy criterion: For a predetermined threshold $\varepsilon \geq 0$, the maximum lag T'_ε satisfying

$$\mathcal{P}(p(\mathbf{y}(t)|\mathbf{x}(s \leq T)), p(\mathbf{y}(t)|\mathbf{x}(s \leq T'_\varepsilon))) > \varepsilon, \quad (3.1)$$

yields the innate CIR measure $\tau_\varepsilon(t) = T'_\varepsilon - t$. This adaptive time variable $\tau_\varepsilon(t)$ defines the effective causal period $[t, t + \tau_\varepsilon(t)]$ during which $\mathbf{y}(t)$ exerts measurable influence on \mathbf{x} . A recently developed online smoother algorithm [3] is employed to compute the CIR. This online smoother computes the uncertainty reduction in the estimated state of $\mathbf{y}(t)$ when the future information of \mathbf{x} is sequentially added. See the Supplementary Information for more technical details.

While the CIR computed via (3.1) is intuitive, it remains inherently subjective due to its dependence on the threshold parameter ε . In the following, an objective CIR formulation is developed, eliminating the need for a prescribed threshold. This threshold-independent measure is subsequently integrated into the ACI framework.

3.2 Objective CIR

For simplicity, assume that the relative entropy between the aforementioned complete and lagged smoother distributions decreases monotonically as more future information of \mathbf{x} is incorporated. This commonly holds in practice, though the theory of the objective CIR (developed rigorously in the Supplementary Information) doesn't require this condition. At a given time instant t , let $M = \mathcal{P}(p_t^s, p_t^f)$ denote the maximum value of the relative entropy between the complete and lagged smoother distributions over $t \leq T' \leq T$, which is the difference between the smoother estimate and the filter estimate (where the latter can be viewed as a degenerate smoother using no future information). Given a threshold $\varepsilon \in [0, M]$, (3.1) yields a subjective CIR as $\tau_\varepsilon(t) = T'_\varepsilon - t$. The objective CIR is then naturally defined by

$$\tau(t) := \frac{1}{M} \int_0^M \tau_\varepsilon(t) d\varepsilon. \quad (3.2)$$

Dividing M guarantees the unit of the objective CIR is “time”. See Panel (d) of Figure 1 for a schematic illustration of the objective CIR and its relationship with the subjective ones. Note that numerically evaluating the integral in (3.2) requires repeated smoother computations, leading to a computational complexity that scales quadratically with the number of discretization points. An efficient computational method of (3.2) is included in the Supplementary Information.

The subjective and objective CIR can be regarded as analogs of the autocorrelation function and decorrelation time, respectively. The autocorrelation function measures the memory of a turbulent system based on the duration of its values that remain above a predetermined threshold. However, determining the memory using the autocorrelation function is subjective and can vary significantly depending on the threshold value. In contrast, the decorrelation time, which integrates the autocorrelation function, provides an objective way to define the memory length and is free from any predetermined cutoff threshold.

4 Conditional ACI in the Presence of Additional Non-Target Variables

In the more general context of a complex system, state variables can be grouped into three disjoint subsets: \mathbf{x}_A , \mathbf{x}_B , and \mathbf{y} , with $\mathbf{x} = (\mathbf{x}_A, \mathbf{x}_B)^T$ under the previous notation. The goal is to determine

whether \mathbf{y} is a cause of \mathbf{x}_A in the presence of the remaining variables \mathbf{x}_B , which are called the non-target variables, including the cases of confounders or mediators. Since \mathbf{x}_B interacts with both \mathbf{x}_A and \mathbf{y} , appropriately accounting for the role of \mathbf{x}_B while inferring the causal link from \mathbf{y} to \mathbf{x}_A becomes essential. Hereafter, let us assume that a realization for each of \mathbf{x}_A and \mathbf{x}_B , namely $\mathbf{x}_A(s \leq T)$ and $\mathbf{x}_B(s \leq T)$, is available. Therefore, the candidate cause \mathbf{y} is the only variable that does not require to have observations in this framework. Following the argument in Section 2, the causal relationship from $\mathbf{y}(t)$ to $(\mathbf{x}_A, \mathbf{x}_B)$ is identified based on the uncertainty reduction in the smoother distribution p_t^s related to the filter one p_t^f , where

$$\begin{aligned} p_t^f &= p(\mathbf{y}(t) | \mathbf{x}_A(s \leq t), \mathbf{x}_B(s \leq t)), \\ p_t^s &= p(\mathbf{y}(t) | \mathbf{x}_A(s \leq T), \mathbf{x}_B(s \leq T)). \end{aligned}$$

The main focus here is to appropriately determine and resolve the presence of \mathbf{x}_B from p_t^f and p_t^s as to infer a conditional causal relationship from $\mathbf{y}(t)$ to \mathbf{x}_A beyond the contributions of \mathbf{x}_B .

Recall from Section 2 that ACI employs Bayesian data assimilation to estimate the state of $\mathbf{y}(t)$. ACI exploits observations of \mathbf{x} to reduce the uncertainty in $\mathbf{y}(t)$, where the influence of \mathbf{x} on the estimation of $\mathbf{y}(t)$ depends on its own uncertainty: smaller observational uncertainty leads to a stronger impact [38]. When extending this framework to $\mathbf{x} = (\mathbf{x}_A, \mathbf{x}_B)^T$ for conditional ACI, the observed time series of \mathbf{x}_B is still used in the forecast step to compute the uncertainties in \mathbf{x}_A and \mathbf{y} . However, during the analysis step, the uncertainty in \mathbf{x}_B 's dynamics is deliberately excluded by assigning infinite uncertainty to its marginal likelihood before posterior computation. This can be rigorously formulated through a limit operation on the analysis component of the Bayesian data assimilation update equations, which formally leads to the following filter- and smoother-based distributions:

$$p_t^{\text{f}|\mathbf{x}_B} := \lim_{\text{Var}(\mathbf{x}_B(t)) \rightarrow +\infty} p_t^f, \quad p_t^{\text{s}|\mathbf{x}_B} := \lim_{\text{Var}(\mathbf{x}_B(t)) \rightarrow +\infty} p_t^s.$$

Similar to (2.5), if the relative entropy of $p_t^{\text{s}|\mathbf{x}_B}$ from $p_t^{\text{f}|\mathbf{x}_B}$ is positive, $\mathcal{P}(p_t^{\text{s}|\mathbf{x}_B}, p_t^{\text{f}|\mathbf{x}_B}) > 0$, then \mathbf{y} is identified as the cause of \mathbf{x}_A conditional to \mathbf{x}_B at time t . This means future data of \mathbf{x}_A incur additional information gain about $\mathbf{y}(t)$ related to its history, beyond the observational contributions of \mathbf{x}_B . By computing this metric at each t , a time-dependent conditional causal relationship is established.

Inflating the uncertainty in \mathbf{x}_B is straightforward using Bayesian inference for state estimation. This approach ensures that \mathbf{x}_B does not affect the uncertainty reduction in the state estimation of $\mathbf{y}(t)$ when treated as an observational process. Consequently, any uncertainty reduction in $\mathbf{y}(t)$ results solely from \mathbf{x}_A under this proposed pipeline. See Panel (c) of Figure 1 for an illustration. For dynamical systems with explicit governing equations (see (2.1)), a shortcut to exclude the influence in the uncertainty of \mathbf{x}_B is to treat \mathbf{x}_B as a prescribed forcing term in the reduced system defined by $(\mathbf{x}_A, \mathbf{y})$ during Bayesian inference, with values defined by its observed time series. Nevertheless, this framework does not necessarily require modifications to the underlying dynamical system, making it compatible with any given model, potentially including operational models in atmospheric and ocean science, as the model structure and integrity remains intact.

It is important to emphasize that while treating \mathbf{x}_B as a conditioning variable may appear analogous to the role of non-target variables in transfer entropy and other traditional causal inference methods, the way of handling the uncertainty in ACI is fundamentally different. Conventional methods treat \mathbf{x}_B as a fixed component. In contrast, ACI explicitly accounts for \mathbf{x}_B 's dynamical influence while systematically prohibiting its uncertainty from affecting state estimation. This unique treatment allows the inferred causal relationships to reflect true dynamical interactions by isolating the contribution of uncertainty reduction from the non-target variables. As a final remark, if Bayesian data assimilation is used to compute $p(\mathbf{y}(t), \mathbf{x}_B(t) | \mathbf{x}_A(s \leq T))$ and then marginalize over $\mathbf{x}_B(t)$ to obtain $p(\mathbf{y}(t) | \mathbf{x}_A(s \leq T))$, this manipulation may lead to incorrect conclusions. This is because the

correlation between $\mathbf{y}(t)$ and $\mathbf{x}_B(t)$ unavoidably alters the uncertainty in $\mathbf{y}(t)$ during Bayesian data assimilation, potentially introducing a spurious causal relationship between \mathbf{y} and \mathbf{x}_A . This is true even if we condition over $\mathbf{x}_B(t)$ to obtain $p(\mathbf{y}(t)|\mathbf{x}_A(s \leq T), \mathbf{x}_B(t))$. For instance, for the causal chain $\mathbf{y} \rightarrow \mathbf{x}_B \rightarrow \mathbf{x}_A$, such a method might falsely imply a direct causal link from $\mathbf{y}(t)$ to \mathbf{x}_A .

The details of the conditional ACI implementation, along with the verification of (conditional) nil causality principles under ACI, are provided in the Supplementary Information.

5 Applications to Nonlinear Systems with Intermittency and Extreme Events

We apply the ACI framework to identify causal relationships across the state space and evaluate the corresponding CIRs in complex nonlinear dynamical systems exhibiting intermittency and extreme events. The dynamical properties of these systems and the mechanisms that trigger crucial observed phenomena are well understood. This knowledge is exploited as guidance to validate the results when applying ACI. In addition, a perfect-model setup is used in the case studies carried out, meaning the system generates the synthetic observational data and the forecast model in ACI at the same. This facilitates the recovery of causal relationships in the absence of model error. Because the underlying system is chaotic and subject to stochastic forcing, a perfect model means that the model used in ACI shares the same governing equations and long-term statistical behavior as the system that generates the true signal. Additional results, including further numerical experiments, case studies, and one crucial application using sparse real-world observations, are provided in the Supplementary Information.

The operational outline of the ACI metric used to infer instantaneous causal relationships in the following experiments, including the details of how we determine the associated CIRs and account for non-target variables, is described in Sections 2–4. The developed framework is also summarized via the schematic diagram provided in Figure 1. Additional mathematical results and analyses, as well as computational implementation details, can be found in the Supplementary Information.

5.1 A Nonlinear Dyad Model with Extreme Events

Let us start with a two-dimensional model, which nevertheless has strong nonlinear features with observed extreme events. The model reads as:

$$\frac{dx}{dt} = -d_x x + \gamma xy + f_x + \sigma_x \dot{W}_x \quad (5.1a)$$

$$\frac{dy}{dt} = -d_y y - \gamma x^2 + f_y + \sigma_y \dot{W}_y, \quad (5.1b)$$

where \dot{W}_x and \dot{W}_y are independent standardized normal random variables. Within the proposed ACI framework, only x is assumed to be observed over time. This is a reduced-order conceptual model for atmospheric variability. It has been used to analyze the effects of various coarse-grained procedures on processes exhibiting intermittency, large-scale bifurcations, and microscale phase transitions. It is defined by an energy-conserving condition on its quadratic nonlinearities [30]. The following parameter values are used for this model:

$$\begin{aligned} d_x = 0.5, \quad \gamma = 2, \quad f_x = 0.5, \quad \sigma_x = 0.5, \\ d_y = 0.5, \quad f_y = 1, \quad \sigma_y = 1. \end{aligned} \quad (5.2)$$

Figure 2 illustrates the ACI and CIRs from y to x . Panel (a) shows that extreme events in x occur intermittently. When the combined coefficient $-d_x + \gamma y$ in (5.1a) becomes positive, the dynamics

of x exhibit anti-damping, leading to amplitude growth and extreme events. Conversely, when the coefficient is negative, x behaves as a damped system, with fluctuations primarily driven by random noise. Panel (b) displays the ACI, revealing that phases with significant ACI values largely coincide with the onset and peak phases of extreme events in x . This aligns with intuition, as y acts as an anti-damping source and the primary driver of these events. Once x peaks and begins to decay, the ACI value drops sharply, reflecting the strong negative feedback from x to y , which then dampens x . The whisker plot in Panel (a) highlights the objective CIR, indicating a sustained influence from y to x during the triggering phase of extreme events but minimal influence during their demise. Notably, the long-range influence from the CIR reveals that extreme events develop gradually, with triggering conditions established well in advance. From a data assimilation perspective, when the observable signal x starts to strengthen, it enhances the ability of the smoother to estimate y as the signal in the future contains useful information beyond noise. As a result, a longer CIR is obtained. In contrast, once x becomes sufficiently strong, its high signal-to-noise ratio ensures the filter captures all relevant triggering dynamics, leaving little room for the smoother to improve estimates. Hence, the outset of the ACI metric's decline and shorter CIR. The Supplementary Information contains the filter and smoother distributions and the subjective CIR with different threshold values ε .

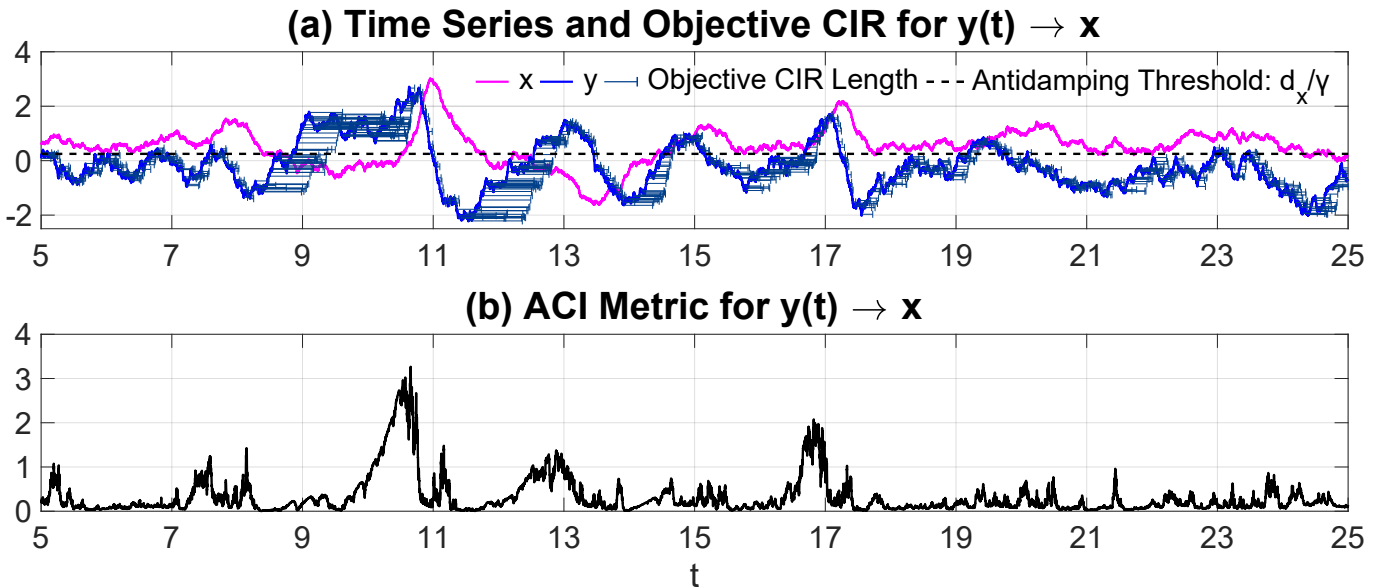


Figure 2: ACI values and CIRs from y to x at each time instant t for the nonlinear dyad model (5.1). Panel (a): Time series of x (magenta) and y (blue), the objective CIR represented by a whisker plot emanating forward in time from each $y(t)$ value, and the anti-damping threshold line at d_x/γ . Panel (b): ACI from y to x as a function of time.

5.2 A Stochastic Model Capturing the El Niño-Southern Oscillation (ENSO) Diversity

El Niño–Southern Oscillation (ENSO) is a dominant climate phenomenon characterized by quasi-regular periodic behaviors in sea surface temperatures (SSTs) and in the atmospheric circulation across the equatorial Pacific Ocean [12, 45]. ENSO exhibits remarkable diversity in its spatial patterns, temporal evolution, and impacts, which can be broadly categorized into two main types: Eastern Pacific (EP) and Central Pacific (CP) El Niños, where an anomalous warming center occurs in the eastern and central Pacific, respectively [8]. The opposite phases with anomalous cooling SSTs are called La Niña. Understanding the causes of different ENSO events is crucial for improving climate predictions and mitigating socio-economic consequences.

Although few models can accurately capture ENSO diversity, a recently developed stochastic conceptual model successfully reproduces its diverse behaviors and non-Gaussian statistics [11]. This

model has been highlighted in a recent review [53], making it a suitable testbed for studying the ENSO diversity. Mathematical details are provided in the Supplementary Information. The model consists of six state variables: ocean zonal current in the CP (u), western Pacific (WP) thermocline depth (h_W), CP SST (T_C), EP SST (T_E), atmospheric winds (τ , intraseasonal), and background Walker circulation (I , decadal). The first four variables (u , h_W , T_C , and T_E) operate on interannual timescales. As a nonlinear system with state-dependent noise, the model generates extreme events and intermittency. The two SST variables allow reconstruction of spatiotemporal SST patterns across the equatorial Pacific, providing an intuitive way to identify different ENSO event types.

The variables T_C , h_W , and τ directly influence T_E . Figure 3 displays their conditional ACI and CIR values to T_E (non-target variables have been resolved via the framework proposed in Section 4). For EP El Niño events (positive T_E anomalies, shown in red), T_C exhibits the strongest ACI value, slightly preceding the T_E peak. This timing aligns with physical understanding, as SSTs in these regions are strongly coupled: during El Niño, warm water propagates from CP to EP, producing the observed ACI lead. The τ to T_E ACI value appears noisier due to τ 's intraseasonal variability, yet its evolution confirms τ 's robust impact on T_E . Winds drive warm water propagation and exert near-instantaneous SST effects. In contrast, while h_W significantly contributes to T_E , its ACI amplitude is weaker than T_C or τ . The discharge–recharge theory [24] posits h_W – T_E oscillator dynamics, but in models with refined CP variables, h_W 's influence on T_E becomes indirect: h_W first affects T_C , which then propagates signals to T_E (WP→CP→EP). Consistent with this paradigm, h_W 's ACI value to T_E peaks months before EP El Niño maxima. CIRs further corroborate these physical mechanisms: T_C shows the longest influence, h_W 's more indirect role yields intermediate CIRs, and τ 's intraseasonal nature produces the shortest impacts. The Supplementary Information provides additional ACI and CIR analyses for all variables across different ENSO event types. In addition, in the Supplementary Information, a case study using real-world ENSO observations is examined, which does not assume a perfect model setup. The conclusions derived about the causal relationships using real-world observational data remain qualitatively similar to those with model-generated data. The results provide preliminary evidence that the ACI framework remains reasonably robust under realistic conditions, including observational noise, moderate model error, and numerical discretization effects.

6 Conclusion and Discussions

In this paper, the assimilative causal inference (ACI) framework is developed for the detection of instantaneous causal relationships and of their associated causal influence range (CIR) in complex dynamical systems. ACI leverages Bayesian data assimilation to trace causes backward from observed effects. It uniquely identifies dynamic causal interactions without requiring observations from candidate causes, accommodates short datasets, and, in principle, can be scaled efficiently to high dimensions using efficient Bayesian data assimilation algorithms. Crucially, it provides online tracking of causal roles, which may reverse intermittently, and facilitates a mathematically rigorous criterion for the causal influence range, revealing how far causal impacts propagate temporally. Its ability to dynamically detect causal influence ranges and handle high-dimensional systems by employing computationally efficient Bayesian techniques highlights its potential for applications in climate science, neuroscience, and other fields. Numerical tests on nonlinear systems with extreme events and regime transitions demonstrate the effectiveness and robustness of the framework.

It is worth highlighting how ACI differs from other state-of-the-art methods in terms of expressivity, computational complexity, and underlying assumptions. Different from most methods that identify cause-and-effect relationships by running the system forward and quantifying informational responses in the target variables' entropy conditioned on past candidate causes, which is a predictive setting typical of information-flow-based methods, ACI instead formulates causality as an inverse problem

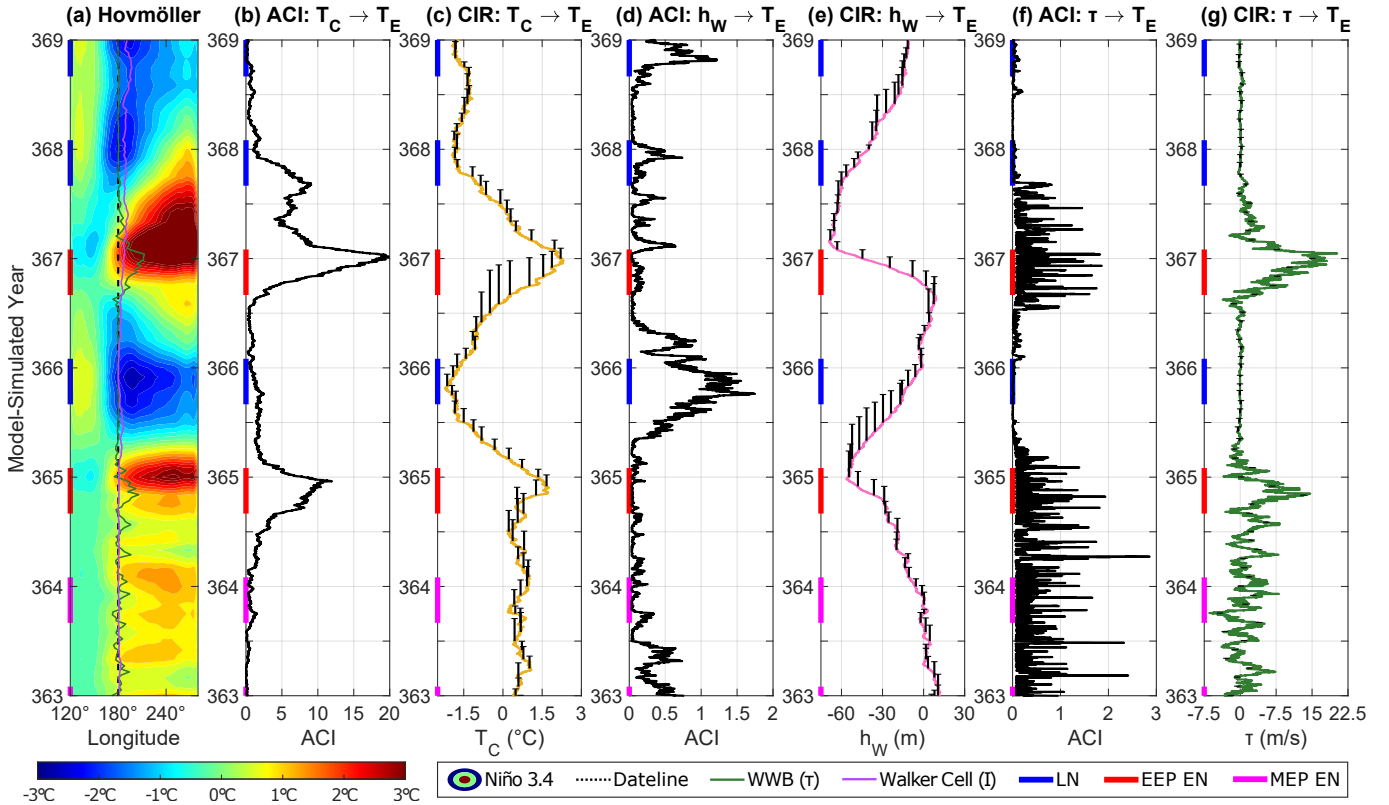


Figure 3: Conditional ACI values and CIRs of the stochastic conceptual model for the ENSO diversity with T_E as the effect variable over a six-year model-simulated period (where EEP EN and MEP EN stand for extreme and moderate EP El Niños, respectively, and LN for La Niña). Panel (a): Hovmöller diagram of the SST anomalies in the equatorial Pacific reconstructed from T_C and T_E via a spatiotemporal multivariate regression technique [11]. Panel (b): ACI values from T_C to T_E as a function of time. Panel (c): Time series of the observable T_C and the objective CIR represented by a whisker plot emanating forward in time from the value of T_C at each month over this six-year period. Panels (d) and (e): Same as Panels (b) and (c) but for the causal link from h_W to T_E . Panels (f) and (g): Same as Panels (b) and (c) but for the causal link from τ to T_E .

in uncertainty quantification. Within the Bayesian data assimilation framework, candidate causal variables are inferred backward from observations of their potential effects. Thus, while many existing methods extrapolate causes forward in time, ACI traces causes back from observed effects, effectively interpolating rather than extrapolating causality. This distinction makes ACI more expressive in capturing instantaneous causal structures and, in practice, often more robust. From a computational standpoint, ACI can leverage well-developed Bayesian data assimilation tools that scale effectively to high-dimensional systems [15, 26]. In contrast, information transfer and other model-based methods often require computing the exact density functions and their derivatives, which is computationally demanding and subject to the curse of dimensionality. Finally, ACI requires only a single time series but assumes access to a dynamical model, which enables it to identify instantaneous causal relationships. In contrast, most time-series-based methods operate under model-free assumptions and therefore focus on aggregated or time-averaged causal links rather than on causality at specific moments. Because ACI incorporates model dynamics, it does not require long time series to detect causes and effects. Instead, it can infer instantaneous causal links from a single data point combined with model information. In contrast, most purely data-driven methods rely on long time series and can only reveal causal relationships in a time-averaged sense.

Future work will focus on several important directions. First, because model error is ubiquitous in practice, it is essential to study its impact on causal inference. Understanding how model error affects inferred causal relationships can create opportunities not only to detect and correct model

error, but also to leverage this information to develop parsimonious models for complex dynamical systems. Similarly, observational data may contain additional noise that can affect causal inference. The ACI framework provides a natural way to analyze how observational noise contaminates causal detection. In such a context, data assimilation can serve as a pre-filtering step to reduce the influence of observational noise, which allows for a systematic examination of its role in shaping causal inference outcomes. Second, by building on the computationally efficient methods developed in Bayesian data assimilation, it is essential to apply ACI to higher-dimensional systems. Ensemble data assimilation is a well-established technique that routinely uses localization, covariance inflation, and other adjustments to overcome the curse of dimensionality [1, 14, 2]. As a result, the ensemble size (typically on the order of $O(100)$) is often chosen independently of the system's dimension, which contributes to the scalability of Bayesian data assimilation and, consequently, of ACI. However, the sampling errors inherent in ensemble methods may introduce additional biases. Thus, it is necessary to examine whether such errors affect ACI. In addition, various coarse-grained approaches, such as approximating the full distribution with a Gaussian, are widely used in practice. Although these approximations introduce errors in computing the PDF, they are robust and highly accurate when computing diagnostic indicators, such as the relative entropy, that are used for model identification and sensitivity analysis. Thus, they may substantially accelerate ACI in practice. Third, building upon the current forward-in-time CIR analysis, the framework allows for the development of a crucial complement that focuses on diagnosing the backward-in-time event attribution to past causes. The forward and backward CIR tools would support distinguishing different types of tipping points in Earth systems, identifying the causes of regime switching, and detecting early warning signals. Finally, continuous-in-time observations are adopted in this work for simplicity of presentation. Nevertheless, an analogous framework can be naturally extended to discrete-in-time observations using the corresponding Bayesian data assimilation algorithms. An interesting scientific question in this context is to understand the uncertainty in causal detection arising from the discrete nature of the data, particularly at time intervals between successive observations. This line of inquiry could also highlight an important distinction between ACI and purely data-driven methods. In ACI, the dynamical model provides a natural way to interpolate causal relationships at time instants when observations are unavailable. Therefore, it may help bridge observational gaps and maintain temporal continuity in causal inference.

Funding

The research of N.C. is funded by Office of Naval Research N00014-24-1-2244 and Army Research Office W911NF-23-1-0118. M.A. is partially supported as a research assistant under the second grant. The research of E.B. is supported by the ONR, ARO, DARPA RSDN, and the NIH and NSF under CRCNS.

Data Availability

In Section 4.3.3 of the Supplementary Information (ACI on Real-World ENSO Data), daily and monthly observations for the state variables of the ENSO model were curated from the following reanalysis datasets: [NCEP Global Ocean Data Assimilation System \(GODAS\)](#) and [NCEP-NCAR Reanalysis 1 Project](#). All other data in the simulations are model-generated.

Code Availability

The MATLAB code used in the analyses and to generate the figures in this work can be found in the following GitHub repository: https://github.com/marandmath/ACI_code. The codebase also

includes implementations for additional experiments and real-world observations that can be used for ACI and CIR analysis in the ENSO case study.

Main Text References

- [1] Jeffrey L Anderson. Localization and sampling error correction in ensemble Kalman filter data assimilation. *Monthly Weather Review*, 140(7):2359–2371, 2012.
- [2] Jeffrey L Anderson and Nancy Collins. Scalable implementations of ensemble filter algorithms for data assimilation. *Journal of Atmospheric and Oceanic Technology*, 24(8):1452–1463, 2007.
- [3] Marios Andreou, Nan Chen, and Yingda Li. An Adaptive Online Smoother with Closed-Form Solutions and Information-Theoretic Lag Selection for Conditional Gaussian Nonlinear Systems. *arXiv preprint arXiv:2411.05870*, 2024.
- [4] Joshua D Angrist and Jörn-Steffen Pischke. *Mostly harmless econometrics: An empiricist’s companion*. Princeton university press, 2009.
- [5] Lionel Barnett, Adam B Barrett, and Anil K Seth. Granger causality and transfer entropy are equivalent for Gaussian variables. *Physical review letters*, 103(23):238701, 2009.
- [6] Jennie E Brand, Xiang Zhou, and Yu Xie. Recent developments in causal inference and machine learning. *Annual Review of Sociology*, 49(1):81–110, 2023.
- [7] Carlo Cafaro, Warren M Lord, Jie Sun, and Erik M Bollt. Causation entropy from symbolic representations of dynamical systems. *Chaos: An interdisciplinary journal of nonlinear science*, 25(4), 2015.
- [8] Antonietta Capotondi, Andrew T Wittenberg, Matthew Newman, Emanuele Di Lorenzo, Jin-Yi Yu, Pascale Braconnot, Julia Cole, Boris Dewitte, Benjamin Giese, Eric Guilyardi, et al. Understanding ENSO diversity. *Bulletin of the American Meteorological Society*, 96(6):921–938, 2015.
- [9] Alberto Carrassi, Marc Bocquet, Alexis Hannart, and Michael Ghil. Estimating model evidence using data assimilation. *Quarterly Journal of the Royal Meteorological Society*, 143(703):866–880, 2017.
- [10] Nan Chen. *Stochastic Methods for Modeling and Predicting Complex Dynamical Systems*. Springer, 2023.
- [11] Nan Chen, Xianghui Fang, and Jin-Yi Yu. A multiscale model for El Niño complexity. *npj Climate and Atmospheric Science*, 5(1):16, 2022.
- [12] Allan J Clarke. *An introduction to the dynamics of El Niño and the Southern Oscillation*. Elsevier, 2008.
- [13] Thomas M Cover. *Elements of information theory*. John Wiley & Sons, 1999.
- [14] Luisa D’Amore, Rossella Arcucci, Luisa Carracciuolo, and Almerico Murli. A scalable approach for variational data assimilation. *Journal of Scientific Computing*, 61(2):239–257, 2014.
- [15] Geir Evensen. The ensemble Kalman filter: Theoretical formulation and practical implementation. *Ocean dynamics*, 53(4):343–367, 2003.
- [16] Geir Evensen, Femke C Vossepoel, and Peter Jan Van Leeuwen. *Data assimilation fundamentals: A unified formulation of the state and parameter estimation problem*. Springer Nature, 2022.

- [17] Fabrizio Falasca, Pavel Perezhogin, and Laure Zanna. Causal inference in spatiotemporal climate fields through linear response theory. *arXiv preprint arXiv:2306.14433*, 2023.
- [18] Alison Fowler and Peter Jan Van Leeuwen. Observation impact in data assimilation: the effect of non-Gaussian observation error. *Tellus A: Dynamic Meteorology and Oceanography*, 65(1):20035, 2013.
- [19] Stefan Frenzel and Bernd Pompe. Partial mutual information for coupling analysis of multivariate time series. *Physical review letters*, 99(20):204101, 2007.
- [20] Colin Graber and Alexander Schwing. Dynamic neural relational inference for forecasting trajectories. In *Proceedings of the IEEE/CVF Conference on Computer Vision and Pattern Recognition Workshops*, pages 1018–1019, 2020.
- [21] Clive WJ Granger. Investigating causal relations by econometric models and cross-spectral methods. *Econometrica: journal of the Econometric Society*, pages 424–438, 1969.
- [22] Alexis Hannart, Alberto Carrassi, Marc Bocquet, Michael Ghil, Philippe Naveau, Manuel Pulido, Juan Ruiz, and Pierre Tandeo. DADA: data assimilation for the detection and attribution of weather and climate-related events. *Climatic Change*, 136:155–174, 2016.
- [23] Alexis Hannart, J Pearl, FEL Otto, P Naveau, and M Ghil. Causal counterfactual theory for the attribution of weather and climate-related events. *Bulletin of the American Meteorological Society*, 97(1):99–110, 2016.
- [24] Fei-Fei Jin. An equatorial ocean recharge paradigm for ENSO. Part I: Conceptual model. *Journal of the atmospheric sciences*, 54(7):811–829, 1997.
- [25] Murat Kocaoglu, Karthikeyan Shanmugam, and Elias Bareinboim. Experimental design for learning causal graphs with latent variables. *Advances in Neural Information Processing Systems*, 30, 2017.
- [26] Kody Law, Andrew Stuart, and Kostas Zygalakis. Data assimilation. *Cham, Switzerland: Springer*, 214:52, 2015.
- [27] X San Liang and Richard Kleeman. Information transfer between dynamical system components. *Physical review letters*, 95(24):244101, 2005.
- [28] Valerio Lucarini and Mickaël D Chekroun. Detecting and attributing change in climate and complex systems: Foundations, Green’s functions, and nonlinear fingerprints. *Physical Review Letters*, 133(24):244201, 2024.
- [29] Andrew J Majda and Nan Chen. Model error, information barriers, state estimation and prediction in complex multiscale systems. *Entropy*, 20(9):644, 2018.
- [30] Andrew J Majda and John Harlim. Physics constrained nonlinear regression models for time series. *Nonlinearity*, 26(1):201–217, November 2012.
- [31] Dan Mønster, Riccardo Fusaroli, Kristian Tylén, Andreas Roepstorff, and Jacob F Sherson. Causal inference from noisy time-series data—testing the convergent cross-mapping algorithm in the presence of noise and external influence. *Future Generation Computer Systems*, 73:52–62, 2017.
- [32] SL Morgan. *Counterfactuals and causal inference*. Cambridge University Press, 2015.
- [33] Judea Pearl et al. Models, reasoning and inference. *Cambridge, UK: CambridgeUniversityPress*, 19(2):3, 2000.

- [34] Jonas Peters, Dominik Janzing, and Bernhard Schölkopf. *Elements of causal inference: foundations and learning algorithms*. The MIT Press, 2017.
- [35] Mattia Proserpi, Yi Guo, Matt Sperrin, James S Koopman, Jae S Min, Xing He, Shannan Rich, Mo Wang, Iain E Buchan, and Jiang Bian. Causal inference and counterfactual prediction in machine learning for actionable healthcare. *Nature Machine Intelligence*, 2(7):369–375, 2020.
- [36] Alexander Radebach, Reik V Donner, Jakob Runge, Jonathan F Donges, and Jürgen Kurths. Disentangling different types of El Niño episodes by evolving climate network analysis. *Physical Review E—Statistical, Nonlinear, and Soft Matter Physics*, 88(5):052807, 2013.
- [37] Sebastian Reich and Colin Cotter. *Probabilistic forecasting and Bayesian data assimilation*. Cambridge University Press, 2015.
- [38] Boris L. Rozovsky and Sergey V. Lototsky. *Stochastic Evolution Systems: Linear Theory and Applications to Non-Linear Filtering*, volume 89. Springer Science & Business Media, 2018.
- [39] Donald B Rubin. Estimating causal effects of treatments in randomized and nonrandomized studies. *Journal of educational Psychology*, 66(5):688, 1974.
- [40] Jakob Runge, Sebastian Bathiany, Erik Bollt, Gustau Camps-Valls, Dim Coumou, Ethan Deyle, Clark Glymour, Marlene Kretschmer, Miguel D Mahecha, Jordi Muñoz-Marí, et al. Inferring causation from time series in earth system sciences. *Nature communications*, 10(1):2553, 2019.
- [41] Jakob Runge, Jobst Heitzig, Norbert Marwan, and Jürgen Kurths. Quantifying causal coupling strength: A lag-specific measure for multivariate time series related to transfer entropy. *Physical Review E—Statistical, Nonlinear, and Soft Matter Physics*, 86(6):061121, 2012.
- [42] Jakob Runge, Peer Nowack, Marlene Kretschmer, Seth Flaxman, and Dino Sejdinovic. Detecting and quantifying causal associations in large nonlinear time series datasets. *Science advances*, 5(11):eaau4996, 2019.
- [43] Jakob Runge, Vladimir Petoukhov, Jonathan F Donges, Jaroslav Hlinka, Nikola Jajcay, Martin Vejmelka, David Hartman, Norbert Marwan, Milan Paluš, and Jürgen Kurths. Identifying causal gateways and mediators in complex spatio-temporal systems. *Nature communications*, 6(1):8502, 2015.
- [44] Adam Rupe, Derek DeSantis, Craig Bakker, Parvathi Kooloth, and Jian Lu. Causal discovery in nonlinear dynamical systems using Koopman operators. *arXiv preprint arXiv:2410.10103*, 2024.
- [45] Edward S Sarachik and Mark A Cane. *The El Nino-southern oscillation phenomenon*. Cambridge University Press, 2010.
- [46] Simo Särkkä and Lennart Svensson. *Bayesian filtering and smoothing*, volume 17. Cambridge university press, 2023.
- [47] Thomas Schreiber. Measuring information transfer. *Physical review letters*, 85(2):461, 2000.
- [48] Karthikeyan Shanmugam, Murat Kocaoglu, Alexandros G Dimakis, and Sriram Vishwanath. Learning causal graphs with small interventions. *Advances in Neural Information Processing Systems*, 28, 2015.
- [49] George Sugihara, Robert May, Hao Ye, Chih-hao Hsieh, Ethan Deyle, Michael Fogarty, and Stephan Munch. Detecting causality in complex ecosystems. *science*, 338(6106):496–500, 2012.
- [50] Jie Sun and Erik M Bollt. Causation entropy identifies indirect influences, dominance of neighbors and anticipatory couplings. *Physica D: Nonlinear Phenomena*, 267:49–57, 2014.

- [51] Jie Sun, Dane Taylor, and Erik M Bollt. Causal network inference by optimal causation entropy. *SIAM Journal on Applied Dynamical Systems*, 14(1):73–106, 2015.
- [52] Sumanth Varambally, Yi-An Ma, and Rose Yu. Discovering mixtures of structural causal models from time series data. *arXiv preprint arXiv:2310.06312*, 2023.
- [53] J Vialard, F-F Jin, MJ McPhaden, A Fedorov, W Cai, S-I An, D Dommenges, X Fang, MF Stuecker, C Wang, et al. The El Niño Southern Oscillation (ENSO) recharge oscillator conceptual model: Achievements and future prospects. *Reviews of Geophysics*, 63(1):e2024RG000843, 2025.
- [54] Qin Xu. Measuring information content from observations for data assimilation: Relative entropy versus Shannon entropy difference. *Tellus A: Dynamic Meteorology and Oceanography*, 59(2):198–209, 2007.
- [55] Xueli Yang, Zhi-Hua Wang, Chenghao Wang, and Ying-Cheng Lai. Finding causal gateways of precipitation over the contiguous United States. *Geophysical Research Letters*, 50(4):e2022GL101942, 2023.
- [56] Hao Ye, Ethan R Deyle, Luis J Gilarranz, and George Sugihara. Distinguishing time-delayed causal interactions using convergent cross mapping. *Scientific reports*, 5(1):14750, 2015.

Supplementary Information

SI. A Mathematical Foundations and Theoretical Analysis of Assimilative Causal Inference

A.1 Mathematical Framework and Notational Conventions

In this document, **boldface** variables denote multidimensional quantities. Specifically, lowercase boldface variables denote column vectors, while Uppercase ones denote matrices. The only exception is \mathbf{W} (with some subscript), which denotes a vector-valued Wiener process due to literary tradition. Furthermore, for simplicity, we follow the notational convention from physics and do not distinguish between random variables and their realizations.

Let $\mathcal{B} = (\Omega, \mathcal{F}, \mathbb{F}, \mathbb{P})$ be an augmented probability space for filtering over the time interval $[0, T]$, $T \in (0, +\infty)$. Denote by $(\mathbf{x}(t, \omega), \mathbf{y}(t, \omega)) \in \mathbb{R}^{k+l}$, for $t \in [0, T]$ and $\omega \in \Omega$, a $(k+l)$ -dimensional partially observable stochastic process on \mathcal{B} , where \mathbf{x} is the k -dimensional observable component while \mathbf{y} is the l -dimensional unobservable part. Without loss of generality, we consider real-valued processes, otherwise we work with the real-valued joint vector formed by the real and imaginary parts of (\mathbf{x}, \mathbf{y}) and for notational simplicity we henceforth drop the sample space (Ω) dependence, but it is always implied. We assume (\mathbf{x}, \mathbf{y}) is adapted to the filtration \mathbb{F} and that $\mathbf{x}(s \leq t)$ represents a realization of \mathbf{x} over $[0, t]$, i.e., a time series for a fixed $\omega \in \Omega$. For convenience, the time series of \mathbf{x} is assumed to be continuously observed, with the development of an analogous framework for discrete-in-time observations being possible. Finally, for explicitness, we hereafter write $(\cdot | \mathbf{x}(s \leq t))$ to indicate the fact that we are conditioning on the σ -algebra generated by $\{\mathbf{x}(s)\}_{s \leq t}$.

A.2 Bayesian Data Assimilation with Continuous-Time Observations

The assimilative causal inference (ACI) framework builds fundamentally upon Bayesian data assimilation methods. Here we outline their essential mathematical formulation, particularly as applied to probabilistic state estimation in complex turbulent dynamical systems.

A.2.1 Underlying Dynamics

We assume that the evolution of the partially observed process (\mathbf{x}, \mathbf{y}) is governed by the following stochastic system of coupled Itô diffusions over $t \in [0, T]$ [26]:

$$d\mathbf{x}(t) = \mathbf{f}^{\mathbf{x}}(t, \mathbf{x}, \mathbf{y})dt + \Sigma_1^{\mathbf{x}}(t, \mathbf{x}, \mathbf{y})d\mathbf{W}_1(t) + \Sigma_2^{\mathbf{x}}(t, \mathbf{x}, \mathbf{y})d\mathbf{W}_2(t), \quad (1.1a)$$

$$d\mathbf{y}(t) = \mathbf{f}^{\mathbf{y}}(t, \mathbf{x}, \mathbf{y})dt + \Sigma_1^{\mathbf{y}}(t, \mathbf{x}, \mathbf{y})d\mathbf{W}_1(t) + \Sigma_2^{\mathbf{y}}(t, \mathbf{x}, \mathbf{y})d\mathbf{W}_2(t), \quad (1.1b)$$

where $\mathbf{W}_1 \in \mathbb{R}^{d_1}$ and $\mathbf{W}_2 \in \mathbb{R}^{d_2}$ are two real-valued independent Wiener processes that are also independent from the distribution of $(\mathbf{x}(0), \mathbf{y}(0))$. We note that all subsequent random ordinary and stochastic differential equations in this document are written in differential form. In (1.1), we assume the following [26, 12, 23]. (I) Almost every sample path of \mathbf{x} and \mathbf{y} is continuous in $[0, T]$. (II) The functions appearing in (1.1) are predictable for each $\mathbf{x} \in \mathbb{R}^k$ and $\mathbf{y} \in \mathbb{R}^l$. (III) Sufficient regularity conditions are enforced such that (1.1) has a unique solution. (IV) The diffusion coefficients of \mathbf{x} do not depend on \mathbf{y} : $\Sigma_m^{\mathbf{x}}(t, \mathbf{x}, \mathbf{y}) = \Sigma_m^{\mathbf{x}}(t, \mathbf{x})$, for $m = 1, 2$. (V) The sum of the row-based Gramians of the observational noise feedback matrices, $(\Sigma^{\mathbf{x}} \circ \Sigma^{\mathbf{x}})(t, \mathbf{x}) := \Sigma_1^{\mathbf{x}}(t, \mathbf{x})\Sigma_1^{\mathbf{x}}(t, \mathbf{x})^T + \Sigma_2^{\mathbf{x}}(t, \mathbf{x})\Sigma_2^{\mathbf{x}}(t, \mathbf{x})^T$, is invertible for each $t \in [0, T]$ and $\mathbf{x} \in \mathbb{R}^k$.

(IV)–(V) function as identifiability conditions, since they ensure that the conditional distribution of \mathbf{y} given the data of \mathbf{x} contains all available information about \mathbf{y} in (1.1) [26].

A.2.2 Bayesian Data Assimilation

Bayesian data assimilation provides a probabilistic state estimation for the unobserved variables $\mathbf{y}(t)$ conditioned on the observations of \mathbf{x} . The process consists of two sequential steps:

- *Forecast step*: Forward integration of (1.1) generates a model-based prior distribution for the unobserved state $\mathbf{y}(t)$.
- *Analysis step*: Observational data of \mathbf{x} is assimilated into the forecast through Bayesian updating, reducing the uncertainty and bias in the estimation of $\mathbf{y}(t)$.

In Bayesian data assimilation for state estimation, the prior distribution (obtained from model forecasts) is combined with the likelihood of observations through Bayes' theorem, yielding an updated posterior distribution.

A.2.3 Filter and Smoother

Bayesian data assimilation is naturally divided into two approaches based on the assimilated observational time window during analysis: filtering incorporates only current and past observations ($\mathbf{x}(s \leq t)$), while smoothing additionally utilizes future data ($\mathbf{x}(s \leq T)$), typically producing more accurate estimates through the broader temporal context.

Under mild spatial regularity assumptions on the parameters in (1.1), both the filter and smoother distributions are absolutely continuous with respect to the Lebesgue measure on [26]. This guarantees the existence of their probability density functions (PDFs) for all $t \in [0, T]$, which we define as:

$$\begin{aligned} \textbf{Filter: } p_t^f(\mathbf{y}|\mathbf{x}) &:= p(\mathbf{y}(t)|\mathbf{x}(s \leq t)), \\ \textbf{Smoother: } p_t^s(\mathbf{y}|\mathbf{x}) &:= p(\mathbf{y}(t)|\mathbf{x}(s \leq T)). \end{aligned} \quad (1.2)$$

A.3 Explicit Expression of the ACI Framework for Gaussian Distributions

The relative entropy (also known as the Kullback-Leibler divergence) between two given PDFs $p(\mathbf{u})$ and $q(\mathbf{u})$ is defined as [17]:

$$\mathcal{P}(p(\mathbf{u}), q(\mathbf{u})) = \int p(\mathbf{u}) \log \left(\frac{p(\mathbf{u})}{q(\mathbf{u})} \right) d\mathbf{u}, \quad (1.3)$$

which is positive unless $p(\mathbf{u}) = q(\mathbf{u})$ and is invariant under general nonlinear changes of the state variables. If

$$\mathcal{P}(p_t^s(\mathbf{y}|\mathbf{x}), p_t^f(\mathbf{y}|\mathbf{x})) > 0 \quad (1.4)$$

holds at time $t \in [0, T]$, we can then establish an instantaneous assimilative causal link where $\mathbf{y}(t)$ is identified as the cause of \mathbf{x} under the ACI framework, which we denote as:

$$\mathbf{y}(t) \rightarrow \mathbf{x}. \quad (1.5)$$

In the main text, ACI is formulated through \mathcal{P} . Nonetheless, the ACI framework is divergence-independent, so other f -divergences can be adopted as to measure the discrepancy between the filter and smoother distributions. This is because their positive-definiteness solely depends on the PDFs themselves.

The relative entropy (1.3) benefits from a simple and explicit formula when the distributions p and q are real-valued Gaussian densities. Specifically, for $p(\mathbf{u})$ being the PDF of $\mathcal{N}_M(\boldsymbol{\mu}_p, \mathbf{R}_p)$ and $q(\mathbf{u})$ of $\mathcal{N}_M(\boldsymbol{\mu}_q, \mathbf{R}_q)$, then [4, 16]:

$$\mathcal{P}(p(\mathbf{u}), q(\mathbf{u})) = \frac{1}{2}(\boldsymbol{\mu}_p - \boldsymbol{\mu}_q)^\top \mathbf{R}_q^{-1}(\boldsymbol{\mu}_p - \boldsymbol{\mu}_q) + \frac{1}{2} \left(\text{tr}(\mathbf{R}_p \mathbf{R}_q^{-1}) - M - \log(\det(\mathbf{R}_p \mathbf{R}_q^{-1})) \right), \quad (1.6)$$

where M is the dimension of the PDFs. The quadratic-form term on the right-hand side of (1.6) is called the signal and measures the information gain in the mean which is weighted by \mathbf{R}_q^{-1} , while the second term is called the dispersion and involves only the covariance ratio $\mathbf{R}_p\mathbf{R}_q^{-1}$. Hence, (1.6) is known as the signal-dispersion decomposition.

In Algorithm 1 we provide a brief outline of how to implement ACI in pseudocode.

Algorithm 1: ACI for the identification of $\mathbf{y}(t) \rightarrow \mathbf{x}$ over $t \in [0, T]$

Data: Observations of \mathbf{x} in $[0, T]$ (continuous or discrete), $p_0^f(\mathbf{y}|\mathbf{x})$

Result: $\mathcal{P}(p_t^s(\mathbf{y}|\mathbf{x}), p_t^f(\mathbf{y}|\mathbf{x}))$ for $t \in [0, T]$, used to assess $\mathbf{y}(t) \rightarrow \mathbf{x}$ at each time

```

1 for  $0 \leq t \leq T$  do
2   | Use (1.1) and the observations of  $\mathbf{x}$  to compute  $p_t^f(\mathbf{y}|\mathbf{x})$ ; /* E.g., see (1.8)-(1.10) for (1.1)
   |   or Theorem B.1 for the system in (2.1)
3 end
4 for  $T \geq t \geq 0$  (moving backward) do
5   | Use  $p_t^f(\mathbf{y}|\mathbf{x})$  and the observations of  $\mathbf{x}$  to compute  $p_t^s(\mathbf{y}|\mathbf{x})$ ; /* E.g., see (1.11)-(1.12) for
   |   (1.1) or Theorem B.2 for the system in (2.1)
6 end
7 for  $0 \leq t \leq T$  do
8   | Calculate  $\mathcal{P}(p_t^s(\mathbf{y}|\mathbf{x}), p_t^f(\mathbf{y}|\mathbf{x})) = \int p_t^s(\mathbf{y}|\mathbf{x}) \log \left( \frac{p_t^s(\mathbf{y}|\mathbf{x})}{p_t^f(\mathbf{y}|\mathbf{x})} \right) d\mathbf{y}(t)$ ; /* Can also use any other
   |   type of information metric, e.g., a different  $f$ -divergence
9   | if  $\mathcal{P}(p_t^s(\mathbf{y}|\mathbf{x}), p_t^f(\mathbf{y}|\mathbf{x})) > 0$  then
10  |   |  $\mathbf{y}(t) \rightarrow \mathbf{x}$ ;
11  |   | else
12  |   |   |  $\mathbf{y}(t) \not\rightarrow \mathbf{x}$ ;
13  |   | end
14 end

```

A.4 Conditional ACI in the Presence of Additional Non-Target Variables

To discuss conditional ACI, which handles the case where additional non-target (or ancillary) variables are present, we split the observed variables \mathbf{x} into $(\mathbf{x}_A, \mathbf{x}_B) \in \mathbb{R}^{k_A+k_B}$, where $k = k_A + k_B$. We aim to determine whether \mathbf{y} is the cause of \mathbf{x}_A in the presence of the remaining interfering variables \mathbf{x}_B . Recall that $\mathbf{y}(t) \rightarrow \mathbf{x}$ is assessed by quantifying the uncertainty reduction in the smoother distribution beyond the filter one:

$$\mathcal{P}(p_t^s(\mathbf{y}|\mathbf{x}_A, \mathbf{x}_B), p_t^f(\mathbf{y}|\mathbf{x}_A, \mathbf{x}_B)), \quad t \in [0, T]. \quad (1.7)$$

Since \mathbf{x}_B interacts with both \mathbf{x}_A and \mathbf{y} in (1.1), it directly affects the state estimation of $\mathbf{y}(t)$. Therefore, establishing an instantaneous conditional assimilative causal link from $\mathbf{y}(t)$ to \mathbf{x}_A beyond \mathbf{x}_B requires careful treatment of \mathbf{x}_B 's contributions in (1.7).

To accurately assess \mathbf{x}_B 's influence on $\mathbf{y}(t)$'s estimation for establishing the conditional assimilative causal link from $\mathbf{y}(t)$ to \mathbf{x}_A beyond the presence of \mathbf{x}_B , we have to examine its contributions during the two-step Bayesian data assimilation pipeline: (1) through the model dynamics during the forecast step, and (2) via the likelihood distribution during the analysis step. This systematic approach allows us to isolate and remove \mathbf{x}_B 's effects on the state estimation of $\mathbf{y}(t)$, thereby ensuring the measured uncertainty reduction in $\mathbf{y}(t)$ stems solely from \mathbf{x}_A 's influence.

A.4.1 Analyzing how \mathbf{x}_B Affects the State Estimation of $\mathbf{y}(t)$

To analytically characterize how non-target variables \mathbf{x}_B influence the $\mathbf{y}(t)$ estimation during Bayesian data assimilation, it suffices to examine the governing evolution equations for the unnormalized filter and smoother densities associated with (1.1) [26, 19]. Under sufficient regularity conditions, we have that the unnormalized filter density $u_t^f(\mathbf{y}|\mathbf{x})$ satisfies a linear random partial differential equation (PDE) for $0 \leq t \leq T$:

$$\partial u_t^f(\mathbf{y}|\mathbf{x}) = \underbrace{\mathcal{L}^* u_t^f(\mathbf{y}|\mathbf{x}) dt}_{\text{Forecast}} + \underbrace{\mathcal{M}^* u_t^f(\mathbf{y}|\mathbf{x}) \cdot d\mathbf{x}}_{\text{Analysis}}, \quad (1.8)$$

where \mathcal{L}^* is the *forward Kolmogorov* or *Fokker-Planck operator*:

$$\mathcal{L}^* u_t(\mathbf{y}) := -\nabla_{\mathbf{y}} \cdot (\mathbf{f}^{\mathbf{y}} u_t) + \frac{1}{2} \nabla_{\mathbf{y}} \cdot \nabla_{\mathbf{y}} \cdot ((\Sigma^{\mathbf{y}} \circ \Sigma^{\mathbf{y}}) u_t), \quad (1.9)$$

and \mathcal{M}^* is the *forward* or *filter Kalman update operator*:

$$\mathcal{M}^* u_t(\mathbf{y}) := (\Sigma^{\mathbf{x}} \circ \Sigma^{\mathbf{x}})^{-1/2} \left(-\nabla_{\mathbf{y}} \cdot ((\Sigma^{\mathbf{x}} \circ \Sigma^{\mathbf{x}})^{-1/2} (\Sigma^{\mathbf{x}} \circ \Sigma^{\mathbf{y}}) u_t) + (\Sigma^{\mathbf{x}} \circ \Sigma^{\mathbf{x}})^{-1/2} \mathbf{f}^{\mathbf{x}} u_t \right), \quad (1.10)$$

while the unnormalized smoother density $u_t^s(\mathbf{y}|\mathbf{x})$ satisfies a backward linear random PDE for $T \geq t \geq 0$:

$$\overleftarrow{\partial} u_t^s(\mathbf{y}|\mathbf{x}) = \underbrace{\mathcal{L} u_t^s(\mathbf{y}|\mathbf{x}) dt}_{\text{Forecast}} + \underbrace{\mathcal{M} u_t^s(\mathbf{y}|\mathbf{x}) \cdot \overleftarrow{d}\mathbf{x}}_{\text{Analysis}}, \quad (1.11)$$

where \mathcal{L} is the *backward Kolmogorov operator* and formal adjoint of \mathcal{L}^* in (1.9), while \mathcal{M} is the *backward* or *smoother Kalman update operator* and formal adjoint of the operator \mathcal{M}^* appearing in (1.10), which are both explicitly given by:

$$\mathcal{L} u_t(\mathbf{y}) = \mathbf{f}^{\mathbf{y}} \cdot \nabla_{\mathbf{y}} u_t + \frac{1}{2} \text{tr}((\Sigma^{\mathbf{y}} \circ \Sigma^{\mathbf{y}}) \nabla_{\mathbf{y}}^2 u_t), \quad (1.12a)$$

$$\mathcal{M} u_t(\mathbf{y}) = (\Sigma^{\mathbf{x}} \circ \Sigma^{\mathbf{x}})^{-1/2} \left((\Sigma^{\mathbf{x}} \circ \Sigma^{\mathbf{x}})^{-1/2} (\Sigma^{\mathbf{x}} \circ \Sigma^{\mathbf{y}}) \nabla_{\mathbf{y}} u_t + (\Sigma^{\mathbf{x}} \circ \Sigma^{\mathbf{x}})^{-1/2} \mathbf{f}^{\mathbf{x}} u_t \right). \quad (1.12b)$$

The diffusion interactions $(\Sigma^{\mathbf{y}} \circ \Sigma^{\mathbf{y}})$ and $(\Sigma^{\mathbf{x}} \circ \Sigma^{\mathbf{y}})$ are defined in the same manner as $\Sigma^{\mathbf{x}} \circ \Sigma^{\mathbf{x}}$, while $\overleftarrow{\partial} u_t^s$ and $\overleftarrow{d}\mathbf{x}$ denote backward stochastic Itô integrals (i.e., the negative of the usual differentials up to the principal (linear) part).

A.4.2 Managing the Influence of \mathbf{x}_B on $\mathbf{y}(t)$'s Estimation

From (1.8) and (1.11), we can deduce that as to eliminate the effect of \mathbf{x}_B on the state estimation of $\mathbf{y}(t)$, while retaining only \mathbf{x}_A 's observational influence, we can simply assign infinite uncertainty to \mathbf{x}_B during the analysis step. This follows from the Kalman update's inverse dependence on the observational uncertainty in (1.10) and (1.12b). This manipulation effectively nullifies \mathbf{x}_B 's contributions to the state update, thus preventing it from impacting the uncertainty reduction (the key mechanism behind ACI), while still preserving its role in the forecast dynamics.

Implementation via posterior densities. We implement this proposition through a formal limit operation on the posterior filter and smoother PDFs (normalizations of the densities in (1.8) and (1.11), respectively), therefore defining for each $t \in [0, T]$:

$$p_t^{\text{fl}\mathbf{x}_B}(\mathbf{y}|\mathbf{x}_A) := \lim_{\text{Var}(\mathbf{x}_B(t)) \rightarrow +\infty} p(\mathbf{y}(t) | \mathbf{x}_A(s \leq t), \mathbf{x}_B(s \leq t)) \quad (1.13a)$$

$$p_t^{\text{sl}\mathbf{x}_B}(\mathbf{y}|\mathbf{x}_A) := \lim_{\text{Var}(\mathbf{x}_B(t)) \rightarrow +\infty} p(\mathbf{y}(t) | \mathbf{x}_A(s \leq T), \mathbf{x}_B(s \leq T)) \quad (1.13b)$$

The limit $\text{Var}(\mathbf{x}_B(t)) \rightarrow +\infty$ represents taking \mathbf{x}_B 's marginal likelihood uncertainty to infinity, which removes \mathbf{x}_B 's influence in the Kalman updates, which occurs through the Kalman gain's effect on the innovation process in (1.10) and (1.12b), while preserving its dynamic role during forecasts in (1.9) and (1.12a).

Conditional assimilative causal links. Using the distributions in (1.13), we generalize the ACI framework. When:

$$\mathcal{P}\left(p_t^{s|\mathbf{x}_B}(\mathbf{y}|\mathbf{x}_A), p_t^{f|\mathbf{x}_B}(\mathbf{y}|\mathbf{x}_A)\right) > 0, \quad (1.14)$$

we establish a *conditional assimilative causal link* at $t \in [0, T]$, denoted as:

$$\left(\mathbf{y}(t) \rightarrow \mathbf{x}_A\right)\Big|_{\mathbf{x}_B}. \quad (1.15)$$

This indicates $\mathbf{y}(t)$ as the cause of \mathbf{x}_A conditioned on \mathbf{x}_B when the relative entropy between the smoother- and filter-based distributions in (1.13) is nonzero.

In Algorithm 2 we provide a brief outline of how to implement conditional ACI in pseudocode.

Algorithm 2: Conditional ACI for the identification of $\left(\mathbf{y}(t) \rightarrow \mathbf{x}_A\right)\Big|_{\mathbf{x}_B}$ over $t \in [0, T]$

Data: Observations of \mathbf{x} in $[0, T]$ (continuous or discrete), $p_0^f(\mathbf{y}|\mathbf{x})$

Result: $\mathcal{P}\left(p_t^{s|\mathbf{x}_B}(\mathbf{y}|\mathbf{x}_A), p_t^{f|\mathbf{x}_B}(\mathbf{y}|\mathbf{x}_A)\right)$ for $t \in [0, T]$, used to assess $\left(\mathbf{y}(t) \rightarrow \mathbf{x}_A\right)\Big|_{\mathbf{x}_B}$ at each time

```

1 for  $0 \leq t \leq T$  do
2   Use (1.1) and the observations of  $\mathbf{x} = (\mathbf{x}_A, \mathbf{x}_B)^T$  to compute  $p_t^{f|\mathbf{x}_B}(\mathbf{y}|\mathbf{x}_A)$  by letting
    $\text{Var}(\mathbf{x}_B(t)) \rightarrow +\infty$  during the corresponding analysis step of Bayesian data assimilation,
   defined by the forward/filter Kalman update operator  $\mathcal{M}^*$  in (1.10); /* E.g., see Theorem
   B.1 and the proof of Theorem C.2 for the system in (2.1) as a concrete example
3 end
4 for  $T \geq t \geq 0$  (moving backward) do
5   Use  $p_t^{f|\mathbf{x}_B}(\mathbf{y}|\mathbf{x}_A)$  and the observations of  $\mathbf{x} = (\mathbf{x}_A, \mathbf{x}_B)^T$  to compute  $p_t^{s|\mathbf{x}_B}(\mathbf{y}|\mathbf{x}_A)$  by letting
    $\text{Var}(\mathbf{x}_B(t)) \rightarrow +\infty$  during the corresponding analysis step of Bayesian data assimilation,
   defined by the backward/smoothing Kalman update operator  $\mathcal{M}$  in (1.12b); /* E.g., see
   Theorem B.2 and the proof of Theorem C.2 for the system in (2.1) as a concrete example
6 end
7 for  $0 \leq t \leq T$  do
8   Calculate  $\mathcal{P}\left(p_t^{s|\mathbf{x}_B}(\mathbf{y}|\mathbf{x}_A), p_t^{f|\mathbf{x}_B}(\mathbf{y}|\mathbf{x}_A)\right) = \int p_t^{s|\mathbf{x}_B}(\mathbf{y}|\mathbf{x}_A) \log \left( \frac{p_t^{s|\mathbf{x}_B}(\mathbf{y}|\mathbf{x}_A)}{p_t^{f|\mathbf{x}_B}(\mathbf{y}|\mathbf{x}_A)} \right) d\mathbf{y}(t)$ ; /* Can also
   use any other type of information metric, e.g., a different  $f$ -divergence
9   if  $\mathcal{P}\left(p_t^{s|\mathbf{x}_B}(\mathbf{y}|\mathbf{x}_A), p_t^{f|\mathbf{x}_B}(\mathbf{y}|\mathbf{x}_A)\right) > 0$  then
10      $\left(\mathbf{y}(t) \rightarrow \mathbf{x}_A\right)\Big|_{\mathbf{x}_B}$ ;
11   else
12      $\left(\mathbf{y}(t) \not\rightarrow \mathbf{x}_A\right)\Big|_{\mathbf{x}_B}$ ;
13   end
14 end

```

A.4.3 Arguments in Favor of the Conditional ACI Framework

The generalized ACI framework presented in Section A.4 and defined by (1.13)–(1.14) offers several key advantages for establishing (1.15):

- (1) Complete elimination of \mathbf{x}_B 's influence during data assimilation, ensuring any uncertainty reduction in $\mathbf{y}(t)$ stems solely from \mathbf{x}_A , consistent with our ACI objectives. Furthermore, during

analysis, the correlations between \mathbf{x}_A and \mathbf{x}_B in their likelihood are necessarily sent to zero as the uncertainty of \mathbf{x}_B goes to infinity. This further resolves the potential for spurious associations arising over the observable state space that can flow over when inferring causality from $\mathbf{y}(t)$ to \mathbf{x}_A ; see Theorem C.2. A rough analogue to this approach would be the assignment of an improper prior as an uninformative or diffuse prior in parametric Bayesian inference.

- (2) While discounting \mathbf{x}_B 's observational influence, we retain its time series in $\mathbf{y}(t)$'s estimation, analogous to transfer entropy approaches where conditional causal links account for spurious effects. Our framework naturally conditions on \mathbf{x}_B 's observations while assigning them uniform likelihood weight through the infinite uncertainty assumption.
- (3) Preservation of the original dynamical system structure. Unlike methods that modify dynamics or eliminate governing equations (potentially yielding nonphysical results), our approach maintains model integrity while properly handling \mathbf{x}_B 's spurious contributions through the Bayesian framework.
- (4) Straightforward implementation. When the filter/smoothing distributions in (1.2) solve continuous random PDEs, the limiting distributions in (1.13) emerge naturally under continuous parameter dependence, particularly as $\text{Var}(\mathbf{x}_B(t)) \rightarrow +\infty$ for the relevant covariance matrix elements.

A.4.4 Further Justification: Why Infinite Uncertainty Outperforms Marginalization

To further justify our approach for establishing temporally-varying conditional assimilative causal links in the presence of ancillary variables, consider treating the non-target variables \mathbf{x}_B as unobserved. In this scenario, the smoother PDF at time $t \in [0, T]$ becomes:

$$p_t(\mathbf{y}, \mathbf{x}_B | \mathbf{x}_A(s \leq T)).$$

One might attempt to infer a conditional causal relationship from $\mathbf{y}(t)$ to \mathbf{x}_A by marginalizing over $\mathbf{x}_B(t)$:

$$p_t(\mathbf{y} | \mathbf{x}_A(s \leq T)) = \int p_t(\mathbf{y}, \mathbf{x}_B | \mathbf{x}_A(s \leq T)) d\mathbf{x}_B(t).$$

However, this approach proves problematic even for simple turbulent nonlinear dynamical systems. Crucially, the issue persists even when conditioning on $\mathbf{x}_B(t)$ rather than marginalizing.

The fundamental flaw lies in how correlations between $\mathbf{y}(t)$ and $\mathbf{x}_B(t)$ affect uncertainty reduction during state estimation. These correlations can introduce spurious causal relationships that become unavoidable once the model forecast begins propagating forward, regardless of time-step size. Consider the following causal network:



For this causal chain, this marginalization (or conditioning) method might falsely suggest a direct causal link from $\mathbf{y}(t)$ to \mathbf{x}_A . While these filter- and smoother-based distributions of $\mathbf{y}(t)$ given \mathbf{x}_A may differ after marginalization (or conditioning), we cannot attribute causation to \mathbf{x}_A under (1.4). The uncertainty reduction in $\mathbf{y}(t)$ inherently incorporates information transfer from $\mathbf{x}_B(t)$ due to their coupled dynamics, unlike the distributions in (1.13) where \mathbf{x}_B trajectories are known but carry infinite uncertainty in their likelihood.

A.5 Dynamic Discovery of the Causal Influence Range (CIR)

The relative entropy between the smoother and filter solutions in (1.4) quantifies both the existence and strength of an assimilative causal link from $\mathbf{y}(t)$ to \mathbf{x} . Similarly, the generalized metric in (1.14) measures the conditional causal link $(\mathbf{y}(t) \rightarrow \mathbf{x}_A)|_{\mathbf{x}_B}$ and its intensity. However, these ACI metrics alone cannot determine the *temporal extent* of causal influence, namely, how many future values of \mathbf{x} (or \mathbf{x}_A conditioned on \mathbf{x}_B) are affected by $\mathbf{y}(t)$ over $[t, T]$. We define this temporal characteristic as the causal influence range (CIR), representing the future time window where $\mathbf{y}(t)$'s causal impact persists. Below we develop the theory for unconditional CIR; the conditional case (CCIR) follows analogously by substituting the appropriate equations with those from Section A.4.

In chaotic turbulent systems, new observations of \mathbf{x} influence $\mathbf{y}(t)$'s estimation only within finite time windows. More chaotic dynamics accelerate memory decay, typically exhibiting exponential decay modulated by factors like \mathbf{x} 's signal-to-noise ratio [2]. Our framework estimates this CIR duration for $\mathbf{y}(t) \rightarrow \mathbf{x}$ by determining how many future \mathbf{x} values are meaningfully affected.

For arbitrary $t \in [0, T]$ and $T' \in [t, T]$, we compare two smoother distributions:

- *Complete* smoother $p_t(\mathbf{y}|\mathbf{x}(s \leq T))$: Optimal (minimum variance) estimation using all available data.
- *Lagged* smoothers $p_t(\mathbf{y}|\mathbf{x}(s \leq T'))$: Suboptimal estimations using partial data ($T' \leq T$).

The divergence between these distributions reveals the temporal decay of $\mathbf{y}(t)$'s causal influence on future \mathbf{x} values as T' increases from t toward T .

A.5.1 Quantifying the CIR

The finite nature of the CIR motivates measuring how the complete and lagged smoother distributions differ as functions of observational time $T' \in [t, T]$ when evaluating the recovery of the state of \mathbf{y} at t . We naturally quantify this discrepancy using the relative entropy:

$$\delta(T'; t) := \mathcal{P}(p_t(\mathbf{y}|\mathbf{x}(s \leq T)), p_t(\mathbf{y}|\mathbf{x}(s \leq T'))), \quad 0 \leq t \leq T' \leq T \quad (1.16)$$

where the second input in δ , i.e., t , is the time on which the posterior distributions of \mathbf{y} are evaluated. For analysis, we normalize the domain of δ to $\mathbb{I} = [0, 1]$ via the transformation $h(\tau) = t + \tau(T - t)$:

$$\hat{\delta}(\tau; t) := \delta(t + \tau(T - t); t), \quad \tau \in \mathbb{I}. \quad (1.17)$$

Let $\mathcal{M}(t) := \|\hat{\delta}(\cdot; t)\|_{L^\infty(\mathbb{I})}$ denote the maximum divergence, which exists in practical applications. Notably:

- At $\tau = 1$, $\hat{\delta}(1; t) = 0$ by the positive-definiteness of the relative entropy.
- At $\tau = 0$, $\hat{\delta}(0; t)$ recovers the standard ACI metric from (1.4).
- For $\tau \in (0, 1)$, $\hat{\delta}(\tau; t)$ measures the lack of information from incorporating a limited portion of the future observations of \mathbf{x} after t , i.e., up until $h(\tau)$, $\mathbf{x}(s \leq h(\tau))$, but not up to T .

For chaotic systems, $\mathcal{M}(t)$ typically occurs at $\tau = 0$ or shortly thereafter. The interval where $\hat{\delta}(\tau; t)$ remains large suggests significant causal influence under ACI, since it indicates that there is substantial information gain to be incurred by additionally incorporating the future observations of \mathbf{x} from $[h(\tau), T]$.

Formal definition of the CIR. For a threshold $\varepsilon \geq 0$, define:

$$J_t(\varepsilon) := \{\tau \in [0, 1] : \hat{\delta}(\tau; t) > \varepsilon\}. \quad (1.18)$$

The CIR length of $\mathbf{y}(t) \rightarrow \mathbf{x}$ is then given by:

$$\tilde{\tau}_{\mathbf{y}(t) \rightarrow \mathbf{x}}(\varepsilon) := (T - t) \sup J_t(\varepsilon), \quad (1.19)$$

with the convention $\tilde{\tau}_{\mathbf{y}(t) \rightarrow \mathbf{x}}(\varepsilon) = 0$ when $J_t(\varepsilon) = \emptyset$ (true for $\varepsilon \geq \mathcal{M}(t)$). The associated CIR interval becomes:

$$\widetilde{\text{CIR}}_{\mathbf{y}(t) \rightarrow \mathbf{x}}(\varepsilon) := [t, t + \tilde{\tau}_{\mathbf{y}(t) \rightarrow \mathbf{x}}(\varepsilon)]. \quad (1.20)$$

As aforementioned, for most practical chaotic dynamical systems, the maximum information deficit $\mathcal{M}(t)$ typically occurs at $\tau = 0$ or shortly thereafter. This reflects the characteristic memory decay in such systems, where the influence on the state estimation of $\mathbf{y}(t)$ from the future observations of \mathbf{x} in $[h(\tau), T]$ diminishes with increasing lead time τ . Note also that under the mild assumption that $\hat{\delta}(\cdot; t)$ is Lebesgue measurable for each $t \in [0, T]$, which is a condition satisfied when $\delta(\cdot; t)$ is Borel measurable (that holds for the relative entropy and most complex turbulent systems found in practice), we obtain the fundamental inequality:

$$\tilde{\tau}_{\mathbf{y}(t) \rightarrow \mathbf{x}}(\varepsilon) \geq (T - t) \lambda_I(\mathbf{J}(\varepsilon)), \quad (1.21)$$

where $\lambda_I(\cdot)$ represents the Lebesgue measure restricted to I . Thus, $\widetilde{\text{CIR}}$ provides a liberal estimate of the temporal window where $\mathbf{y}(t)$ causally influences \mathbf{x} .

Interpretation. The decreasing trend of $\delta(T'; t)$ reflects the finite memory of chaotic dynamics:

- $\delta(t; t)$ assesses whether $\mathbf{y}(t) \rightarrow \mathbf{x}$ via ACI.
- $\delta(T; t) = 0$ shows complete information incorporation.
- The significant $\delta(T'; t)$ region marks where $\mathbf{y}(t)$ substantially affects future \mathbf{x} .

A.5.2 Subjective and Objective Perspectives of the CIR

The current CIR framework, while intuitive, introduces subjectivity through its dependence on the threshold parameter ε . We therefore distinguish between two perspectives:

- **Subjective CIR:** Denoted by $\tilde{\tau}_{\mathbf{y}(t) \rightarrow \mathbf{x}}(\varepsilon)$ (length) and $\widetilde{\text{CIR}}_{\mathbf{y}(t) \rightarrow \mathbf{x}}(\varepsilon)$ (interval), marked with tildes to emphasize their ε -dependence.
- **Objective CIR:** An ε -independent alternative developed in the sequel.

Objective CIR definition. The natural objective measure averages the subjective CIR lengths over all possible thresholds:

$$\tau_{\mathbf{y}(t) \rightarrow \mathbf{x}} := \frac{1}{\mathcal{M}(t)} \int_0^{\mathcal{M}(t)} \tilde{\tau}_{\mathbf{y}(t) \rightarrow \mathbf{x}}(\varepsilon) d\varepsilon, \quad t \in [0, T], \quad (1.22)$$

where $\mathcal{M}(t) = \max_{\tau \in [0, 1]} \hat{\delta}(\tau; t)$. Dividing by $\mathcal{M}(t)$ guarantees the unit of the objective CIR is temporal. This averaging process: (a) yields dimensionally consistent results (time units), (b) guarantees $\tau_{\mathbf{y}(t) \rightarrow \mathbf{x}} \in [0, T - t]$, and (c) defaults to 0 when $\mathcal{M}(t) = 0$ (no causal link).

The corresponding objective CIR interval is then defined as:

$$\text{CIR}_{\mathbf{y}(t) \rightarrow \mathbf{x}} := [t, t + \tau_{\mathbf{y}(t) \rightarrow \mathbf{x}}], \quad t \in [0, T]. \quad (1.23)$$

By construction, this objective interval is always contained within the maximal subjective CIR and always contains the minimal one.

Analogy with correlation analysis. These CIR measures parallel concepts in correlation analysis:

- **Subjective CIR** resembles the autocorrelation function (ACF), where memory duration depends on a subjective threshold.
- **Objective CIR** mirrors the decorrelation time, providing a threshold-free measure through integration.

Just as decorrelation time objectively quantifies system memory by integrating the ACF, our objective CIR integrates over all possible thresholds to remove subjectivity, by assigning an impartial uniform weight on each subjective CIR, while capturing the essential temporal influence structure.

A.5.3 Efficient Computation of the Objective CIR

While (1.22) offers a theoretically sound definition of the objective CIR length, its practical implementation faces significant computational challenges. The subjective CIR length $\tilde{\tau}_{\mathbf{y}(t) \rightarrow \mathbf{x}}(\varepsilon)$ generally admits no analytical solution across the full parameter space $\varepsilon \in [0, \mathcal{M}(t)]$ and $t \in [0, T]$. Numerically evaluating the integral in (1.22) requires repeated smoother computations and leads to a computational complexity that scales at best quadratically with the number of discretization points adopted for quadrature.

We overcome this computational limitation by developing an efficient lower-bound approximation that becomes exact when the information loss metric $\delta(T'; t)$ in (1.16) is non-increasing with respect to future observations (i.e., non-increasing in T'). This is the typical case in most applications as the memory usually decays as the lead time increases. The following theorem formalizes this approach, requiring only that $\hat{\delta}(\cdot; t)$ is Lebesgue measurable for each $t \in [0, T]$.

Theorem A.1 (Computing the Objective CIR). *Assume that there exists $\mathcal{M}(t) := \|\hat{\delta}(\cdot; t)\|_{L^\infty(\mathbf{I})} = \|\delta(\cdot; t)\|_{L^\infty([t, T])} > 0$ for each $t \in [0, T]$. Then, for $t \in [0, T]$:*

$$\begin{aligned} \frac{1}{\mathcal{M}(t)} \int_t^T \delta(T'; t) dT' &= \frac{T-t}{\mathcal{M}(t)} \int_0^1 \hat{\delta}(\tau; t) d\tau \\ &= \frac{T-t}{\mathcal{M}(t)} \int_0^{\mathcal{M}(t)} \lambda_{\mathbf{I}}(J_t(\varepsilon)) d\varepsilon \\ &\leq \frac{1}{\mathcal{M}(t)} \int_0^{\mathcal{M}(t)} \tilde{\tau}_{\mathbf{y}(t) \xrightarrow{\text{ACI}} \mathbf{x}}(\varepsilon) d\varepsilon = \tau_{\mathbf{y}(t) \xrightarrow{\text{ACI}} \mathbf{x}}, \end{aligned} \tag{1.24}$$

where $\hat{\delta}(\tau; t)$, $J_t(\varepsilon)$, and $\tilde{\tau}_{\mathbf{y}(t) \xrightarrow{\text{ACI}} \mathbf{x}}(\varepsilon)$ are defined in (1.17), (1.18), and (1.19), respectively. The equality (in the last inequality in (1.24)) is achieved if and only if $\hat{\delta}(\cdot; t)$ is a nonincreasing function in \mathbf{I} . In that case, we also have:

$$\mathcal{M}(t) = \hat{\delta}(0; t) = \delta(t; t) = \mathcal{P}(p_t^s(\mathbf{y}|\mathbf{x}), p_t^f(\mathbf{y}|\mathbf{x})).$$

Proof of Theorem A.1. First, observe that $\lambda_{\mathbf{I}}(\cdot)$ defines a probability measure on $\mathbf{I} = [0, 1]$. Under the Lebesgue measurability assumption for $\hat{\delta}(\cdot; t)$, we can then interpret $\hat{\delta}(\cdot; t)$ as a continuous random variable on the probability space $(\mathbf{I}, \mathcal{L}_{\mathbf{I}}, \lambda_{\mathbf{I}})$, $\mathcal{L}_{\mathbf{I}}$ as the σ -algebra of Lebesgue measurable subsets of \mathbf{I} , where the support of $\hat{\delta}(\cdot; t)$ is $[0, \mathcal{M}(t)]$.

$\hat{\delta}(\cdot; t)$'s survival function $\lambda_{\mathbf{I}}(J_t(\varepsilon))$ is well-defined because (a) it is nonincreasing and right-continuous with left limits, (b) it satisfies $\lambda_{\mathbf{I}}(J_t(\varepsilon)) = 1$ for $\varepsilon \leq 0$, and (c) it satisfies $\lambda_{\mathbf{I}}(J_t(\varepsilon)) = 0$ for $\varepsilon \geq \mathcal{M}(t)$.

Applying the expected survival time formula to this nonnegative, compactly supported random variable yields:

$$\mathbb{E}[\hat{\delta}(\cdot; t)] := \int_0^1 \hat{\delta}(\tau; t) d\tau \equiv \frac{1}{T-t} \int_t^T \delta(T'; t) dT' = \int_0^{\mathcal{M}(t)} \lambda_I(\mathbf{J}_t(\varepsilon)) d\varepsilon.$$

The theorem's main result follows by dividing through by $\mathcal{M}(t) > 0$, multiplying by $T - t$, and applying the inequality in (1.21). The equality condition follows immediately from (1.21), since the equality there holds if and only if $\hat{\delta}(\cdot; t)$ is nonincreasing on I . \blacksquare

The result of Theorem A.1 provides a consistent and computationally efficient way to approximate from below the objective CIR length:

$$\tau_{\mathbf{y}(t) \rightarrow \mathbf{x}}^{\text{approx}} := \frac{T-t}{\mathcal{M}(t)} \int_0^1 \hat{\delta}(\tau; t) d\tau = \frac{1}{\mathcal{M}(t)} \int_t^T \delta(T'; t) dT' \leq \tau_{\mathbf{y}(t) \rightarrow \mathbf{x}}, \quad t \in [0, T]. \quad (1.25)$$

The inequality reduces to an equality precisely when $\hat{\delta}(\cdot; t)$ is nonincreasing on I , which is a condition satisfied in most practical applications. A dimensional analysis of (1.25) reveals that $\tau_{\mathbf{y}(t) \rightarrow \mathbf{x}}^{\text{approx}}$ maintains consistent time units, confirming the physical validity of this approximation. This consistency mirrors the dimensional properties established for the exact objective CIR length in (1.22).

SI. B Analytically Tractable Nonlinear Systems for ACI Analysis

In this section, we introduce a broad class of nonlinear stochastic dynamical systems that possess analytically tractable Bayesian data assimilation solutions. These closed-form solutions allow direct investigation of ACI without relying on ensemble approximation methods.

B.1 Conditional Gaussian Nonlinear Systems (CGNS)

Numerical approximations, such as ensemble or particle methods, have to be adopted to find the filter and smoother solutions for general nonlinear dynamics systems. Nevertheless, analytical solutions are available for the data assimilation solutions for a broad class of nonlinear systems, known as conditional Gaussian nonlinear systems (CGNSs) [19].

B.1.1 The Modeling Framework

A CGNS consists of two Itô diffusion processes and has the following form [19]:

$$d\mathbf{x}(t) = \left(\mathbf{\Lambda}^{\mathbf{x}}(t, \mathbf{x})\mathbf{y}(t) + \mathbf{f}^{\mathbf{x}}(t, \mathbf{x}) \right) dt + \mathbf{\Sigma}_1^{\mathbf{x}}(t, \mathbf{x}) d\mathbf{W}_1(t) + \mathbf{\Sigma}_2^{\mathbf{x}}(t, \mathbf{x}) d\mathbf{W}_2(t), \quad (2.1a)$$

$$d\mathbf{y}(t) = \left(\mathbf{\Lambda}^{\mathbf{y}}(t, \mathbf{x})\mathbf{y}(t) + \mathbf{f}^{\mathbf{y}}(t, \mathbf{x}) \right) dt + \mathbf{\Sigma}_1^{\mathbf{y}}(t, \mathbf{x}) d\mathbf{W}_1(t) + \mathbf{\Sigma}_2^{\mathbf{y}}(t, \mathbf{x}) d\mathbf{W}_2(t). \quad (2.1b)$$

where the matrices $\mathbf{\Lambda}^{\mathbf{x}}$, $\mathbf{\Lambda}^{\mathbf{y}}$, $\mathbf{\Sigma}_1^{\mathbf{x}}$, $\mathbf{\Sigma}_2^{\mathbf{x}}$, $\mathbf{\Sigma}_1^{\mathbf{y}}$, $\mathbf{\Sigma}_2^{\mathbf{y}}$ and the vectors $\mathbf{f}^{\mathbf{x}}$, $\mathbf{f}^{\mathbf{y}}$ can contain arbitrarily nonlinear functions of \mathbf{x} . The state variable \mathbf{y} appears in the system in a conditionally linear way but it can interact nonlinearly with \mathbf{x} . Therefore, the system is overall highly nonlinear and can generate strong non-Gaussian feature in both the marginal and joint distributions, corresponding to extreme events, intermittency, regime switching, etc. When all these matrices and vectors become only a function of time, i.e., they do not depend on \mathbf{x} , then the filtering and smoothing of (2.1) collapses to the setup of the classical Kalman-Bucy filter [14] and Rauch-Tung-Striebel smoother [24].

The CGNS framework broadly applies to many complex nonlinear systems across disciplines, including physics-constrained stochastic models (e.g., noisy Lorenz systems, low-order Charney-DeVore

flows, and topographic mean-flow interaction paradigms), stochastically coupled reaction-diffusion systems like FitzHugh-Nagumo neural models and SIR epidemic models, and multiscale geophysical flow models such as stochastic Boussinesq equations and forced rotating shallow water equations. This framework has also been successfully adapted to model realistic phenomena like the Madden-Julian oscillation and Arctic sea ice dynamics. See a gallery of examples in [6]. On the other hand, many multiscale systems with general nonlinearities can be effectively approximated as CGNSs with minimal error. In geophysical and fluid systems, where nonlinearities often take quadratic forms, this approximation preserves all nonlinear interactions involving the large-scale variables \mathbf{x} and their couplings with the small-scale fluctuations in \mathbf{y} . Only the self-interactions of \mathbf{y} are replaced by effective noise and damping terms, which is an approach rigorously justified when \mathbf{y} represents fast, unresolved scales. This strategy aligns with the stochastic mode reduction framework developed by Majda, Timofeyev, and Vanden-Eijnden (the MTV method) [21].

The conditional linearity of \mathbf{y} given \mathbf{x} allows closed-form analytic solutions for the posterior distributions of \mathbf{y} in Bayesian data assimilation, despite the overall nonlinearity of the system. This property fundamentally distinguishes CGNSs from linear Gaussian systems. For instance, the posterior covariance evolves according to a random Riccati equation, leading to temporal fluctuations rather than the asymptotic convergence seen in linear cases. These dynamic covariance variations are essential for capturing extreme events and intermittency with high fidelity.

B.1.2 Filtering and Smoothing Distributions for CGNSs

Theorem B.1 (Optimal nonlinear filter state estimation equations for CGNSs [19]). *Let $\mathbf{x}(t)$ and $\mathbf{y}(t)$ satisfy (2.1a)–(2.1b). Then, under suitable regularity conditions, the posterior distribution of $\mathbf{y}(t)$ given a realization of the trajectory \mathbf{x} up to the current time instant t (namely, the optimal filter solution) is Gaussian,*

$$\mathbb{P}(\mathbf{y}(t) | \mathbf{x}(s \leq t)) \stackrel{(d)}{\approx} \mathcal{N}_l(\boldsymbol{\mu}_f(t), \mathbf{R}_f(t)),$$

where

$$\boldsymbol{\mu}_f(t) := \mathbb{E}[\mathbf{y}(t) | \mathbf{x}(s \leq t)] \quad \text{and} \quad \mathbf{R}_f(t) := \mathbb{E}[(\mathbf{y}(t) - \boldsymbol{\mu}_f(t))(\mathbf{y}(t) - \boldsymbol{\mu}_f(t))^T | \mathbf{x}(s \leq t)],$$

are the unique continuous solutions to the system of optimal nonlinear filter equations for $0 \leq t \leq T$:

$$d\boldsymbol{\mu}_f(t) = (\boldsymbol{\Lambda}^y \boldsymbol{\mu}_f + \mathbf{f}^y)dt + \mathbf{K}_f(d\mathbf{x} - (\boldsymbol{\Lambda}^x \boldsymbol{\mu}_f + \mathbf{f}^x)dt), \quad (2.2a)$$

$$d\mathbf{R}_f(t) = (\boldsymbol{\Lambda}^y \mathbf{R}_f + \mathbf{R}_f(\boldsymbol{\Lambda}^y)^T + (\boldsymbol{\Sigma}^y \circ \boldsymbol{\Sigma}^y) - \mathbf{K}_f(\boldsymbol{\Sigma}^x \circ \boldsymbol{\Sigma}^x)\mathbf{K}_f^T)dt, \quad (2.2b)$$

with

$$\mathbf{K}_f(t, \mathbf{x}) := ((\boldsymbol{\Sigma}^y \circ \boldsymbol{\Sigma}^x) + \mathbf{R}_f(\boldsymbol{\Lambda}^x)^T)(\boldsymbol{\Sigma}^x \circ \boldsymbol{\Sigma}^x)^{-1}, \quad (2.3)$$

being the filter Kalman gain operator of the CGNS and $d\mathbf{x} - (\boldsymbol{\Lambda}^x \boldsymbol{\mu}_f + \mathbf{f}^x)dt$ being its filter innovation process.

Theorem B.2 (Optimal nonlinear smoother state estimation backward equations for CGNSs [19]). *Let $\mathbf{x}(t)$ and $\mathbf{y}(t)$ satisfy (2.1a)–(2.1b). Then, under suitable regularity conditions, the posterior distribution of $\mathbf{y}(t)$ given a realization of the trajectory \mathbf{x} up to the end point T (namely, the optimal smoother solution) is Gaussian,*

$$\mathbb{P}(\mathbf{y}(t) | \mathbf{x}(s \leq T)) \stackrel{(d)}{\approx} \mathcal{N}_l(\boldsymbol{\mu}_s(t), \mathbf{R}_s(t)),$$

where

$$\boldsymbol{\mu}_s(t) := \mathbb{E}[\mathbf{y}(t) | \mathbf{x}(s \leq T)] \quad \text{and} \quad \mathbf{R}_s(t) := \mathbb{E}[(\mathbf{y}(t) - \boldsymbol{\mu}_s(t))(\mathbf{y}(t) - \boldsymbol{\mu}_s(t))^T | \mathbf{x}(s \leq T)],$$

are the unique continuous solutions to the system of optimal nonlinear smoother backward equations for $T \geq t \geq 0$ (t running backward):

$$\overleftarrow{d}\boldsymbol{\mu}_s(t) = -(\boldsymbol{\Lambda}^y \boldsymbol{\mu}_s + \mathbf{f}^y - \mathbf{B}\mathbf{R}_f^{-1}(\boldsymbol{\mu}_f - \boldsymbol{\mu}_s))dt + \mathbf{K}_s(\overleftarrow{d}\mathbf{x} + (\boldsymbol{\Lambda}^x \boldsymbol{\mu}_s + \mathbf{f}^x)dt), \quad (2.4a)$$

$$\overleftarrow{d}\mathbf{R}_s(t) = -\left((\mathbf{A} + \mathbf{B}\mathbf{R}_f^{-1})\mathbf{R}_s + \mathbf{R}_s(\mathbf{A} + \mathbf{B}\mathbf{R}_f^{-1})^\top - (\boldsymbol{\Sigma}^y \circ \boldsymbol{\Sigma}^y) + \mathbf{K}_s(\boldsymbol{\Sigma}^x \circ \boldsymbol{\Sigma}^x)\mathbf{K}_s^\top\right)dt, \quad (2.4b)$$

with

$$\mathbf{K}_s(t, \mathbf{x}) := (\boldsymbol{\Sigma}^y \circ \boldsymbol{\Sigma}^x)(\boldsymbol{\Sigma}^x \circ \boldsymbol{\Sigma}^x)^{-1}, \quad (2.5)$$

being the smoother Kalman gain operator of the CGNS and $\overleftarrow{d}\mathbf{x} + (\boldsymbol{\Lambda}^x \boldsymbol{\mu}_s + \mathbf{f}^x)dt$ being its smoother innovation process, where the auxiliary matrices \mathbf{A} and \mathbf{B} are defined by:

$$\mathbf{A}(t, \mathbf{x}) := \boldsymbol{\Lambda}^y(t, \mathbf{x}) - (\boldsymbol{\Sigma}^y \circ \boldsymbol{\Sigma}^x)(t, \mathbf{x})(\boldsymbol{\Sigma}^x \circ \boldsymbol{\Sigma}^x)^{-1}(t, \mathbf{x})\boldsymbol{\Lambda}^x(t, \mathbf{x}) \in \mathbb{R}^{l \times l},$$

$$\mathbf{B}(t, \mathbf{x}) := (\boldsymbol{\Sigma}^y \circ \boldsymbol{\Sigma}^y)(t, \mathbf{x}) - (\boldsymbol{\Sigma}^y \circ \boldsymbol{\Sigma}^x)(t, \mathbf{x})(\boldsymbol{\Sigma}^x \circ \boldsymbol{\Sigma}^x)^{-1}(t, \mathbf{x})(\boldsymbol{\Sigma}^x \circ \boldsymbol{\Sigma}^y)(t, \mathbf{x}) \in \mathbb{R}^{l \times l}.$$

The backward-arrow notation in denotes a backward Itô integral and is to be understood as:

$$\overleftarrow{d}\mathbf{u}(t) := \lim_{\Delta t \rightarrow 0^+} (\mathbf{u}(t) - \mathbf{u}(t + \Delta t)),$$

i.e., \overleftarrow{d} corresponds to the negative of the usual differential up to its principal (linear) part. Since (2.4) are solved backward, $(\boldsymbol{\mu}_s(T), \mathbf{R}_s(T)) = (\boldsymbol{\mu}_f(T), \mathbf{R}_f(T))$.

B.2 Online Smoother for CGNSs

The theoretical framework in Section A.5 requires computation of $\delta(T'; t)$ in (1.16) for all $t \in [0, T]$ and $T' \in [t, T]$ to evaluate either the subjective or objective CIR of an (conditional) assimilative causal link. For CGNSs, this calculation is now feasible thanks to recent advances in online smoothing algorithms [2], which allow real-time computation of smoother distributions as \mathbf{x} observations arrive sequentially.

Let $\{t_j\}_{j \in \llbracket N \rrbracket}$ be a uniform partition of $[0, T]$ with mesh size $0 < \Delta t \ll 1$ and $t_j = j\Delta t$, for $j \in \llbracket N \rrbracket := \{0, 1, \dots, N\}$, where $N = T/\Delta t$. The assumption of uniform Δt is without loss of generality [2]. In what follows we use a superscript notation \cdot^j to denote the discrete approximation to the continuous form of the respective function when evaluated on t_j , e.g., $\boldsymbol{\Lambda}^{\mathbf{x},j} := \boldsymbol{\Lambda}^{\mathbf{x}}(t_j, \mathbf{x}(t_j))$ and $\mathbf{x}^j := \mathbf{x}(t_j)$. Similar to the continuous-time setup, $(\cdot | \mathbf{x}(s \leq n))$ denotes that we are conditioning on the σ -algebra generated by $\{\mathbf{x}^0, \dots, \mathbf{x}^n\}$. Define the following auxiliary matrices for $j \in \llbracket N \rrbracket$:

$$\mathbf{E}^j := \mathbf{I}_{l \times l} + \left[(\boldsymbol{\Sigma}^y \circ \boldsymbol{\Sigma}^x)^j \left((\boldsymbol{\Sigma}^x \circ \boldsymbol{\Sigma}^x)^j \right)^{-1} \mathbf{G}^{\mathbf{x},j} - \mathbf{G}^{\mathbf{y},j} \right] \Delta t \in \mathbb{R}^{l \times l},$$

$$\mathbf{F}^j := -\mathbf{R}_f^j \left[(\mathbf{K}^j)^\top + \left((\mathbf{G}^{\mathbf{x},j})^\top \mathbf{K}^j \mathbf{R}_f^j (\mathbf{K}^j)^\top - (\mathbf{R}_f^j)^{-1} (\mathbf{H}^j)^\top \mathbf{R}_f^j (\mathbf{K}^j)^\top + (\boldsymbol{\Lambda}^{\mathbf{y},j})^\top (\mathbf{K}^j)^\top \right) \Delta t - (\boldsymbol{\Lambda}^{\mathbf{x},j})^\top \left(\left((\boldsymbol{\Sigma}^x \circ \boldsymbol{\Sigma}^x)^j \right)^{-1} + \mathbf{K}^j \mathbf{R}_f^j (\mathbf{K}^j)^\top \Delta t \right) \right] \in \mathbb{R}^{l \times k},$$

where

$$\mathbf{G}^{\mathbf{x},j} := \boldsymbol{\Lambda}^{\mathbf{x},j} + (\boldsymbol{\Sigma}^x \circ \boldsymbol{\Sigma}^y)^j (\mathbf{R}_f^j)^{-1} \in \mathbb{R}^{k \times l},$$

$$\mathbf{G}^{\mathbf{y},j} := \boldsymbol{\Lambda}^{\mathbf{y},j} + (\boldsymbol{\Sigma}^y \circ \boldsymbol{\Sigma}^y)^j (\mathbf{R}_f^j)^{-1} \in \mathbb{R}^{l \times l},$$

$$\mathbf{H}^j := (\mathbf{R}_f^j)^{-1} \left(\boldsymbol{\Lambda}^{\mathbf{y},j} \mathbf{R}_f^j + \mathbf{R}_f^j (\boldsymbol{\Lambda}^{\mathbf{y},j})^\top + (\boldsymbol{\Sigma}^y \circ \boldsymbol{\Sigma}^y)^j \right) \in \mathbb{R}^{l \times l},$$

$$\mathbf{K}^j := \left((\boldsymbol{\Sigma}^x \circ \boldsymbol{\Sigma}^x)^j \right)^{-1} \mathbf{G}^{\mathbf{x},j} \in \mathbb{R}^{k \times l}.$$

Theorem B.3 (Optimal online smoother for CGNSs [2]). *Let $\mathbf{x}(t)$ and $\mathbf{y}(t)$ satisfy (2.1a)–(2.1b). Then, under suitable regularity conditions, the discrete-time smoother distribution up to the n -th observation \mathbf{x}^n at t_j is Gaussian,*

$$\mathbb{P}(\mathbf{y}^j | \mathbf{x}(s \leq n)) \stackrel{(d)}{\sim} \mathcal{N}_l(\boldsymbol{\mu}_s^{j,n}, \mathbf{R}_s^{j,n}),$$

where

$$\boldsymbol{\mu}_s^{j,n} := \mathbb{E}[\mathbf{y}^j | \mathbf{x}(s \leq n)], \quad \mathbf{R}_s^{j,n} := \mathbb{E}[(\mathbf{y}^j - \boldsymbol{\mu}_s^{j,n})(\mathbf{y}^j - \boldsymbol{\mu}_s^{j,n})^\top | \mathbf{x}(s \leq n)],$$

for $n \in \llbracket N \rrbracket$ and $j = n$ are given by $\boldsymbol{\mu}_s^{n,n} = \boldsymbol{\mu}_f^n$ and $\mathbf{R}_s^{n,n} = \mathbf{R}_f^n$, since the smoother and filter Gaussian statistics coincide at the current end point t_n . Then, for $n \in \{1, \dots, N\}$ and $j = n - 1$ they are instead given by the following equations:

$$\begin{aligned} \boldsymbol{\mu}_s^{n-1,n} &= \mathbf{E}^{n-1} \boldsymbol{\mu}_f^n + \mathbf{b}^{n-1}, \\ \mathbf{R}_s^{n-1,n} &= \mathbf{E}^{n-1} \mathbf{R}_f^n (\mathbf{E}^{n-1})^\top + \mathbf{P}_n^{n-1}, \end{aligned}$$

where the \mathbf{b}^{n-1} and \mathbf{P}_n^{n-1} auxiliary residual terms are defined by

$$\begin{aligned} \mathbf{b}^{n-1} &:= \boldsymbol{\mu}_f^{n-1} - \mathbf{E}^{n-1} \left((\mathbf{I}_{l \times l} + \boldsymbol{\Lambda}^{\mathbf{y},n-1} \Delta t) \boldsymbol{\mu}_f^{n-1} + \mathbf{f}^{\mathbf{y},n-1} \Delta t \right) \\ &\quad + \mathbf{F}^{n-1} \left(\mathbf{x}^n - \mathbf{x}^{n-1} - (\boldsymbol{\Lambda}^{\mathbf{x},n-1} \boldsymbol{\mu}_f^{n-1} + \mathbf{f}^{\mathbf{x},n-1}) \Delta t \right), \\ \mathbf{P}_n^{n-1} &:= \mathbf{R}_f^{n-1} - \mathbf{E}^{n-1} (\mathbf{I}_{l \times l} + \boldsymbol{\Lambda}^{\mathbf{y},n-1} \Delta t) \mathbf{R}_f^{n-1} - \mathbf{F}^{n-1} \boldsymbol{\Lambda}^{\mathbf{x},n-1} \mathbf{R}_f^{n-1} \Delta t, \end{aligned}$$

while finally for $n \in \{2, \dots, N\}$ and $j \in \llbracket n-2 \rrbracket$ they are the unique solutions to the following system of recursive backward difference equations:

$$\boldsymbol{\mu}_s^{j,n} = \boldsymbol{\mu}_s^{j,n-1} + \mathbf{D}^{j,n-2} \left(\boldsymbol{\mu}_s^{n-1,n} - \boldsymbol{\mu}_f^{n-1} \right), \quad (2.6a)$$

$$\mathbf{R}_s^{j,n} = \mathbf{R}_s^{j,n-1} + \mathbf{D}^{j,n-2} \left(\mathbf{R}_s^{n-1,n} - \mathbf{R}_f^{n-1} \right) (\mathbf{D}^{j,n-2})^\top, \quad (2.6b)$$

with the update matrices $\mathbf{D}^{j,n-2}$ being defined as

$$\mathbf{D}^{n-1,n-2} := \mathbf{I}_{l \times l} \quad \& \quad \mathbf{D}^{j,n-2} := \prod_{i=j}^{\curvearrowright n-2} \mathbf{E}^i := \mathbf{E}^j \mathbf{E}^{j+1} \dots \mathbf{E}^{n-2}. \quad (2.7)$$

Theorem B.3 yields $O(\Delta t)$ -accurate discrete-time Gaussian smoother statistics for each new observation \mathbf{x}^n at $t_n = n\Delta t$ ($n \in \llbracket N \rrbracket$) by solving (2.6a)–(2.6b) backward over $j \in \llbracket n \rrbracket$, where the forward operator $\mathbf{D}^{j,n-2}$ represents the discrete-time smoother Kalman gain at t_j for the n -th observation, while $\boldsymbol{\mu}_s^{n-1,n} - \boldsymbol{\mu}_f^{n-1}$ and $\mathbf{R}_s^{n-1,n} - \mathbf{R}_f^{n-1}$ respectively denote the discrete-time innovation mean and covariance corresponding to \mathbf{x}^n .

B.3 Calculation of the Subjective and Objective CIRs for CGNSs

Using the online smoother for CGNSs, for each $j \in \llbracket N \rrbracket$ we can compute both the subjective and objective CIRs over $[t_j, T]$ for the potential assimilative causal link $\mathbf{y}^j \rightarrow \mathbf{x}$ (with analogous results for the CCIRs). Let $p_n(\mathbf{y}^j | \mathbf{x})$, for $j \in \llbracket N \rrbracket$ and $n \in \{j, \dots, N\}$ denote the $\mathcal{N}_l(\boldsymbol{\mu}_s^{j,n}, \mathbf{R}_s^{j,n})$ PDF from Theorem B.3. At each $t_j = j\Delta t$, we quantify the information gain in the complete smoother distribution $p_N(\mathbf{y}^j | \mathbf{x})$ beyond its lagged counterpart $p_n(\mathbf{y}^j | \mathbf{x})$ using the signal-dispersion decomposition from (1.6) as:

$$\begin{aligned} \mathcal{P}_n^j &:= \mathcal{P}(p_N(\mathbf{y}^j | \mathbf{x}), p_n(\mathbf{y}^j | \mathbf{x})) = \frac{1}{2} \left(\boldsymbol{\mu}_s^{j,N} - \boldsymbol{\mu}_s^{j,n} \right)^\top (\mathbf{R}_s^{j,n})^{-1} \left(\boldsymbol{\mu}_s^{j,N} - \boldsymbol{\mu}_s^{j,n} \right) \\ &\quad + \frac{1}{2} \left(\text{tr} \left(\mathbf{R}_s^{j,N} (\mathbf{R}_s^{j,n})^{-1} \right) - l - \ln \left(\det \left(\mathbf{R}_s^{j,N} (\mathbf{R}_s^{j,n})^{-1} \right) \right) \right). \end{aligned} \quad (2.8)$$

Per Section A.5 and (1.16), we identify $\delta(t_n; t_j) = \mathcal{P}_n^j$, for $j \in \llbracket N \rrbracket$ and $n \in \{j, \dots, N\}$. This yields:

- The *subjective CIR length* for a threshold $\varepsilon \geq 0$:

$$\tilde{\tau}_{\mathbf{y}(t_j) \rightarrow \mathbf{x}}(\varepsilon) = \max_{n \in \{j, \dots, N\}} \left\{ \mathcal{P}_n^j > \varepsilon \right\} \Delta t - t_j \in [0, T - t_j]. \quad (2.9)$$

- The *objective CIR length* via integration of (2.9) over $\varepsilon \in [0, \max_n \{\mathcal{P}_n^j\}]$.
- Its efficient approximation:

$$\tau_{\mathbf{y}(t_j) \rightarrow \mathbf{x}}^{\text{approx}} = \frac{\Delta t}{\max_n \{\mathcal{P}_n^j\}} \sum_{n=j}^N \mathcal{P}_n^j \in [0, T - t_j]. \quad (2.10)$$

We maintain the conventions from Section A.5: $\tilde{\tau}_{\mathbf{y}(t_j) \rightarrow \mathbf{x}}(\varepsilon) = 0$ when no maximum exists, and $\tau_{\mathbf{y}(t_j) \rightarrow \mathbf{x}} = \tau_{\mathbf{y}(t_j) \rightarrow \mathbf{x}}^{\text{approx}} = 0 = \tilde{\tau}_{\mathbf{y}(t_j) \rightarrow \mathbf{x}}(\varepsilon)$ when $\max_n \{\mathcal{P}_n^j\} = 0$. For strongly intermittent systems and the objective CIR, we employ the computationally efficient scheme in (2.10) rather than the full integral definition.

In Algorithm 3 we provide a brief outline of how to calculate the subjective and objective CIR lengths of $\mathbf{y}^j \rightarrow \mathbf{x}$ over $[t_j, T]$ for $j \in \llbracket N \rrbracket$ in pseudocode, specifically for CGNSs. An analogous algorithm extends to CCIRs for CGNSs, as well as to the general complex system in (1.1) by appropriately computing $\delta(t_n; t_j) = \mathcal{P}_n^j$ for each $j \in \llbracket N \rrbracket$ and $n \in \{j, \dots, N\}$.

Algorithm 3: CIRs of $\mathbf{y}^j \rightarrow \mathbf{x}$ over $[t_j, T]$ for $j \in \llbracket N \rrbracket$ in the case of a CGNS

Data: $N \in \mathbb{N}$, $0 < \Delta t \ll 1$, $\{t_j = j\Delta t\}_{j \in \llbracket N \rrbracket}$, Observations of \mathbf{x} : $\{\mathbf{x}^0, \dots, \mathbf{x}^N\}$, $\boldsymbol{\mu}_f^0, \mathbf{R}_f^0$, $\varepsilon \geq 0$

Result: $\tilde{\tau}_{\mathbf{y}(t_j) \rightarrow \mathbf{x}}(\varepsilon)$ for arbitrary ε , $\tau_{\mathbf{y}(t_j) \rightarrow \mathbf{x}}$, and $\tau_{\mathbf{y}(t_j) \rightarrow \mathbf{x}}^{\text{approx}}$, all for $j \in \llbracket N \rrbracket$

```

1 for  $j \in \llbracket N \rrbracket$  do
2   for  $n \in \{j, \dots, N\}$  do
3     | Calculate  $p_n(\mathbf{y}^j | \mathbf{x})$ , the Gaussian PDF corresponding to  $\mathcal{N}_l(\boldsymbol{\mu}_s^{j,n}, \mathbf{R}_s^{j,n})$ , per Theorem B.3;
4   end
5   Calculate  $\delta(t_n; t_j) = \mathcal{P}_n^j$  using (2.8) for each  $n \in \{j, \dots, N\}$ ;
6   if  $\varepsilon < \max_n \{\mathcal{P}_n^j\}$  then
7     |  $\tilde{\tau}_{\mathbf{y}(t_j) \rightarrow \mathbf{x}}(\varepsilon) = \max_{n \in \{j, \dots, N\}} \left\{ \mathcal{P}_n^j > \varepsilon \right\} \Delta t - t_j$ ;
8   else
9     |  $\tilde{\tau}_{\mathbf{y}(t_j) \rightarrow \mathbf{x}}(\varepsilon) = 0$ ;
10  end
11  if  $\max_n \{\mathcal{P}_n^j\} > 0$  then
12    | if  $\tilde{\tau}_{\mathbf{y}(t_j) \rightarrow \mathbf{x}}(\varepsilon)$  is known for many  $\varepsilon \in [0, \max_n \{\mathcal{P}_n^j\}]$  then
13      |  $\tau_{\mathbf{y}(t_j) \rightarrow \mathbf{x}} = \frac{1}{\max_n \{\mathcal{P}_n^j\}} \int_0^{\max_n \{\mathcal{P}_n^j\}} \tilde{\tau}_{\mathbf{y}(t) \rightarrow \mathbf{x}}(\varepsilon) d\varepsilon$ ;
14    end
15     $\tau_{\mathbf{y}(t_j) \rightarrow \mathbf{x}}^{\text{approx}} = \frac{\Delta t}{\max_n \{\mathcal{P}_n^j\}} \sum_{n=j}^N \mathcal{P}_n^j$ ; /* If  $\max_n \{\mathcal{P}_n^j\}$  is essentially negligible, e.g.,
16       $\max_n \{\mathcal{P}_n^j\} < 10^{-4}$ , we can set  $\tau_{\mathbf{y}(t_j) \rightarrow \mathbf{x}}^{\text{approx}} = 0$ , which necessarily coincides with  $\tau_{\mathbf{y}(t_j) \rightarrow \mathbf{x}} \approx 0$ ,
17      as to avoid operationally inflated values due to numerical imprecision
18    else
19      |  $\tau_{\mathbf{y}(t_j) \rightarrow \mathbf{x}} = \tau_{\mathbf{y}(t_j) \rightarrow \mathbf{x}}^{\text{approx}} = 0$ ;
20    end
21  end
22 end

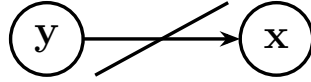
```

SI.C ACI-Based Principles of Nil Causality

Before investigating complex turbulent systems, we first validate the ACI framework's theoretical foundations using the analytically tractable CGNS structure. Crucially, any reliable causal metric must satisfy two requirements: (1) It should be asymmetric in its state components, sometimes referred to as Schreiber's principle [28], and (2) it should correctly identify unidirectional relationships, yielding zero measure in non-causal directions; in other words, it must obey the *principle of nil causality* [18], which is "an event cannot cause another if their dynamics are independent". Both ACI and its conditional variant naturally satisfy (1) for general complex systems. As for the principle of nil causality, for CGNSs this principle takes a rigorous form: when \mathbf{x} 's evolution is independent of \mathbf{y} , the ACI framework guarantees $\mathbf{y}(t) \not\rightarrow \mathbf{x}$ for all $t \in [0, T]$, confirming the absence of spurious causality. This extends to conditional ACI, mutatis mutandis.

C.1 Principle of Nil Assimilative Causality for CGNSs

Theorem C.1 (Principle of Nil Assimilative Causality for CGNSs). *Let $\mathbf{x}(t)$ and $\mathbf{y}(t)$ satisfy (2.1a)–(2.1b). When $\Lambda^{\mathbf{x}} \equiv \mathbf{0}_{k \times l}$ and $(\Sigma^{\mathbf{y}} \circ \Sigma^{\mathbf{x}}) \equiv \mathbf{0}_{l \times k}$ for every t and \mathbf{x} , then the ground-truth causal network is:*



This is validated by the ACI framework per (1.2) and (1.4)–(1.5):

$$\mathbf{y}(t) \not\rightarrow \mathbf{x}, \quad \forall t \in [0, T],$$

since in this case we have

$$p_t^s(\mathbf{y}|\mathbf{x}) = p_t^f(\mathbf{y}|\mathbf{x}), \quad t \in [0, T].$$

Note on Theorem C.1: The condition $\Lambda^{\mathbf{x}} \equiv \mathbf{0}_{k \times l}$ prohibits \mathbf{y} from entering the mean dynamics of \mathbf{x} , while $(\Sigma^{\mathbf{y}} \circ \Sigma^{\mathbf{x}}) \equiv \mathbf{0}_{l \times k}$ nullifies the cross-interactions between their noise feedbacks. The combination of these two assumptions removes the possibility of \mathbf{y} contributing to the evolution of \mathbf{x} in the dynamics, both through its drift coefficient, as well as via the full diffusion coefficient of the system in (2.1). As a result: $\mathbf{y} \not\rightarrow \mathbf{x}$.

Proof of Theorem C.1. Since $\Lambda^{\mathbf{x}} \equiv \mathbf{0}_{k \times l}$ and $(\Sigma^{\mathbf{y}} \circ \Sigma^{\mathbf{x}}) \equiv \mathbf{0}_{l \times k}$, by (2.3) we have that the filter Kalman gain operator of the CGNS vanishes. As a result, the filter equations for the mean and covariance matrix reduce to their model-forecast part:

$$\begin{aligned} d\boldsymbol{\mu}_f(t) &= (\Lambda^{\mathbf{y}} \boldsymbol{\mu}_f + \mathbf{f}^{\mathbf{y}})dt, \\ d\mathbf{R}_f(t) &= \left(\Lambda^{\mathbf{y}} \mathbf{R}_f + \mathbf{R}_f (\Lambda^{\mathbf{y}})^T + (\Sigma^{\mathbf{y}} \circ \Sigma^{\mathbf{y}}) \right) dt. \end{aligned}$$

The equations for the filter statistics become decorrelated under this regime, meaning they can be solved independently. Similarly to its filter counterpart, the smoother Kalman gain operator of the CGNS also vanishes, meaning the smoother equations likewise become:

$$\begin{aligned} \overleftarrow{d}\boldsymbol{\mu}_s(t) &= -(\Lambda^{\mathbf{y}} \boldsymbol{\mu}_s + \mathbf{f}^{\mathbf{y}} - (\Sigma^{\mathbf{y}} \circ \Sigma^{\mathbf{y}}) \mathbf{R}_f^{-1} (\boldsymbol{\mu}_f - \boldsymbol{\mu}_s))dt, \\ \overleftarrow{d}\mathbf{R}_s(t) &= -\left((\Lambda^{\mathbf{y}} + (\Sigma^{\mathbf{y}} \circ \Sigma^{\mathbf{y}}) \mathbf{R}_f^{-1}) \mathbf{R}_s + \mathbf{R}_s (\Lambda^{\mathbf{y}} + (\Sigma^{\mathbf{y}} \circ \Sigma^{\mathbf{y}}) \mathbf{R}_f^{-1})^T - (\Sigma^{\mathbf{y}} \circ \Sigma^{\mathbf{y}}) \right) dt. \end{aligned}$$

Taking the difference between the filter and smoother equations we have

$$\overleftarrow{d}(\boldsymbol{\mu}_s - \boldsymbol{\mu}_f)(t) = \overleftarrow{d}\boldsymbol{\mu}_s(t) + d\boldsymbol{\mu}_f(t) = -(\Lambda^{\mathbf{y}} + (\Sigma^{\mathbf{y}} \circ \Sigma^{\mathbf{y}}) \mathbf{R}_f^{-1}) (\boldsymbol{\mu}_s - \boldsymbol{\mu}_f) dt, \quad T \geq t \geq 0, \quad (3.1)$$

and so by $\boldsymbol{\mu}_s(T) = \boldsymbol{\mu}_f(T)$, the linearity of (3.1), and its uniqueness of solution, we retrieve

$$\boldsymbol{\mu}_s(t) = \boldsymbol{\mu}_f(t), \quad t \in [0, T].$$

As an immediate consequence, we have

$$\begin{aligned} \mathbf{R}_s(t) &= \mathbb{E} \left[(\mathbf{y}(t) - \boldsymbol{\mu}_s(t))(\mathbf{y}(t) - \boldsymbol{\mu}_s(t))^{\top} \mid \mathbf{x}(s \leq T) \right] \\ &= \mathbb{E} \left[(\mathbf{y}(t) - \boldsymbol{\mu}_f(t))(\mathbf{y}(t) - \boldsymbol{\mu}_f(t))^{\top} \mid \mathbf{x}(s \leq T) \right] = \mathbf{R}_f(t), \quad t \in [0, T], \end{aligned}$$

where in the last equality we have used the stability property of conditional expectations, $\mathcal{F}_t^{\mathbf{x}} \subseteq \mathcal{F}_T^{\mathbf{x}}$, and the $\mathcal{F}_t^{\mathbf{x}}$ -measurability of $\mathbf{R}_f(t)$, with $\mathcal{F}_t^{\mathbf{x}}$ denoting the σ -algebra generated by $\{\mathbf{x}(s)\}_{s \leq t}$ for $t \in [0, T]$ [19]. Combining these, we end up with:

$$p_t^s(\mathbf{y} \mid \mathbf{x}) = p_t^f(\mathbf{y} \mid \mathbf{x}), \quad t \in [0, T],$$

which by (1.4) yields $\mathbf{y}(t) \not\rightarrow \mathbf{x}$ for each $t \in [0, T]$. ■

C.2 Principle of Nil Conditional Assimilative Causality for CGNSs

The following theorem extends Theorem C.1 to establish the principle of nil *conditional* assimilative causality for CGNSs. To formulate this result, we first introduce some necessary notation. Following Section A.4, we consider the state variables $(\mathbf{x}_A, \mathbf{x}_B, \mathbf{y})$ and reformulate the CGNS in (1.1) as:

$$d\mathbf{x}_A(t) = \left(\boldsymbol{\Lambda}^{\mathbf{x}_A}(t, \mathbf{x})\mathbf{y}(t) + \mathbf{f}^{\mathbf{x}_A}(t, \mathbf{x}) \right) dt + \boldsymbol{\Sigma}_1^{\mathbf{x}_A}(t, \mathbf{x})d\mathbf{W}_1(t) + \boldsymbol{\Sigma}_2^{\mathbf{x}_A}(t, \mathbf{x})d\mathbf{W}_2(t), \quad (3.2a)$$

$$d\mathbf{x}_B(t) = \left(\boldsymbol{\Lambda}^{\mathbf{x}_B}(t, \mathbf{x})\mathbf{y}(t) + \mathbf{f}^{\mathbf{x}_B}(t, \mathbf{x}) \right) dt + \boldsymbol{\Sigma}_1^{\mathbf{x}_B}(t, \mathbf{x})d\mathbf{W}_1(t) + \boldsymbol{\Sigma}_2^{\mathbf{x}_B}(t, \mathbf{x})d\mathbf{W}_2(t), \quad (3.2b)$$

$$d\mathbf{y}(t) = \left(\boldsymbol{\Lambda}^{\mathbf{y}}(t, \mathbf{x})\mathbf{y}(t) + \mathbf{f}^{\mathbf{y}}(t, \mathbf{x}) \right) dt + \boldsymbol{\Sigma}_1^{\mathbf{y}}(t, \mathbf{x})d\mathbf{W}_1(t) + \boldsymbol{\Sigma}_2^{\mathbf{y}}(t, \mathbf{x})d\mathbf{W}_2(t), \quad (3.2c)$$

where by using block-matrix notation we have:

$$\begin{aligned} \boldsymbol{\Lambda}^{\mathbf{x}} &= \begin{pmatrix} \boldsymbol{\Lambda}^{\mathbf{x}_A} \\ \boldsymbol{\Lambda}^{\mathbf{x}_B} \end{pmatrix}, \quad \mathbf{f}^{\mathbf{x}} = \begin{pmatrix} \mathbf{f}^{\mathbf{x}_A} \\ \mathbf{f}^{\mathbf{x}_B} \end{pmatrix}, \quad \boldsymbol{\Sigma}_m^{\mathbf{x}} = \begin{pmatrix} \boldsymbol{\Sigma}_m^{\mathbf{x}_A} \\ \boldsymbol{\Sigma}_m^{\mathbf{x}_B} \end{pmatrix}, \quad m = 1, 2, \\ \boldsymbol{\Lambda}^{\mathbf{x}\square} &\in \mathbb{R}^{k_{\square} \times l}, \quad \mathbf{f}^{\mathbf{x}\square} \in \mathbb{R}^{k_{\square}}, \quad \boldsymbol{\Sigma}_m^{\mathbf{x}\square} \in \mathbb{R}^{k_{\square} \times d_m}, \quad m = 1, 2, \quad \square \in \{A, B\}. \end{aligned}$$

Under this formulation, $(\boldsymbol{\Sigma}^{\mathbf{x}} \circ \boldsymbol{\Sigma}^{\mathbf{x}})$ can be depicted as a 2×2 block matrix:

$$(\boldsymbol{\Sigma}^{\mathbf{x}} \circ \boldsymbol{\Sigma}^{\mathbf{x}}) = \boldsymbol{\Sigma}_1^{\mathbf{x}}(\boldsymbol{\Sigma}_1^{\mathbf{x}})^{\top} + \boldsymbol{\Sigma}_2^{\mathbf{x}}(\boldsymbol{\Sigma}_2^{\mathbf{x}})^{\top} = \begin{pmatrix} (\boldsymbol{\Sigma}^{\mathbf{x}_A} \circ \boldsymbol{\Sigma}^{\mathbf{x}_A}) & (\boldsymbol{\Sigma}^{\mathbf{x}_A} \circ \boldsymbol{\Sigma}^{\mathbf{x}_B}) \\ (\boldsymbol{\Sigma}^{\mathbf{x}_B} \circ \boldsymbol{\Sigma}^{\mathbf{x}_A}) & (\boldsymbol{\Sigma}^{\mathbf{x}_B} \circ \boldsymbol{\Sigma}^{\mathbf{x}_B}) \end{pmatrix}.$$

We also define the Schur complement of the $(\boldsymbol{\Sigma}^{\mathbf{x}_A} \circ \boldsymbol{\Sigma}^{\mathbf{x}_A})$ and $(\boldsymbol{\Sigma}^{\mathbf{x}_B} \circ \boldsymbol{\Sigma}^{\mathbf{x}_B})$ blocks with respect to $(\boldsymbol{\Sigma}^{\mathbf{x}} \circ \boldsymbol{\Sigma}^{\mathbf{x}})$ [9]:

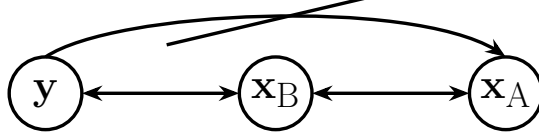
$$\begin{aligned} (\boldsymbol{\Sigma}^{\mathbf{x}} \circ \boldsymbol{\Sigma}^{\mathbf{x}}) / (\boldsymbol{\Sigma}^{\mathbf{x}_A} \circ \boldsymbol{\Sigma}^{\mathbf{x}_A}) &:= (\boldsymbol{\Sigma}^{\mathbf{x}_B} \circ \boldsymbol{\Sigma}^{\mathbf{x}_B}) - (\boldsymbol{\Sigma}^{\mathbf{x}_B} \circ \boldsymbol{\Sigma}^{\mathbf{x}_A})(\boldsymbol{\Sigma}^{\mathbf{x}_A} \circ \boldsymbol{\Sigma}^{\mathbf{x}_A})^{-1}(\boldsymbol{\Sigma}^{\mathbf{x}_A} \circ \boldsymbol{\Sigma}^{\mathbf{x}_B}), \\ (\boldsymbol{\Sigma}^{\mathbf{x}} \circ \boldsymbol{\Sigma}^{\mathbf{x}}) / (\boldsymbol{\Sigma}^{\mathbf{x}_B} \circ \boldsymbol{\Sigma}^{\mathbf{x}_B}) &:= (\boldsymbol{\Sigma}^{\mathbf{x}_A} \circ \boldsymbol{\Sigma}^{\mathbf{x}_A}) - (\boldsymbol{\Sigma}^{\mathbf{x}_A} \circ \boldsymbol{\Sigma}^{\mathbf{x}_B})(\boldsymbol{\Sigma}^{\mathbf{x}_B} \circ \boldsymbol{\Sigma}^{\mathbf{x}_B})^{-1}(\boldsymbol{\Sigma}^{\mathbf{x}_B} \circ \boldsymbol{\Sigma}^{\mathbf{x}_A}), \end{aligned} \quad (3.3)$$

under the tacit assumption that $(\boldsymbol{\Sigma}^{\mathbf{x}_A} \circ \boldsymbol{\Sigma}^{\mathbf{x}_A})$ and $(\boldsymbol{\Sigma}^{\mathbf{x}_B} \circ \boldsymbol{\Sigma}^{\mathbf{x}_B})$ are invertible; $(\boldsymbol{\Sigma}^{\mathbf{x}} \circ \boldsymbol{\Sigma}^{\mathbf{x}})$ is positive definite if and only if either one of $(\boldsymbol{\Sigma}^{\mathbf{x}_A} \circ \boldsymbol{\Sigma}^{\mathbf{x}_A})$ or $(\boldsymbol{\Sigma}^{\mathbf{x}_B} \circ \boldsymbol{\Sigma}^{\mathbf{x}_B})$ and its associated Schur complement are positive definite matrices [9]. In the case where both $(\boldsymbol{\Sigma}^{\mathbf{x}_A} \circ \boldsymbol{\Sigma}^{\mathbf{x}_A})$ and $(\boldsymbol{\Sigma}^{\mathbf{x}_B} \circ \boldsymbol{\Sigma}^{\mathbf{x}_B})$ are positive definite, then $(\boldsymbol{\Sigma}^{\mathbf{x}} \circ \boldsymbol{\Sigma}^{\mathbf{x}})^{-1}$ enjoys the following explicit representation:

$$\begin{aligned} (\boldsymbol{\Sigma}^{\mathbf{x}} \circ \boldsymbol{\Sigma}^{\mathbf{x}})^{-1} &= \begin{pmatrix} \left((\boldsymbol{\Sigma}^{\mathbf{x}} \circ \boldsymbol{\Sigma}^{\mathbf{x}}) / (\boldsymbol{\Sigma}^{\mathbf{x}_B} \circ \boldsymbol{\Sigma}^{\mathbf{x}_B}) \right)^{-1} & \mathbf{0}_{k_A \times k_B} \\ \mathbf{0}_{k_B \times k_A} & \left((\boldsymbol{\Sigma}^{\mathbf{x}} \circ \boldsymbol{\Sigma}^{\mathbf{x}}) / (\boldsymbol{\Sigma}^{\mathbf{x}_A} \circ \boldsymbol{\Sigma}^{\mathbf{x}_A}) \right)^{-1} \end{pmatrix} \\ &\times \begin{pmatrix} \mathbf{I}_{k_A \times k_A} & -(\boldsymbol{\Sigma}^{\mathbf{x}_A} \circ \boldsymbol{\Sigma}^{\mathbf{x}_B})(\boldsymbol{\Sigma}^{\mathbf{x}_B} \circ \boldsymbol{\Sigma}^{\mathbf{x}_B})^{-1} \\ -(\boldsymbol{\Sigma}^{\mathbf{x}_B} \circ \boldsymbol{\Sigma}^{\mathbf{x}_A})(\boldsymbol{\Sigma}^{\mathbf{x}_A} \circ \boldsymbol{\Sigma}^{\mathbf{x}_A})^{-1} & \mathbf{I}_{k_B \times k_B} \end{pmatrix}. \end{aligned} \quad (3.4)$$

With these preliminaries, we now establish the principle of nil conditional assimilative causality for CGNSs: when (i) \mathbf{x}_A 's evolution is independent of \mathbf{y} , and (ii) the uncertainty levels of \mathbf{x}_A and \mathbf{x}_B are non-interacting, the generalized ACI framework correctly identifies the absence of conditional causation. Formally, $(\mathbf{y}(t) \not\rightarrow \mathbf{x}_A) | \mathbf{x}_B$, for all $t \in [0, T]$.

Theorem C.2 (Principle of Nil Conditional Assimilative Causality for CGNSs). *Let $\mathbf{x}(t)$ and $\mathbf{y}(t)$ satisfy (2.1a)–(2.1b). When $\Lambda^{\mathbf{x}_A} \equiv \mathbf{0}_{k_A \times l}$, $(\Sigma^{\mathbf{y}} \circ \Sigma^{\mathbf{x}_A}) \equiv \mathbf{0}_{l \times k_B}$, and $(\Sigma^{\mathbf{x}_A} \circ \Sigma^{\mathbf{x}_B}) \equiv \mathbf{0}_{k_A \times k_B}$ for every t and \mathbf{x} , then the ground-truth causal network is:*



This is validated by the ACI framework per (1.13)–(1.15):

$$(\mathbf{y}(t) \not\rightarrow \mathbf{x}_A) | \mathbf{x}_B, \quad \forall t \in [0, T],$$

since in this case we have

$$p_t^{s|\mathbf{x}_B}(\mathbf{y}|\mathbf{x}_A) = p_t^{f|\mathbf{x}_B}(\mathbf{y}|\mathbf{x}_A), \quad t \in [0, T].$$

Note on Theorem C.2: The assumption $\Lambda^{\mathbf{x}_A} \equiv \mathbf{0}_{k_A \times l}$ eliminates direct influence of \mathbf{y} on \mathbf{x}_A 's mean dynamics, while $(\Sigma^{\mathbf{y}} \circ \Sigma^{\mathbf{x}_A}) \equiv \mathbf{0}_{l \times k_B}$ removes their noise feedback coupling. However, these conditions alone are insufficient to prevent indirect \mathbf{y} - \mathbf{x}_A interactions through \mathbf{x}_B via observable noise cross-correlations. We therefore additionally impose $(\Sigma^{\mathbf{x}_A} \circ \Sigma^{\mathbf{x}_B}) \equiv \mathbf{0}_{k_A \times k_B}$, rendering $(\Sigma^{\mathbf{x}} \circ \Sigma^{\mathbf{x}})$ block-diagonal. Collectively, these ensure: $(\mathbf{y} \not\rightarrow \mathbf{x}_A) | \mathbf{x}_B$.

Proof of Theorem C.2. For CGNS, the filter and smoother means evolve according to linear random ODEs, while their covariance matrices satisfy forward Riccati and backward symmetric Sylvester random ODEs respectively [1]. Under the regularity conditions of Theorems B.1 and B.2, these Gaussian statistics exhibit continuous dependence on both the model parameters in (2.1) and their initial/terminal conditions [10, 22]. This continuity allows direct computation of the posterior PDFs in (1.13) through the limit $\text{Var}(\mathbf{x}_B(t)) \rightarrow +\infty$ applied to (2.2) and (2.4). Crucially, Gaussianity is preserved under this limit since a normal distribution depends continuously on its mean and covariance. Specifically, $p_t^{f|\mathbf{x}_B}(\mathbf{y}|\mathbf{x}_A)$ remains Gaussian $\mathcal{N}_l(\boldsymbol{\mu}_{f|\mathbf{x}_B}(t), \mathbf{R}_{f|\mathbf{x}_B}(t))$, where:

$$d\boldsymbol{\mu}_{f|\mathbf{x}_B}(t) = (\Lambda^{\mathbf{y}}\boldsymbol{\mu}_{f|\mathbf{x}_B} + \mathbf{f}^{\mathbf{y}})dt + \mathbf{K}_{f|\mathbf{x}_B}(d\mathbf{x} - (\Lambda^{\mathbf{x}}\boldsymbol{\mu}_{f|\mathbf{x}_B} + \mathbf{f}^{\mathbf{x}})dt), \quad (3.5a)$$

$$d\mathbf{R}_{f|\mathbf{x}_B}(t) = \left(\Lambda^{\mathbf{y}}\mathbf{R}_{f|\mathbf{x}_B} + \mathbf{R}_{f|\mathbf{x}_B}(\Lambda^{\mathbf{y}})^{\mathbf{T}} + (\Sigma^{\mathbf{y}} \circ \Sigma^{\mathbf{y}}) - \mathbf{K}_{f|\mathbf{x}_B}(\Sigma^{\mathbf{x}} \circ \Sigma^{\mathbf{x}})\mathbf{K}_{f|\mathbf{x}_B}^{\mathbf{T}} \right)dt, \quad (3.5b)$$

with

$$\mathbf{K}_{f|\mathbf{x}_B}(t, \mathbf{x}) := \lim_{\text{Var}(\mathbf{x}_B(t)) \rightarrow +\infty} \mathbf{K}_f(t, \mathbf{x}),$$

while $p_t^{s|\mathbf{x}_B}(\mathbf{y}|\mathbf{x}_A)$ is a Gaussian density corresponding to $\mathcal{N}_l(\boldsymbol{\mu}_{s|\mathbf{x}_B}(t), \mathbf{R}_{s|\mathbf{x}_B}(t))$, where

$$\begin{aligned} \overleftarrow{d}\boldsymbol{\mu}_{s|\mathbf{x}_B}(t) &= -\left(\Lambda^{\mathbf{y}}\boldsymbol{\mu}_{s|\mathbf{x}_B} + \mathbf{f}^{\mathbf{y}} - \mathbf{B}_{|\mathbf{x}_B}\mathbf{R}_{f|\mathbf{x}_B}^{-1}(\boldsymbol{\mu}_{f|\mathbf{x}_B} - \boldsymbol{\mu}_{s|\mathbf{x}_B}) \right)dt \\ &\quad + \mathbf{K}_{s|\mathbf{x}_B} \left(\overleftarrow{d}\mathbf{x} + (\Lambda^{\mathbf{x}}\boldsymbol{\mu}_{s|\mathbf{x}_B} + \mathbf{f}^{\mathbf{x}})dt \right), \end{aligned} \quad (3.6a)$$

$$\begin{aligned} \overleftarrow{d}\mathbf{R}_{s|\mathbf{x}_B}(t) &= -\left((\mathbf{A}_{|\mathbf{x}_B} + \mathbf{B}_{|\mathbf{x}_B}\mathbf{R}_{f|\mathbf{x}_B}^{-1})\mathbf{R}_{s|\mathbf{x}_B} + \mathbf{R}_{s|\mathbf{x}_B}(\mathbf{A}_{|\mathbf{x}_B} + \mathbf{B}_{|\mathbf{x}_B}\mathbf{R}_{f|\mathbf{x}_B}^{-1})^{\mathbf{T}} \right. \\ &\quad \left. - (\Sigma^{\mathbf{y}} \circ \Sigma^{\mathbf{y}}) + \mathbf{K}_{s|\mathbf{x}_B}(\Sigma^{\mathbf{x}} \circ \Sigma^{\mathbf{x}})\mathbf{K}_{s|\mathbf{x}_B}^{\mathbf{T}} \right)dt, \end{aligned} \quad (3.6b)$$

with

$$\begin{aligned}\mathbf{K}_{s|\mathbf{x}_B}(t, \mathbf{x}) &:= \lim_{\text{Var}(\mathbf{x}_B(t)) \rightarrow +\infty} \mathbf{K}_s(t, \mathbf{x}), \\ \mathbf{A}_{|\mathbf{x}_B}(t, \mathbf{x}) &:= \lim_{\text{Var}(\mathbf{x}_B(t)) \rightarrow +\infty} \mathbf{A}(t, \mathbf{x}), \\ \mathbf{B}_{|\mathbf{x}_B}(t, \mathbf{x}) &:= \lim_{\text{Var}(\mathbf{x}_B(t)) \rightarrow +\infty} \mathbf{B}(t, \mathbf{x}).\end{aligned}$$

As the measurability of the posterior Gaussian statistics remains unaffected under the formal limit $\text{Var}(\mathbf{x}_B(t)) \rightarrow +\infty$, we just need to prove

$$\boldsymbol{\mu}_{s|\mathbf{x}_B}(t) = \boldsymbol{\mu}_{f|\mathbf{x}_B}(t), \quad t \in [0, T],$$

as this immediately yields $\mathbf{R}_{s|\mathbf{x}_B} \equiv \mathbf{R}_{f|\mathbf{x}_B}$, similarly to the proof of Theorem C.1.

Following a similar procedure to the proof of Theorem C.1, we first determine how the filter and smoother Kalman gain operators reduce subject to the assumptions of this theorem. Under this regime, by using block-matrix algebra and (3.3)–(3.4), we have from (2.3) that

$$\begin{aligned}\mathbf{K}_f &= \left((\boldsymbol{\Sigma}^y \circ \boldsymbol{\Sigma}^x) + \mathbf{R}_f(\boldsymbol{\Lambda}^x)^\top \right) (\boldsymbol{\Sigma}^x \circ \boldsymbol{\Sigma}^x)^{-1} \\ &= \begin{pmatrix} \mathbf{0}_{l \times k_A} & (\boldsymbol{\Sigma}^y \circ \boldsymbol{\Sigma}^{\mathbf{x}_B}) + \mathbf{R}_f(\boldsymbol{\Lambda}^{\mathbf{x}_B})^\top \end{pmatrix} \\ &\quad \times \begin{pmatrix} \left((\boldsymbol{\Sigma}^x \circ \boldsymbol{\Sigma}^x) / (\boldsymbol{\Sigma}^{\mathbf{x}_B} \circ \boldsymbol{\Sigma}^{\mathbf{x}_B}) \right)^{-1} & \mathbf{0}_{k_A \times k_B} \\ \mathbf{0}_{k_B \times k_A} & \left((\boldsymbol{\Sigma}^x \circ \boldsymbol{\Sigma}^x) / (\boldsymbol{\Sigma}^{\mathbf{x}_A} \circ \boldsymbol{\Sigma}^{\mathbf{x}_A}) \right)^{-1} \end{pmatrix} \\ &= \begin{pmatrix} \mathbf{0}_{l \times k_A} & \left((\boldsymbol{\Sigma}^y \circ \boldsymbol{\Sigma}^{\mathbf{x}_B}) + \mathbf{R}_f(\boldsymbol{\Lambda}^{\mathbf{x}_B})^\top \right) \left((\boldsymbol{\Sigma}^x \circ \boldsymbol{\Sigma}^x) / (\boldsymbol{\Sigma}^{\mathbf{x}_A} \circ \boldsymbol{\Sigma}^{\mathbf{x}_A}) \right)^{-1} \end{pmatrix} \\ &= \begin{pmatrix} \mathbf{0}_{l \times k_A} & \left((\boldsymbol{\Sigma}^y \circ \boldsymbol{\Sigma}^{\mathbf{x}_B}) + \mathbf{R}_f(\boldsymbol{\Lambda}^{\mathbf{x}_B})^\top \right) (\boldsymbol{\Sigma}^{\mathbf{x}_B} \circ \boldsymbol{\Sigma}^{\mathbf{x}_B})^{-1} \end{pmatrix},\end{aligned}$$

since under the conditions of this theorem we simply have

$$(\boldsymbol{\Sigma}^x \circ \boldsymbol{\Sigma}^x)^{-1} = \begin{pmatrix} \left((\boldsymbol{\Sigma}^{\mathbf{x}_A} \circ \boldsymbol{\Sigma}^{\mathbf{x}_A}) \right)^{-1} & \mathbf{0}_{k_A \times k_B} \\ \mathbf{0}_{k_B \times k_A} & \left((\boldsymbol{\Sigma}^{\mathbf{x}_B} \circ \boldsymbol{\Sigma}^{\mathbf{x}_B}) \right)^{-1} \end{pmatrix}.$$

As such, by interpreting $\text{Var}(\mathbf{x}_B(t)) \rightarrow +\infty$ as to mean $(\boldsymbol{\Sigma}^{\mathbf{x}_B} \circ \boldsymbol{\Sigma}^{\mathbf{x}_B})^{-1} \rightarrow \mathbf{0}_{k_B \times k_B}$ for each t and \mathbf{x} in this regime, by the result we just established we see that

$$\mathbf{K}_{f|\mathbf{x}_B}(t, \mathbf{x}) = \lim_{\text{Var}(\mathbf{x}_B(t)) \rightarrow +\infty} \mathbf{K}_f(t, \mathbf{x}) = \mathbf{0}_{l \times k}.$$

Analogously, we can see that for the smoother Kalman gain operator we have from (2.5):

$$\begin{aligned}\mathbf{K}_s(t, \mathbf{x}) &= (\boldsymbol{\Sigma}^y \circ \boldsymbol{\Sigma}^x) (\boldsymbol{\Sigma}^x \circ \boldsymbol{\Sigma}^x)^{-1} \\ &= \begin{pmatrix} \mathbf{0}_{l \times k_A} & (\boldsymbol{\Sigma}^y \circ \boldsymbol{\Sigma}^{\mathbf{x}_B}) \end{pmatrix} \begin{pmatrix} \left((\boldsymbol{\Sigma}^{\mathbf{x}_A} \circ \boldsymbol{\Sigma}^{\mathbf{x}_A}) \right)^{-1} & \mathbf{0}_{k_A \times k_B} \\ \mathbf{0}_{k_B \times k_A} & \left((\boldsymbol{\Sigma}^{\mathbf{x}_B} \circ \boldsymbol{\Sigma}^{\mathbf{x}_B}) \right)^{-1} \end{pmatrix} \\ &= \begin{pmatrix} \mathbf{0}_{l \times k_A} & (\boldsymbol{\Sigma}^y \circ \boldsymbol{\Sigma}^{\mathbf{x}_B}) (\boldsymbol{\Sigma}^{\mathbf{x}_B} \circ \boldsymbol{\Sigma}^{\mathbf{x}_B})^{-1} \end{pmatrix},\end{aligned}$$

and so, in the same vain as in the filter-based result, we end up with

$$\mathbf{K}_{s|\mathbf{x}_B}(t, \mathbf{x}) = \lim_{\text{Var}(\mathbf{x}_B(t)) \rightarrow +\infty} \mathbf{K}_s(t, \mathbf{x}) = \mathbf{0}_{l \times k}.$$

Applying now these results to (3.5a) and (3.6a), we retrieve

$$\begin{aligned}d\boldsymbol{\mu}_{f|\mathbf{x}_B}(t) &= (\boldsymbol{\Lambda}^y \boldsymbol{\mu}_{f|\mathbf{x}_B} + \mathbf{f}^y) dt, \\ \overleftarrow{d}\boldsymbol{\mu}_{s|\mathbf{x}_B}(t) &= -\left(\boldsymbol{\Lambda}^y \boldsymbol{\mu}_{s|\mathbf{x}_B} + \mathbf{f}^y - \mathbf{B}_{|\mathbf{x}_B} \mathbf{R}_{f|\mathbf{x}_B}^{-1} (\boldsymbol{\mu}_{f|\mathbf{x}_B} - \boldsymbol{\mu}_{s|\mathbf{x}_B}) \right) dt.\end{aligned}$$

Then, as in the proof of Theorem C.1, we have

$$\overleftarrow{d}(\boldsymbol{\mu}_{s|\mathbf{x}_B} - \boldsymbol{\mu}_{f|\mathbf{x}_B})(t) = -(\boldsymbol{\Lambda}^y + \mathbf{B}_{|\mathbf{x}_B} \mathbf{R}_{f|\mathbf{x}_B}^{-1})(\boldsymbol{\mu}_{s|\mathbf{x}_B} - \boldsymbol{\mu}_{f|\mathbf{x}_B})dt, \quad T \geq t \geq 0, \quad (3.7)$$

and since $\boldsymbol{\mu}_s(T) = \boldsymbol{\mu}_f(T)$, which by the continuous dependence of the filter and smoother means on their initial and terminal conditions, respectively, translates to

$$\boldsymbol{\mu}_{s|\mathbf{x}_B}(T) = \boldsymbol{\mu}_{f|\mathbf{x}_B}(T),$$

then due to this, the linearity of (3.7), and its uniqueness of solution, we recover

$$\boldsymbol{\mu}_{s|\mathbf{x}_B}(t) = \boldsymbol{\mu}_{f|\mathbf{x}_B}(t), \quad t \in [0, T].$$

As already mentioned, this has the immediate consequence that

$$\mathbf{R}_{s|\mathbf{x}_B}(t) = \mathbf{R}_{f|\mathbf{x}_B}(t), \quad t \in [0, T],$$

which yields the desired result of

$$p_t^{s|\mathbf{x}_B}(\mathbf{y}|\mathbf{x}_A) = p_t^{f|\mathbf{x}_B}(\mathbf{y}|\mathbf{x}_A), \quad t \in [0, T],$$

which in turn, by (1.14), establishes $(\mathbf{y}(t) \not\rightarrow \mathbf{x}_A)|_{\mathbf{x}_B}$ for each $t \in [0, T]$. ■

Remark C.1 (Analytical Meaning of $\text{Var}(\mathbf{x}_B(t)) \rightarrow +\infty$). *When $(\boldsymbol{\Sigma}^{\mathbf{x}_A} \circ \boldsymbol{\Sigma}^{\mathbf{x}_B}) \equiv \mathbf{0}_{k_A \times k_B}$, the interpretation of “assigning infinite uncertainty to \mathbf{x}_B ’s marginal likelihood” (Section A.4) becomes straightforward. In this case, $\text{Var}(\mathbf{x}_B(t)) \rightarrow +\infty$ simply corresponds to $(\boldsymbol{\Sigma}^{\mathbf{x}_B} \circ \boldsymbol{\Sigma}^{\mathbf{x}_B})^{-1} \rightarrow \mathbf{0}_{k_B \times k_B}$ for all t and \mathbf{x} , since $(\boldsymbol{\Sigma}^{\mathbf{x}} \circ \boldsymbol{\Sigma}^{\mathbf{x}})$ becomes block-diagonal. For general turbulent systems or when this condition fails, the interpretation of this limiting procedure requires more care. Here, $\text{Var}(\mathbf{x}_B(t)) \rightarrow +\infty$ demands rigorous analysis of the structure of \mathbf{x}_B ’s marginal likelihood and its impact on the Kalman gain operators. Only through such analysis can we properly nullify \mathbf{x}_B ’s influence when testing for conditional assimilative causal links $(\mathbf{y}(t) \rightarrow \mathbf{x}_A)|_{\mathbf{x}_B}$. We defer this detailed investigation to future work.*

Remark C.2 (Special Case: ACI Framework and Reduced CGNS Dynamics). *When $(\boldsymbol{\Sigma}^{\mathbf{x}_A} \circ \boldsymbol{\Sigma}^{\mathbf{x}_B}) \equiv \mathbf{0}_{k_A \times k_B}$ in a CGNS, implementing the condition within the generalized ACI framework $(\boldsymbol{\Sigma}^{\mathbf{x}_B} \circ \boldsymbol{\Sigma}^{\mathbf{x}_B})^{-1} \rightarrow \mathbf{0}_{k_B \times k_B}$ (Section A.4) leads to an equivalent reduced system. In this reduced system, the state estimation of $\mathbf{y}(t)$ becomes governed by the CGNS defined in (3.2a) and (3.2c), where $(\mathbf{x}_A, \mathbf{y})$ form the state variables, with \mathbf{x}_B being reduced to a deterministic forcing term defined by its observed values (analogous to a control or input term).*

SI.D Numerical Studies: ACI Performance in Nonlinear Systems with Intermittency, Regime Switching and Extreme Events

This section includes three numerical studies that exploit the ACI framework to study complex dynamical systems with intermittency, non-Gaussian features, regime switching, and extreme events. All test cases employ CGNS models, leveraging their analytical tractability while capturing these nonlinear phenomena. Additionally, unless otherwise specified, the efficient approximation in (1.25) is used to compute the objective (C)CIR lengths.

D.1 A Nonlinear Dyad Model with Intermittent Extreme Events

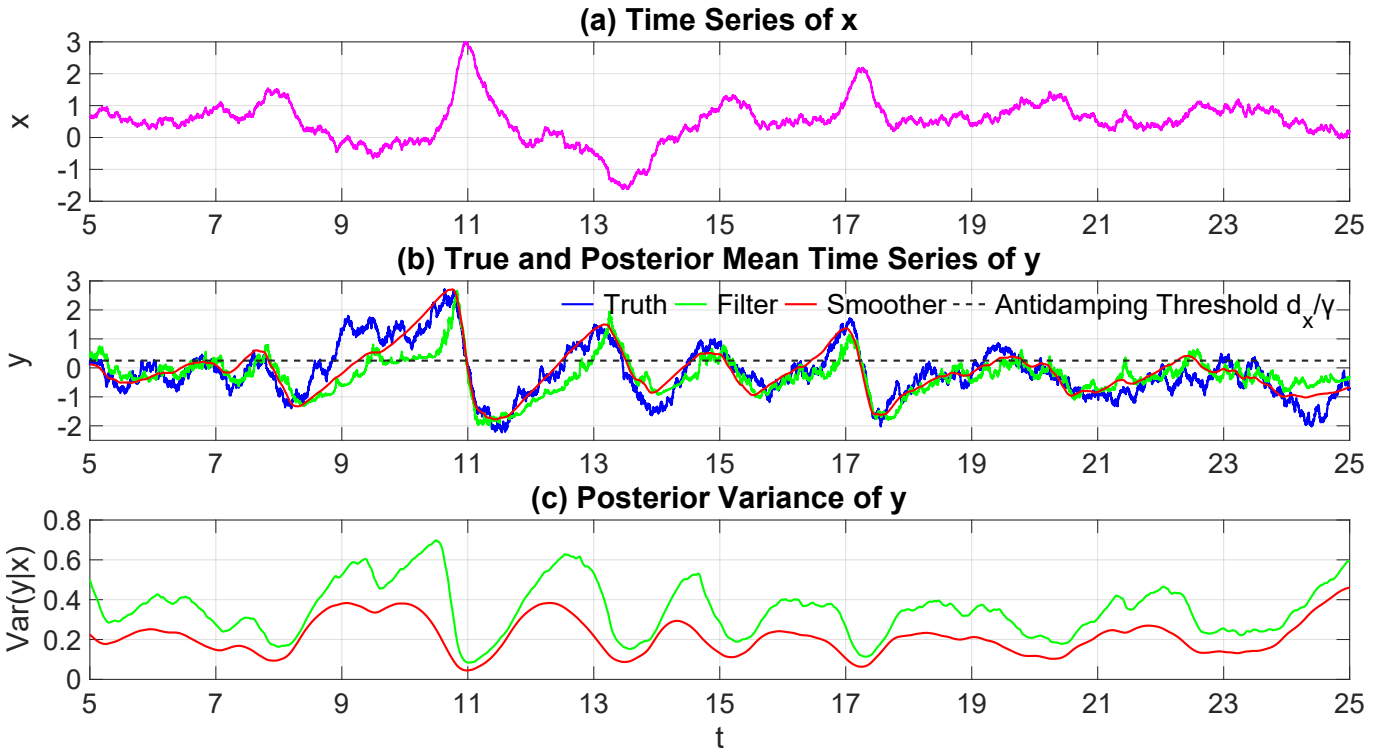
For completeness, we restate the nonlinear dyad model described in the main text (in differential form):

$$dx = (-d_x x + \gamma xy + f_x)dt + \sigma_x dW_x \quad (4.1a)$$

$$dy = (-d_y y - \gamma x^2 + f_y)dt + \sigma_y dW_y. \quad (4.1b)$$

This is a reduced-order conceptual model for atmospheric variability. It has been used to analyze the effects of various coarse-grained procedures on processes exhibiting intermittency, large-scale bifurcations, and microscale phase transitions. It is defined by an energy-conserving condition on its quadratic nonlinearities [20]. The coupling parameter $\gamma > 0$ plays a crucial role by ensuring significant positive y values ($y > d_x/\gamma$) trigger extreme events in x .

Supplementary Figure 1 presents the data assimilation results for the dyad model in (4.1). The key distinction between the filter and smoother distributions in estimating y occurs prior to extreme events in x . This behavior is expected since the filter, operating without knowledge of future observations, cannot fully anticipate the triggering mechanism in y . In contrast, the smoother benefits from future extreme event data, enabling more accurate state estimation of y with reduced uncertainty.



Supplementary Figure 1: Data assimilation of the dyad model (4.1). Panel (a): A single realization of the observed variable x . Panel (b): The true hidden signal y (blue) alongside the posterior mean estimates from filtering (green) and smoothing (red), where the smoother is the complete smoother using all the information in future. The dashed line marks the anti-damping threshold, above which the net damping $-d_x + \gamma y$ in (4.1a) becomes positive. Panel (c): Posterior variance of the filtered and smoothed estimates of y .

Supplementary Figure 2 displays the ACI and CIR analyses. Several important patterns emerge:

- First, the ACI value (Panel (d)) reaches its maximum during y 's strongest anti-damping phase, corresponding to y 's peak instantaneous influence on x .
- Second, the subjective CIR attains its highest values (shown by the deep red shading in Panel (b)) slightly before $y > d_x/\gamma$ (initiating an extreme event) and for small ε thresholds (indicating

a longer-range influence). This reveals that extreme events develop gradually, with triggering conditions established well in advance. Notably, the objective CIR's temporal extent does not reach the actual peak of extreme events. This finding mirrors the decorrelation time (the integration of the autocorrelation function) in complex dynamical systems, where the true causal influence often persists weakly beyond the formal timescale indicated by the objective function.

- Third, and most significantly, the objective CIR shortens as the system approaches y 's positive peak (corresponding to x 's extreme event buildup phase). At this stage, the filter can reliably detect the emerging pattern without requiring future information. This transition naturally partitions the time series at each extreme event, marking distinct dynamical regimes: a buildup phase with long-range dependence (where future information improves estimation) and an event phase where the trajectory becomes locally predictable. The short CIR also persists during y 's demise, where x is the driving factor behind the system dynamics (high signal-to-noise ratio) and controls y via $-\gamma x^2$.
- Finally, Panel (c) showcases the temporal evolution of the objective CIR for $y(t) \rightarrow x$, calculated using both the definition in (1.22) and its approximation in (1.25). This confirms the results of Theorem A.1 and (1.25), and clearly demonstrates the high skill that this computationally efficient approximation achieves while circumventing the expensive quadrature entailed by the ε -integrals of the subjective CIRs in the definition. Significantly, it captures the exact profile of the exact definition. This is true both during the quiescent phases of the signal, but importantly also at the onset of the extreme events generated by y .

These results demonstrate that extreme events in this system are not sudden occurrences, but rather the outcome of gradually evolving conditions. The triggering mechanism begins significantly earlier than the actual event, with effects that propagate both forward and backward in time, as evidenced by the CIR patterns.

D.2 A Noisy Predator–Prey Model

The predator–prey model (also known as the Lotka–Volterra model) is fundamentally important across scientific disciplines as it captures the universal dynamics of interacting populations through simple yet powerful mathematics [7]. Originating in ecology to explain cyclical fluctuations between species like lynx and hares, its core principles have been adapted to model diverse systems, from disease spread in epidemiology to competition in economics and even chemical oscillations. The nonlinear feedback mechanisms in the model provide crucial insights into understanding stability, resilience, and emergent patterns of many natural and scientific problems.

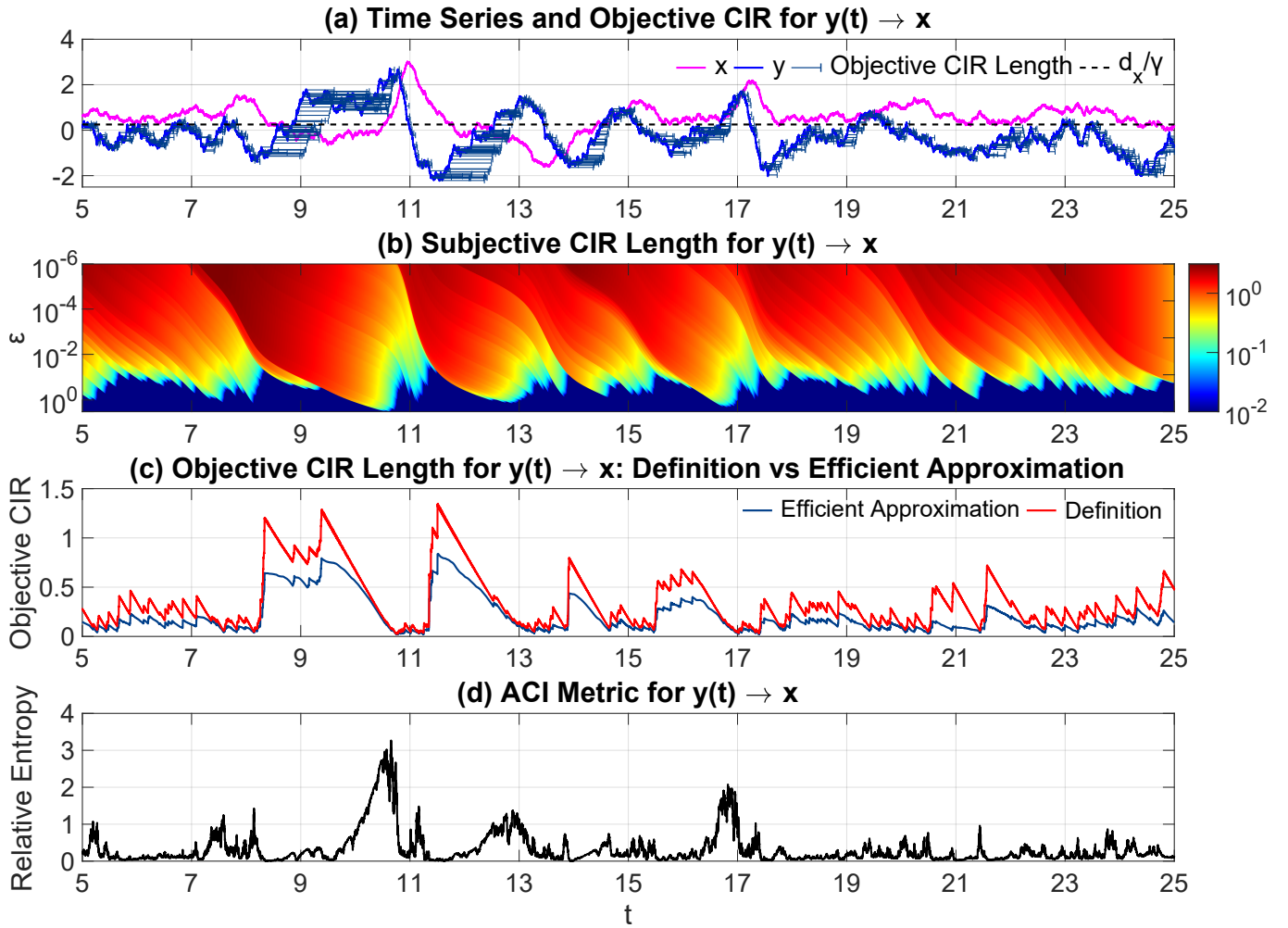
Let us consider a noisy version of the predator–prey model:

$$dx = (\beta xy - \alpha x)dt + \sigma_x dW_x, \quad (4.2a)$$

$$dy = (\gamma y - \delta xy)dt + \sigma_y dW_y, \quad (4.2b)$$

In (4.2), x and y represent the population densities of a predator species and its prey, respectively, with their time derivatives (dx/dt and dy/dt) describing their instantaneous population growth rates. The predator dynamics are governed by two parameters: α , the predator's natural death rate, and β , which quantifies how prey availability enhances predator growth. The prey dynamics depend on γ , which is the maximum intrinsic growth rate of the prey, and δ , which captures the negative impact of predators on the prey population. To ensure results are biologically realistic in finite-length simulations, small additive noise terms (σ_x and σ_y) are included, preventing populations from reaching nonphysical negative values. The parameter values in the study here are as follows:

$$\alpha = 0.4, \quad \beta = 0.1, \quad \sigma_x = 0.3, \quad \gamma = 1.1, \quad \delta = 0.4, \quad \sigma_y = 0.3.$$

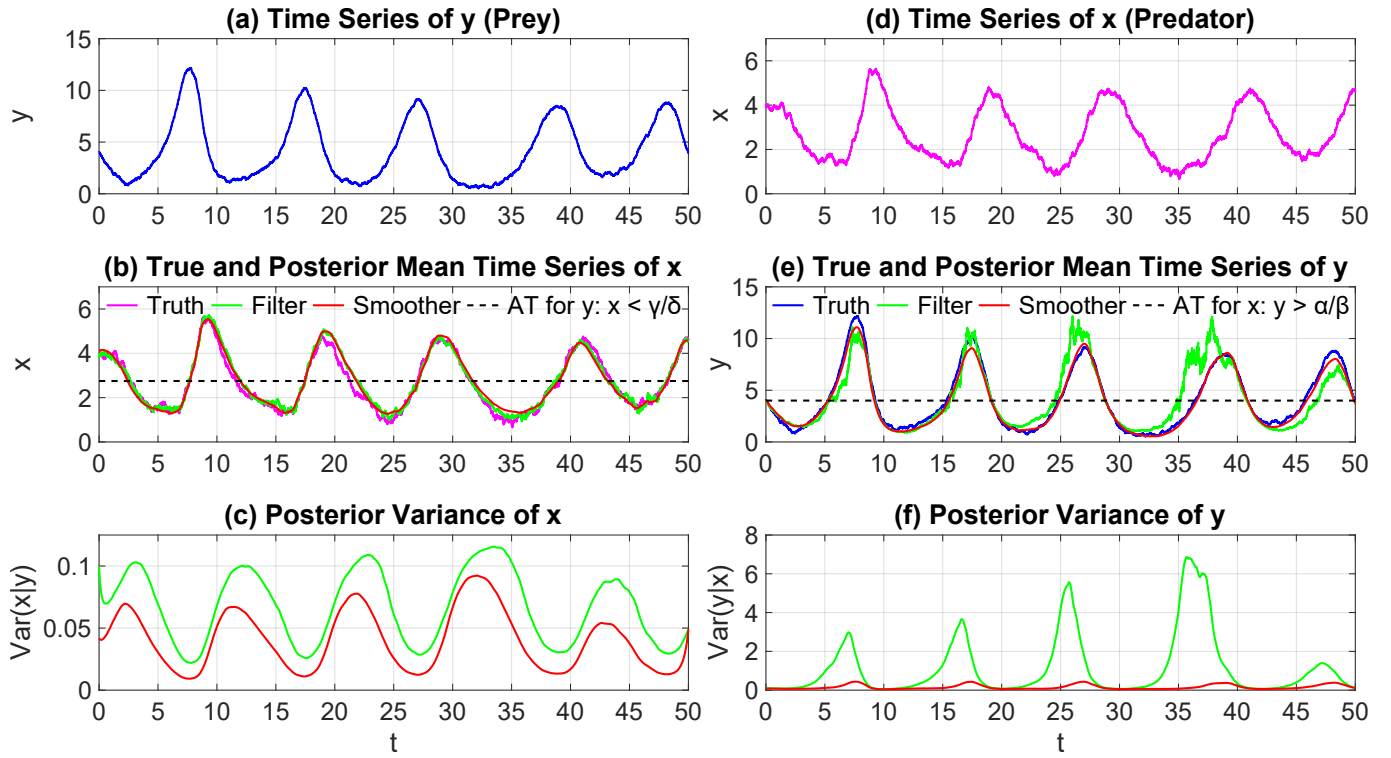


Supplementary Figure 2: ACI values and CIRs for the nonlinear dyad model (4.1) from y to x as functions of time. Panel (a): Time series of x (magenta) and y (blue), with the objective CIR depicted as whiskers extending forward in time from each $y(t)$. The dashed horizontal line marks the anti-damping threshold d_x/γ . Panel (b): Subjective CIR (shaded region, logarithmically scaled) as a function of the threshold ε (logarithmic, reversed y -axis). Panel (c): Objective CIRs from y to x over time, calculated using both the definition (1.22) (in red) and the computationally efficient approximation (1.25) (in navy blue), corresponding to the whiskers in Panel (a). Panel (d): ACI values from y to x over time.

Since both β and δ are positive, larger prey population y enhances the anti-damping effect in the x equation, while larger predator population x intensifies the damping in y . The resulting coupled variations in x and y produce intermittent phase alternations in the system dynamics. Note that since (4.2) is conditionally linear both in x and y , it is a bidirectional CGNS, meaning both posterior distributions, $x|y$ and $y|x$, are Gaussian.

Supplementary Figure 3 displays the data assimilation results. Panels (a)–(c) and (d)–(f) show the results by observing y (recovering x) and observing x (recovering y), respectively. The state estimation is more informative when the observed signal has a large value, corresponding to when the estimated variable induces an extreme event in the former’s evolution. Additionally, the uncertainty reduction in the smoother related to the filter is more significant when the predator x is the observed variable, which accounts for the choice of the coupling, quadratic feedback parameter values; $\delta > \beta$.

Supplementary Figure 4 presents the ACI value (instantaneous causal strength) and CIR (influence duration) between predator (x) and prey (y) populations. The interaction exhibits two distinct regimes:



Supplementary Figure 3: Data assimilation of the noisy predator–prey model (4.2). Panels (a)–(c) and (d)–(f) show the results by observing y (recovering x) and observing x (recovering y), respectively. The dashed lines in Panels (b) and (e) indicate the anti-damping threshold values.

1. Predator-to-Prey Causality (x -to- y ; Panels (a)–(b)):

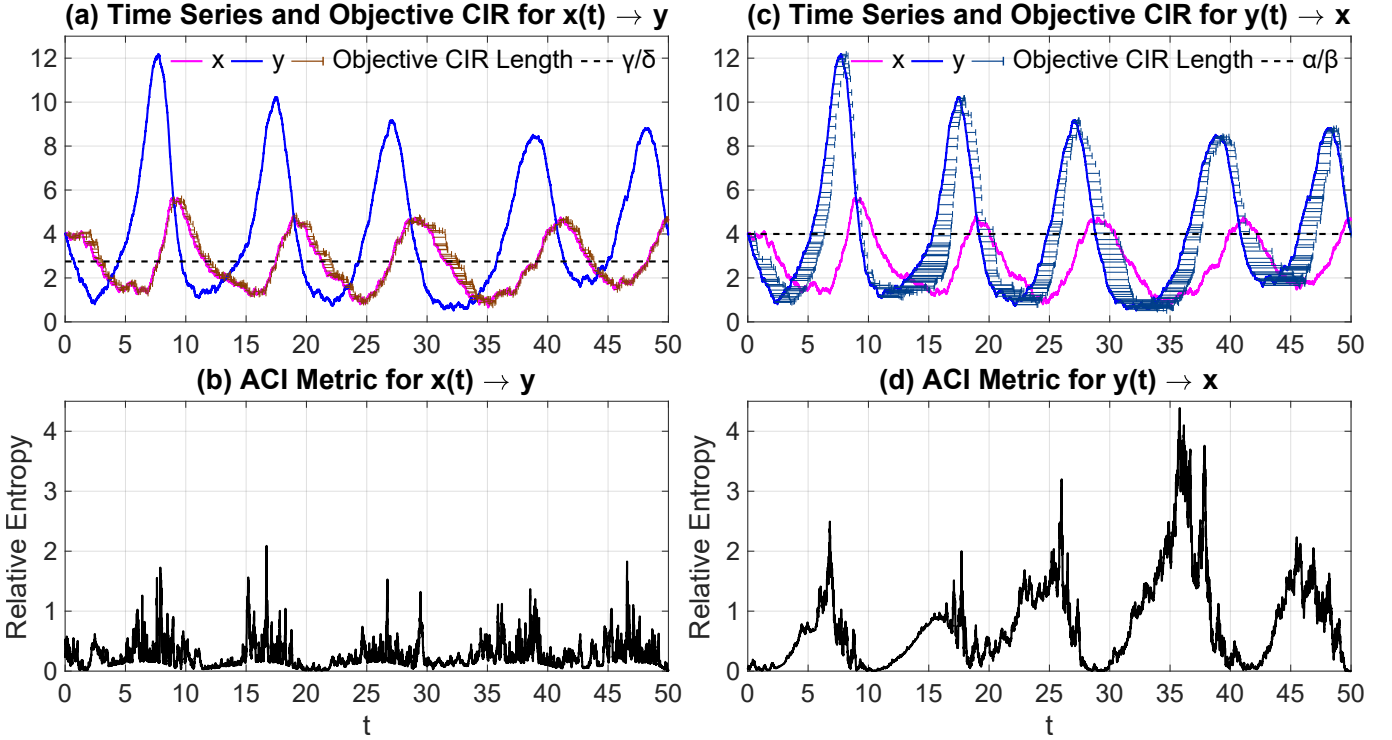
- When the predator population x is below the threshold γ/δ , the net damping in the prey equation becomes positive (anti-damping phase), allowing y to grow, though at a progressively slower rate as x increases.
- Once x exceeds γ/δ , strong positive damping emerges causing y to decline. This demonstrates how predator growth first suppresses then reverses prey population trends.
- Notably, when y is small, x shows weak instantaneous influence (low ACI values) but exhibits extended CIRs, which reveals how predator reduction leads to delayed prey resurgence.

2. Prey-to-Predator Causality (y -to- x ; Panels (c)–(d)):

- The prey population y acts as an anti-damping term for predators during its abundance (when $y > \alpha/\beta$), directly driving x growth with persistent temporal effects (long CIRs).
- The subsequent prey collapse (sharp y decrease) when the predator population reaches the critical quantity ($x > \gamma/\delta$) reflects predator overconsumption rather than causing predator dynamics (causal link reversal), which is consistent with the x -to- y causality shown in Panels (a)–(b).
- Due to the stronger coupling feedback in y , $\delta > \beta$, the ACI metric for $y(t) \rightarrow x$ is stronger. Furthermore, the damping effect that x 's growth induces has a more immediate impact on the prey population y , when compared to the more delayed effect that prey prosperity y has on the predators x .

Remarkably, the causal relationship between predator (x) and prey (y) is bidirectional during specific phases. Prior to the prey population peak, while y is growing but x remains below the anti-damping threshold, the variables exhibit strong mutual interaction: the increasing prey population y drives

predator growth (x), while simultaneously, the rising predator population x suppresses (but does not yet reverse) the prey’s growth rate. This creates a transient period of coupled positive feedback ($y \rightarrow x$) and negative feedback ($x \rightarrow y$).



Supplementary Figure 4: ACI values and CIRs for the noisy predator–prey model (4.2). Only the objective CIRs are shown. Panels (a)–(b) and (c)–(d) show the results from $x(t)$ to y and from $y(t)$ to x , respectively. The dashed lines in Panels (a) and (b) indicate the anti-damping threshold values in the equations of y and x , respectively.

D.3 A Stochastic Model Capturing the El Niño–Southern Oscillation (ENSO) Diversity

D.3.1 Model Details

As was described in the main text, although few models can accurately capture ENSO diversity, a recently developed stochastic conceptual model successfully reproduces its diverse behaviors and non-Gaussian statistics [5]. This model has been highlighted in a recent review [29], making it a suitable testbed for studying El Niño diversity. Using the defined abbreviations from the main text, the model consists of six state variables: ocean zonal current in the CP (u), WP thermocline depth (h_W), CP SST (T_C), EP SST (T_E), atmospheric winds (τ , intraseasonal), and background Walker circulation (I , decadal). The variables (u , h_W , T_C , and T_E) operate on interannual timescales and model the anomalies away from the corresponding climatology. As a nonlinear system with state-dependent noise, the model generates extreme events and intermittency. Note that the decadal variable represents the strength of the Walker circulation. The two SST variables (T_C and T_E) allow reconstruction of spatiotemporal SST patterns across the equatorial Pacific, providing an intuitive way to identify different ENSO event types. The model reads:

$$du = \left(-ru - \delta_u \frac{T_C + T_E}{2} + \beta_u(I)\tau \right) dt + \sigma_u dW_u, \quad (4.3a)$$

$$dh_W = \left(-rh_W - \delta_h \frac{T_C + T_E}{2} + \beta_h(I)\tau \right) dt + \sigma_h dW_h, \quad (4.3b)$$

$$dT_C = \left((r_C - c_1(t, T_C)) T_C + \zeta_C T_E + \gamma_C h_W + \sigma(I)u + C_u + \beta_C(I)\tau \right) dt + \sigma_C dW_C, \quad (4.3c)$$

$$dT_E = \left((r_E - c_2(t)) T_E - \zeta_E T_C + \gamma_E h_W + \beta_E(I) \tau \right) dt + \sigma_E dW_E, \quad (4.3d)$$

$$d\tau = -d_\tau \tau dt + \sigma_\tau(t, T_C) dW_\tau, \quad (4.3e)$$

$$dI = -\lambda(I - m) dt + \sigma_I(I) dW_I. \quad (4.3f)$$

While the full model details are available in [5], its basic mechanism can be summarized as follows. EP El Niño events are typically associated with a strong thermocline buildup in the WP, whereas CP EN and La Niña events are primarily triggered by advective processes. In the latter case, when $\sigma(I) \propto I$ is larger, indicating a strengthening Walker circulation, the advection term u becomes dynamically significant in driving T_C . Unlike the standard discharge–recharge oscillator model, which couples h_W and T_E , the T_C variable acts as a transitional component that is expected to have a more direct influence on T_E .

D.3.2 Additional Results Using Model-Generated Data

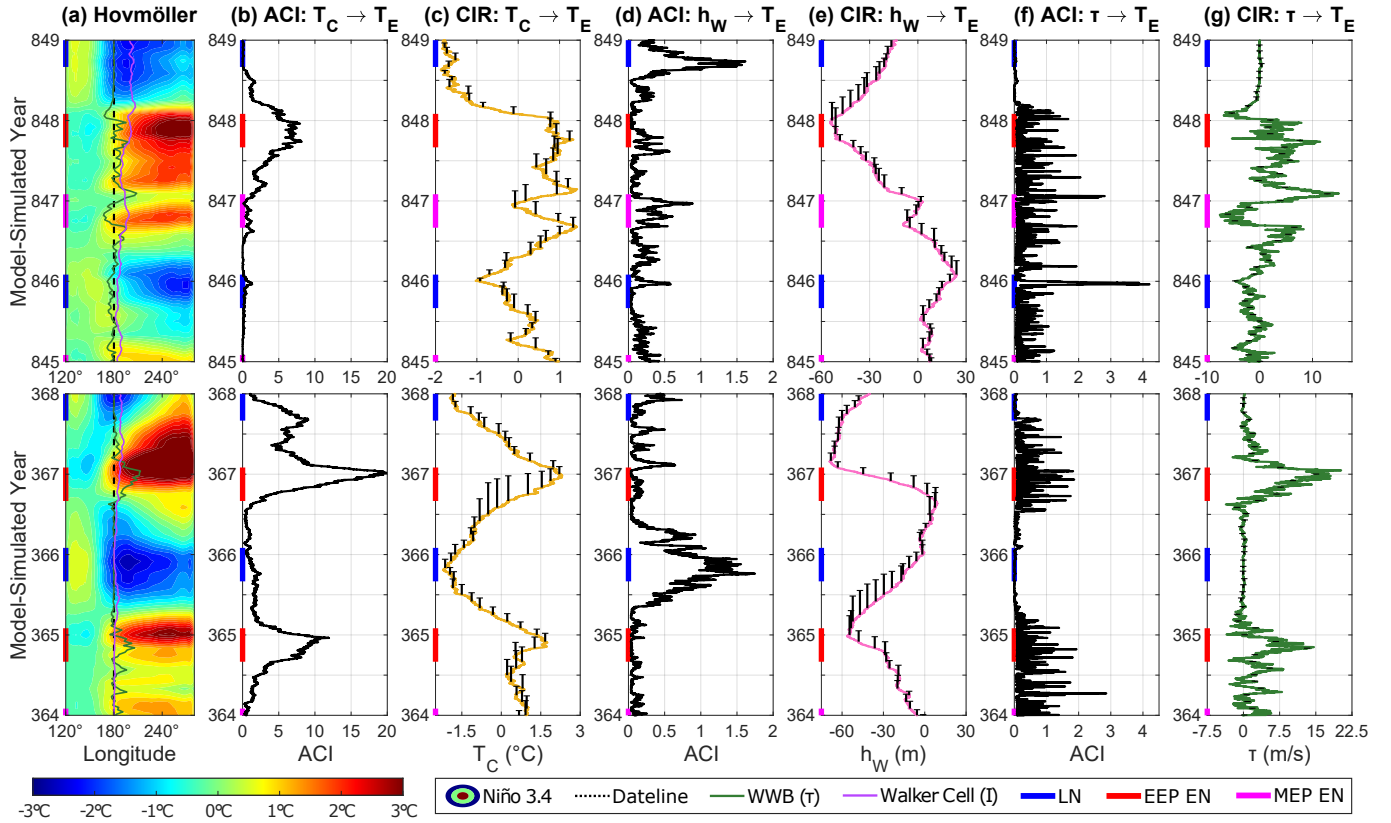
Supplementary Figure 5 shows conditional ACI values and CCIRs for model-simulated EP events (target variable: T_E). We note that the variables not appearing in the title of each column are resolved in the corresponding causal relationship through the conditional ACI framework (similarly for Supplementary Figure 6). Among the three potential causal variables, T_C has the strongest ACI value, peaking slightly before T_E during EP El Niño events (red positive T_E anomalies). This timing makes physical sense because SSTs in these regions are strongly coupled: during El Niño, warm water moves from CP to EP, explaining why T_C leads. The τ - T_E ACI value is noisier due to τ 's short-term variability, but still shows τ 's clear impact on T_E . Winds both push warm water and directly affect SSTs quickly. While h_W does influence T_E , its ACI value is weaker than T_C or τ . According to discharge–recharge theory [13], h_W and T_E form an oscillator, but in models with CP resolution, h_W affects T_E indirectly: first changing T_C , which then affects T_E (WP→CP→EP). This explains why h_W 's ACI value peaks months before EP El Niño maxima, specifically during periods where h_W starts to increase thus initiating upwelling processes that generate extreme warming centers in the EP. The CIRs further corroborate these underlying mechanisms in the temporal sense: T_C has the longest influence, h_W 's more indirect role gives medium-length CIRs, and τ 's shortest-term variability leads to the briefest impacts.

Supplementary Figure 6 shows conditional ACI values and CCIRs for model-simulated CP events (target variable: T_C). When the decadal variable I is significant, u contributes substantially to CP events through the enhanced zonal advective feedback ($\sigma(I) \propto I$) according to (4.3c), peaking slightly before CP El Niño events. The WP thermocline (h_W) also affects T_C via positive feedback in (4.3c), but peaks earlier than the CP event. While the u and h_W ACIs sometimes coincide due to state-space correlations, h_W 's CIR persists longer due to WP-CP information transfer delays. Wind (τ) influences CP events on shorter intraseasonal timescales. Unlike EP events, CP events show balanced contributions from u , h_W , and τ . The strong ACI value from u to T_C around $t = 1985$ corresponds to the rapid transition from CP El Niño to La Niña, where the value of u changes dramatically from positive to negative. Furthermore, during the second year of the multi-year CP La Niña events (i.e., $t = 1986$), all three ACIs drop suddenly, as the signals of all these three variables remain near zero. This corresponds to a typical discharge phase of ENSO.

D.3.3 ACI on Real-World ENSO Data

In this subsection, we apply the ACI framework on real-world observational data to study the ENSO diversity through (4.3).

The oceanic data used here, including the monthly SST, zonal current velocity, and thermocline depth (calculated from the potential temperature at the depth of the 20°C isotherm) measurements, are sourced from the GODAS dataset (<https://www.psl.noaa.gov/data/gridded/data.godas.html>)

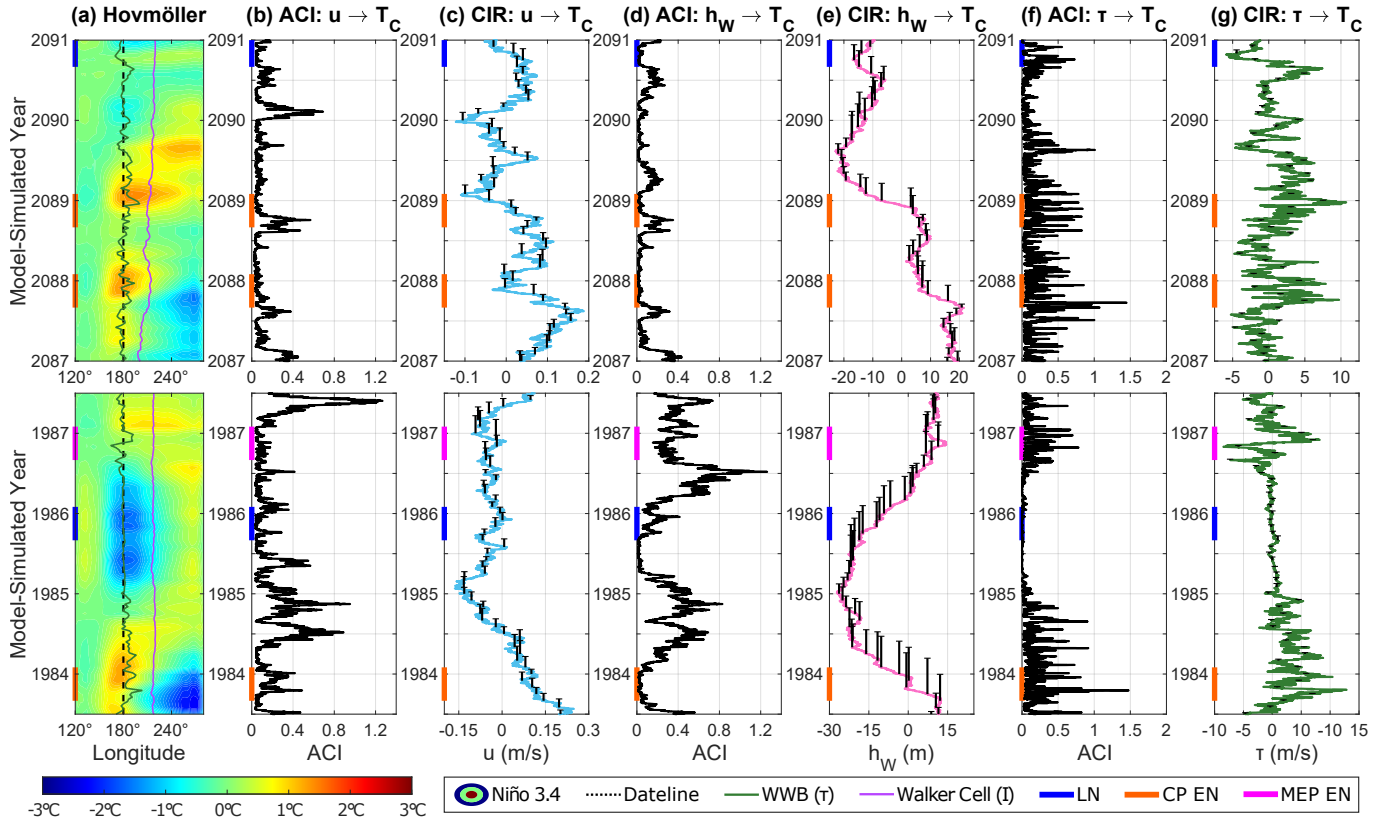


Supplementary Figure 5: Conditional ACI values and CCIRs for some model-simulated EP events (EEP EN and MEP EN stand for extreme and moderate EP El Niño, respectively, and LN for La Niña); $t \in [364, 368]$ and $t \in [845, 849]$. Panel (a): Hovmöller diagram of the SST anomalies in the equatorial Pacific reconstructed from T_C and T_E via a spatiotemporal multivariate regression technique [5]. The wind profile τ , plotted above and centered around the dateline, is superimposed along with the decadal variable I , whose time series is also positioned relative to the dateline: Positive τ (indicating westerly winds) appear to the right of the dateline, while negative values appear to the left, and a weakening Walker circulation appears close to the dateline, while a stronger I appears further to its right. Panel (b): Conditional ACI values from T_C to T_E . Panel (c): Time series of T_C and the corresponding CCIRs from T_C to T_E (depicted as whiskers at each month, similar to Panel (a) of Supplementary Figure 2). Panels (d)–(e) and (f)–(g): Similar to (a)–(b) but for h_W and τ . The two rows represent two distinct periods. The Walker circulation in both cases is nearly zero, which is the usual condition to trigger EP events.

[3]. The present study solely uses oceanic anomalies, calculated by removing the monthly mean climatology over the whole analysis period. The data spans from January 1982 to December 2017, chosen to fall within the satellite era when observations are more reliable. The atmospheric wind data is obtained from the National Centers for Environmental Prediction-National Center for Atmospheric Research (NCEP-NCAR) reanalysis data set (<https://psl.noaa.gov/data/gridded/data.ncep.reanalysis.html>) [15] over the same period.

The model used within ACI remains the stochastic conceptual model defined in (4.3a)–(4.3f). However, because the observations are now drawn from the real world rather than from synthetic data, this study no longer has a perfect-model setup. Nevertheless, as shown in [5], the conceptual model in (4.3a)–(4.3f) successfully reproduces key statistical features of observed ENSO variability and generates time series that are qualitatively consistent with real ENSO episodes. Hence, the model error is expected to be relatively small.

Daily data are available for the wind burst amplitudes τ , whereas all other variables are monthly. To ensure the stability of the filter, smoother, and online-smoother algorithms required for the



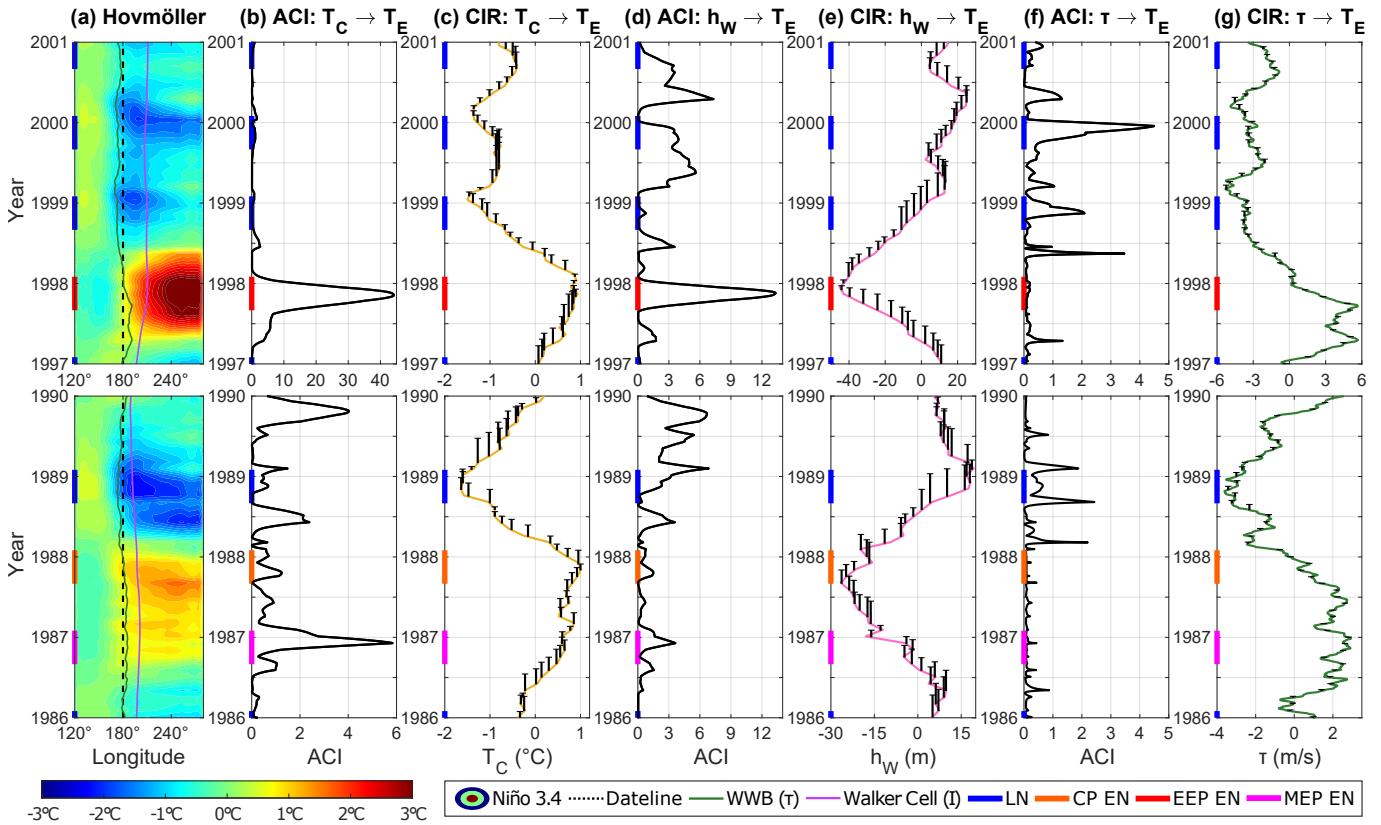
Supplementary Figure 6: Conditional ACI values and CCIRs for some model-simulated CP events (CP EN and MEP EN stand for CP and moderate EP El Niño, respectively, and LN for La Niña); $t \in [1983.5, 1987.5]$ and $t \in [2087, 2091]$. Panel (a): Same as Panel (a) of Figure 5. Panel (b): Conditional ACI values from u to T_C . Panel (c): Time series of u and the corresponding CCIRs from u to T_C (depicted as whiskers at each month, similar to Panel (a) of Supplementary Figure 2). Panels (d)–(e) and (f)–(g): Similar to (a)–(b) but for h_W and τ . The Walker circulation in this case is strong, which is the usual condition to trigger CP events.

conditional ACI analysis and the computation of the CCIRs, we linearly interpolate all data onto a uniform temporal grid with a spacing of approximately 7 hours and 20 minutes. Linear interpolation has been shown to be more compatible with data assimilation than smoother interpolation methods [11]. Since the oceanic variables primarily evolve on interannual timescales, this approximation is not expected to alter the data’s underlying dynamics. This procedure also provides an opportunity to test the robustness of the ACI framework with respect to potential numerical discretization errors.

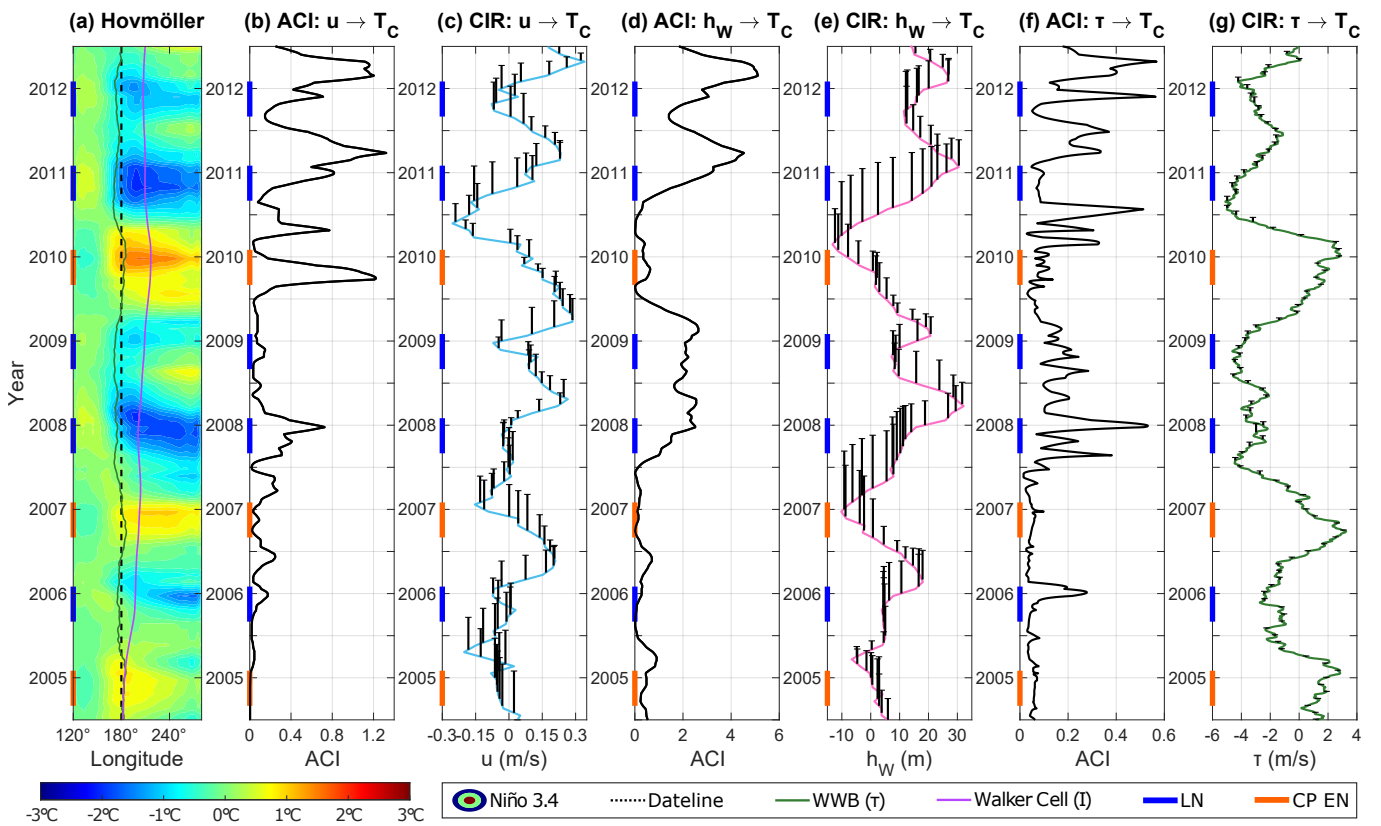
Supplementary Figure 7 includes the historically strongest EP El Niño event in 1998 and a moderately strong EP event in 1987, together with their subsequent La Niña phases. Supplementary Figure 8 presents several CP events that occurred in the early 21st century. The results based on real-world observations show qualitatively similar conclusions to those in Supplementary Figures 5–6, which use model-generated synthetic data.

Specifically, during EP El Niño phases, the causal links $T_C \rightarrow T_E$, $h_W \rightarrow T_E$, and $\tau \rightarrow T_E$ are identified. In addition, the thermocline continues to play a key role during EP La Niña events through the recharge–discharge mechanism, while there are no clear causal influences from T_C and τ to T_E , consistent with the classical discharge process. Likewise, during CP El Niño phases, $u \rightarrow T_C$ and $\tau \rightarrow T_C$ emerge as the two most significant causal relationships, while during CP La Niña phases $h_W \rightarrow T_C$ is also detected. All of these findings are consistent with those obtained from the model-generated experiments.

The results presented here suggest that ACI performs reasonably well in the presence of noisy ob-



Supplementary Figure 7: Conditional ACI values and CCIRs for some real-world EP events; Similar to Supplementary Figure 5 but the observations are collected from real-world data.



Supplementary Figure 8: Conditional ACI values and CCIRs for some real-world CP events; Similar to Supplementary Figure 6 but the observations are collected from real-world data.

servations, moderate model error, and some numerical discretization effects. While more systematic

studies are needed to fully quantify the influence of these factors, the results here provide some preliminary evidence that the ACI framework maintains a degree of robustness under these conditions.

Finally, it is worth emphasizing the distinction between ACI and many baseline causal inference methods for analyzing real-world ENSO datasets [25, 27, 8]. Most of the current approaches are purely data-driven and focus on identifying broad, time-averaged cause-and-effect relationships. Their findings are generally consistent with physical mechanisms, such as the causal influence of the thermocline depth on the SST and the discharge–recharge loop linking El Niño and La Niña. Yet, ACI provides a more refined and event-specific indicator that reveals how individual variables contribute to the causal structure of each ENSO episode, an aspect often missing from state-of-the-art techniques. ACI yields markedly different causal strengths and CIR patterns across events, providing valuable insight into instantaneous, time-localized cause-and-effect behavior. As a natural direction for future work, the ACI framework can be coupled with a range of ENSO models and expanded to include additional variables, thereby enhancing causal discovery with a particular focus on instantaneous relationships.

Supplementary Information References

- [1] Hisham Abou-Kandil, Gerhard Freiling, Vlad Ionescu, and Gerhard Jank. *Matrix Riccati Equations in Control and Systems Theory*. Birkhäuser Basel, 2003.
- [2] Marios Andreou, Nan Chen, and Yingda Li. An Adaptive Online Smoother with Closed-Form Solutions and Information-Theoretic Lag Selection for Conditional Gaussian Nonlinear Systems. *arXiv preprint arXiv:2411.05870*, 2024.
- [3] David Behringer and Yan Xue. Evaluation of the global ocean data assimilation system at NCEP: The Pacific Ocean. In *Eighth symp. on integrated observing and assimilation systems for atmosphere, oceans, and land surface*, 2004.
- [4] David Cai, Richard Kleeman, and Andrew Majda. A Mathematical Framework for Quantifying Predictability Through Relative Entropy. *Methods and Applications of Analysis*, 9(3):425–444, 2002.
- [5] Nan Chen, Xianghui Fang, and Jin-Yi Yu. A multiscale model for El Niño complexity. *npj Climate and Atmospheric Science*, 5(1):16, 2022.
- [6] Nan Chen and Andrew J Majda. Conditional Gaussian systems for multiscale nonlinear stochastic systems: Prediction, state estimation and uncertainty quantification. *Entropy*, 20(7):509, 2018.
- [7] Dennis Cooke and Robert William Hiorns. *The Mathematical Theory of the Dynamics of Biological Populations 2: Based on the Proceedings of a Conference on The Mathematical Theory of the Dynamics of Biological Populations Organised by the Institute of Mathematics and Its Applications and Held in Oxford, 1st-3rd July, 1980*. Academic Press, 1981.
- [8] Fabrizio Falasca, Pavel Perezhgin, and Laure Zanna. Data-driven dimensionality reduction and causal inference for spatiotemporal climate fields. *Physical Review E*, 109(4):044202, 2024.
- [9] Jean H Gallier. The Schur Complement and Symmetric Positive Semidefinite (and Definite) Matrices. <https://www.cis.upenn.edu/~jean/schur-comp.pdf>, 2019. [Online; Accessed 25-March-2025].
- [10] Xiaoying Han and Peter E. Kloeden. *Random Ordinary Differential Equations and Their Numerical Solution*. Springer Singapore, 2017.

- [11] John Harlim. Interpolating irregularly spaced observations for filtering turbulent complex systems. *SIAM Journal on Scientific Computing*, 33(5):2620–2640, 2011.
- [12] Nobuyuki Ikeda and Shinzo Watanabe. *Stochastic differential equations and diffusion processes*, volume 24. Elsevier, 2014.
- [13] Fei-Fei Jin. An equatorial ocean recharge paradigm for ENSO. Part I: Conceptual model. *Journal of the atmospheric sciences*, 54(7):811–829, 1997.
- [14] R. E. Kalman and R. S. Bucy. New Results in Linear Filtering and Prediction Theory. *Journal of Basic Engineering*, 83(1):95–108, March 1961.
- [15] Eugenia Kalnay, Masao Kanamitsu, Robert Kistler, William Collins, Dennis Deaven, Lev Gandin, Mark Iredell, Suranjana Saha, Glenn White, John Woollen, et al. The NCEP/NCAR 40-year reanalysis project. In *Renewable energy*, pages Vol1_146–Vol1_194. Routledge, 2018.
- [16] Richard Kleeman. Measuring Dynamical Prediction Utility Using Relative Entropy. *Journal of the Atmospheric Sciences*, 59(13):2057 – 2072, 2002.
- [17] Richard Kleeman. Information Theory and Dynamical System Predictability. *Entropy*, 13(3):612–649, March 2011.
- [18] X San Liang. Information flow and causality as rigorous notions ab initio. *Physical Review E*, 94(5):052201, 2016.
- [19] Robert S Liptser and Albert N Shiryaev. *Statistics of random processes I: General theory & Statistics of Random Processes II: Applications*. Springer Science & Business Media, 2001.
- [20] Andrew J Majda and John Harlim. Physics constrained nonlinear regression models for time series. *Nonlinearity*, 26(1):201–217, November 2012.
- [21] Andrew J Majda, Ilya Timofeyev, and Eric Vanden-Eijnden. Systematic strategies for stochastic mode reduction in climate. *Journal of the Atmospheric Sciences*, 60(14):1705–1722, 2003.
- [22] Tobias Neckel and Florian Rupp. *Random Differential Equations in Scientific Computing*. Ver-sita, November 2013.
- [23] Bernt Øksendal. *Stochastic Differential Equations*. Universitext. Springer, Berlin, Germany, July 2003.
- [24] Herbert E Rauch, F Tung, and Charlotte T Striebel. Maximum likelihood estimates of linear dynamic systems. *AIAA journal*, 3(8):1445–1450, 1965.
- [25] Mark D Risser, Mohammed Ombadi, and Michael F Wehner. Granger causal inference for climate change attribution. *Environmental Research: Climate*, 4(2):022001, 2025.
- [26] Boris L. Rozovsky and Sergey V. Lototsky. *Stochastic Evolution Systems: Linear Theory and Applications to Non-Linear Filtering*, volume 89. Springer Science & Business Media, 2018.
- [27] Jakob Runge, Andreas Gerhardus, Gherardo Varando, Veronika Eyring, and Gustau Camps-Valls. Causal inference for time series. *Nature Reviews Earth & Environment*, 4(7):487–505, 2023.
- [28] Thomas Schreiber. Measuring information transfer. *Physical review letters*, 85(2):461, 2000.
- [29] J Vialard, F-F Jin, MJ McPhaden, A Fedorov, W Cai, S-I An, D Dommenges, X Fang, MF Stuecker, C Wang, et al. The El Niño Southern Oscillation (ENSO) recharge oscillator conceptual model: Achievements and future prospects. *Reviews of Geophysics*, 63(1):e2024RG000843, 2025.